UNIVERSITY OF Southampton

University of Southampton Research Repository
ePrints Soton

Copyright © and Moral Rights for this thesis are retained by the author and/or other copyright owners. A copy can be downloaded for personal non-commercial research or study, without prior permission or charge. This thesis cannot be reproduced or quoted extensively from without first obtaining permission in writing from the copyright holder/s. The content must not be changed in any way or sold commercially in any format or medium without the formal permission of the copyright holders.

When referring to this work, full bibliographic details including the author, title, awarding institution and date of the thesis must be given e.g.

AUTHOR (year of submission) "Full thesis title", University of Southampton, name of the University School or Department, PhD Thesis, pagination

http://eprints.soton.ac.uk

University of Southampton

Optoelectronics Research Centre

A Thesis Submitted in Partial Fulfilment for Doctor of Philisophy

Coherent Diffraction Imaging using a High Harmonic Source at 40 eV

Author:
Aaron Parsons

Supervisor:
Dr. W.S Brocklesby

August 4, 2014

Abstract

This thesis presents the current status of coherent diffractive imaging and ptychography using the high harmonic at the University of Southampton. The full system used to generate the 40 eV radiation and collect the far-field speckle patterns is outlined and critical criteria discussed. The algorithms used to re-phase the data are outlined and some simple 1-dimensional examples are given. The question of how to appropriately state the resolution of a coherent diffraction system is addressed and the concluding results are applied to the work in the experimental chapters, of which this thesis contains two.

The first, is a published result which investigates the treatment of partial temporal coherence through the coherent diffraction process. Partial coherence for a high harmonic source is slightly more complex to treat than standard broad-bandwidth sources since the spectrum is modulated by the narrow-bandwidth harmonic comb underneath a broad-bandwidth envelope. An experimental investigation is presented by illuminating the same amplitude mask under broad-band and narrow-band conditions using the same imaging systems. The results are discussed and conclude that a much greater than expected (20%) relative bandwidth can used for such an experiment and still reproduce a reliable and fairly stable reconstruction. This construction is not a solution to the phase problem however, and hence only provides an improved support constraint for potential further processing.

The second experimental chapter presents novel and currently unpublished work using the high harmonic source to obtain iterative ptychograms of complex-valued extended samples. This represents the first documented result of ptychography using a lab-based source of short-wavelength radiation. Defects in the Molybdenum pinhole used to define the illumination function are investigated and provide a thickness for the defect area of 6 nm $\pm$ 1 nm with a pixel size of 90 nm. The sample under investigation for this experiment was a substrate with fixed cultured hippocampal neurons. An investigation of one of the neurite processes of this sample is made and identification of the neurite as an axon is deduced via analysis of the samples dielectric loss tangent.

Contents

Declaration of Authorship

I, Aaron Parsons declare that this thesis entitled "Coherent Diffraction Imaging using a High Harmonic Source at 40 eV" and the work presented in it are my own and has been generated by me as the result of my own original research.

I confirm that:

- This work was done wholly or mainly while in candidature for a research degree at this University
- Where any part of this thesis has previously been submitted for a degree or any other qualification at this University or any other institution, this has been clearly stated
- Where I have consulted the published work of others, this is always clearly attributed
- Where I have quoted from the work of others, the source is always given. With the exception of such quotations, this thesis is entirely my own work;
- I have acknowledged all main sources of help;
- Where the thesis is based on work done by myself jointly with others, I have made clear exactly what was done by others and what I have contributed myself;

Signed: _____

Date: _____

Acknowledgements

The work shown in this thesis has only been possible due to the support I have received, both academically and on a personal level by many people, which I am very grateful for.

Bill Brocklesby, my supervisor, for getting me into lasers in the first place. Thank you for your patience and guidance over the years. Your attention to detail, and approach to problem solving is something that makes you the great teacher and supervisor you are.

Jeremy Frey, for your infectious enthusiasm and seemingly infinite breadth of knowledge that provided many interesting discussions and investigations.

John Chad, for all the advice on what is and isn't possible with biological specimens. Please forgive my ignorance and stupid questions. You taught me a lot.

Thanks go to all the previous group members that provided the ground work for the research detailed in this thesis. Especially Tom Butcher for teaching me how to get the best out of our laser system, Richard Chapman for his guidance on how to pick the simplest and best ideas for the instrumentation, and Ben Mills for teaching me how to code like a real person, not a student. Also, thanks to Rachel Card who prepared the neuron samples used in this thesis, I thank you for your patience and for explaining to me slowly and patiently exactly how the neurons work.

To the current students Patrick, Hannah, Pete, James for tea, sympathy and asking the awkward questions. I learnt so much from you guys.

I would also like to thank my family. Mum and Dad, your guidance and direction over the years have inspired me to always push myself further, and given me confidence in myself to achieve my goals. To my not-so-little sister Charlie, thanks for all the hugs and chats over the years, they have really helped!

To Ilka, my long suffering partner for putting up with all the late nights and for supporting me through everything. Your patience and kindness make me a better person.

To my son, Sam: You bring so much happiness to everyone that meets you; it makes me so proud. Although you probably didn't realise it, your cuddles and laughter provided some much needed relief during the writing process. I hope I can provide you with as much support and love as your grandparents gave me so that one day you might also realise your dreams.

List of Figures

List of Tables

Chapter 1

Background and Theory

1.1 Introduction

In Feynman's landmark "There's plenty of room at the bottom" paper [1] he outlines why characterising and understanding the world on the microscopic (>400nm) and nanoscopic (<400nm) scale is essential for the progress of science and the general population of the world. Whether it be understanding the nature of processes or structures within biological systems for developing medical treatments, or the inspection of lithographic masks for use in fabricating the ever decreasing scale of micro-electronic/optic devices to keep up with Moores' Law [2], most people rely daily, indirectly, on developing fabrication and characterisation techniques smaller than the unaided eye can observe.

Whilst it is possible to infer some structures indirectly from models built from the spectral response or chemical interactions of materials, these processes are not applicable to general objects, particularly those which consist of large ensembles of atoms of different elements where the interactions soon get very complex. In such cases, it is preferable to observe the object directly via microscopic/nanoscopic profiling of their spatial extent via a variety of complementary techniques.

Microscopy and nanoscopy can be split into techniques that involve probe radiation, and those which do not. Physical probe techniques such atomic force microscopy (AFM) [3, pages 113-155] and scanning tunnelling microscopy (STM) [3, pages 52-112] are typically limited to the surface interaction of the probe with the bound electron wavefunction and hence cannot delve further into the structure than the wavelength of the electron for the material under investigation [4, page 3], although the information they provide about the surface is comprehensive. Instead, for most applications it is

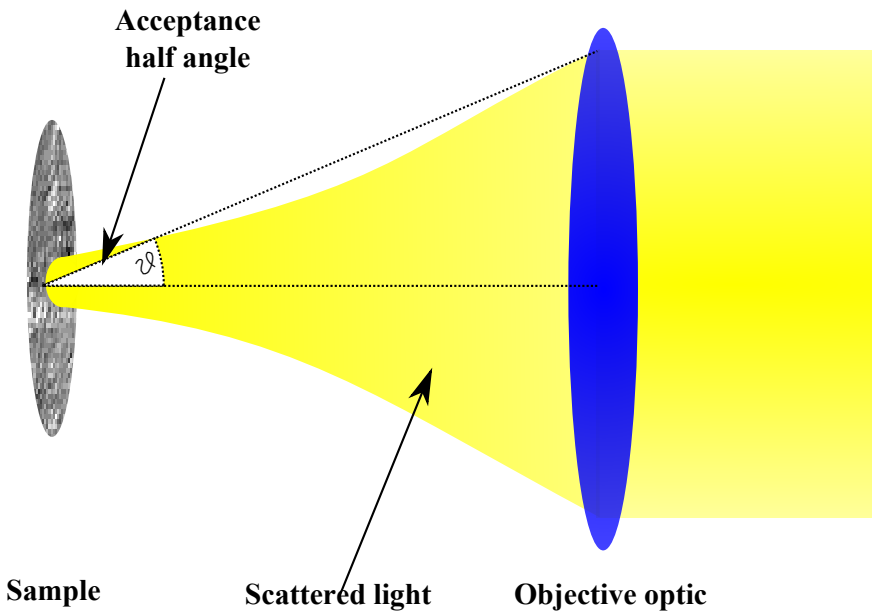

Figure 1.1: The concept of the objective optic in a microscope system. The scattered or emitted light is collected by an objective optic. The resolution of the optic at a given wavelength is determined by the collection half-angle.

preferable to probe the structure with radiation and observe the effects of the interaction.

1.1.1 Microscopy with probe radiation

The probe radiation used for microscopy can be composed of either photons of wavelength λ or, equivalently by the de Broglie relation $\lambda = \frac{h}{p}$ [5] particles of momentum p, where h is Planck's constant. This radiation can either be provided in the form of an illumination of the sample, or by stimulating the sample to emit via some reductive process. After this interaction the light is then collected by an optic as shown in figure 1.1. This optic can take many forms including simple refractive lenses, diffractive optics such as Fresnel zone plates (FZPs, [6]), or, for charged particles electro/magneto-static lenses (EMS, [7]).

In 1874, Ernst Abbe [8] and Herman Helmholtz [9] derived empirically and theoretically respectively the adaptation of Lord Rayleigh's [10] relation to estimating the best resolution of a spectrograph. This 'diffraction limit' can take many forms (discussed in detail in section 1.8), however the simplest form of calculation to find the minimum resolvable feature, δd, investigated at wavelength λ can be expressed as in equation 1.1, where the

NA (Numerical Aperture) is defined as the maximum acceptance cone of an optic with acceptance half-angle θ as shown in figure 1.1.

$$\delta d > \frac{\lambda}{NA} \tag{1.1}$$

For the one dimensional representation given in figure 1.1, the NA can be expressed as $n \sin \theta$, where n is the refractive index of the transmissive medium. This key result states that the resolution of a microscope can be exceeded only by decreasing the wavelength of the probe radiation or by increasing the acceptance half angle of the objective optic.

There are a variety of techniques that involve pushing the validity of this second criterion, the most basic of which is to increase the refractive index of the propagation medium between the optic and the sample to enable light to be refracted into a conventional lens more readily, increasing the acceptance angle of the optic.

It is also possible to gain a higher resolution than this diffraction limit, by decreasing the size of the area of the sample under investigation at a given point. Since the diffraction limit also applies reciprocally to limit the size of the focus for a given wavelength and NA of lens, usually this is achieved by using techniques to gate the emission of light from sub-diffraction-limited size parts of the sample itself.

A popular scanning microscopy technique where this is used to provide an impressive increase in resolution is that of stimulated emission depletion (STED) microscopy. In the simplest version of this technique, molecules attached to the sample of interest are promoted to a higher energy state using one laser colour. A doughnut beam (Laguerre-Gaussian mode, [11, page 586]) is then used to de-excite the majority of these states back down by stimulated emission. The fluorescent signal then corresponds to the signal from molecules that were not de-excited. This is a very accurate technique and can regularly achieve 20 nm positional accuracy (state of the art of 2.5 nm resolution [12]) of such molecules in a range of samples, however they are inherently limited by the absorption depth of the light used as well as the size of the feature that is being used to gate the interaction.

Photo-activated localisation microscopy (PALM) and stochastic optical reconstruction microscopy (STORM) [13], and their many variants, are scanning techniques that can also track the position of objects of interest to much better than the diffraction limit (20nm) [13]. These techniques involve attaching switchable photo-activated fluorophores, of size smaller than the diffraction limit, to the objects. By switching the fluorophores at the appropriate time, the centre-of-mass can be calculated from the recorded signal and hence the position extrapolated beyond the diffraction limit via averag-

ing of the point spread function over many images. This does not provide higher than diffraction-limited resolution of the objects themselves though and usually require the samples to be treated or stained before they are investigated.

It is also possible to decrease the spot size of a probe beam interacting with the sample, a practice exploited in non-linear scanning microscopy (NSM)techniques where either two overlapping beams or a single spatially shaped beam triggers a non-linear process (typically second or third harmonic photon emission). The non-linear process is only able to happen when a threshold intensity is exceeded meaning that the effective spot size is the size of the beam above this threshold. Such techniques regularly reach below the diffraction limit, but are limited to sample types, knowledge of the non-linear properties of the material, which will be different from the material bulk properties. Their is also a hard limit that depends on the damage to the sample as the pump laser power is increased.

Naturally, the scanning nature of these techniques increase the time for each image to be formed and ultimately limit the field of view.

It is also possible to manipulate the illumination wave-vectors such that the waves that would normally be coupled into the evanescent wave-field are instead forced to propagate from the sample. Examples of this are the super-lens [14] and the super oscillating super-lens [15]. These techniques obtain high resolution images of flat test samples, however it is the interaction of this spot with real sample boundaries also impacts this interaction, limiting the resolution and interpretation of the image.

All of these techniques have their merits and pitfalls, and all play an invaluable part of a microscopist's arsenal. However, this thesis is primarily concerned with the other criteria in 1.1. That is: the reduction in wavelength of the probe radiation.

1.1.2 Sources of short wavelength radiation

As outlined in the introduction, both particles and photons can be sources of short-wavelength radiation. Suitable particles include, but are not limited to, electrons, neutrons and both Helium and Gallium ions. However, electrons are by far the most widely applicable and commonly available for use in everyday microscopy due to their ease of production in thermionic emission and manipulation. This section will hence mainly compare the usage of electrons with short-wavelength optical radiation such as extreme ultraviolet (EUV,$\lambda < 50nm$), soft ($\lambda < 10nm$) and hard X-rays ($\lambda < 1\mathring{A}$).

History

X-rays were first documented fully and used in experiments by Nikola Tesla [16], in 1887, although he had not yet investigated their nature, he did take the first ever x-ray images, of his own hand. X-rays were subsequently classified as photons by Wilhelm Roentgen [17] in 1898. Although electrons were experimentally proven to exist by J.J. Thompson in 1897 [18], it took 30 years for the first electron diffraction experiments to be performed [19], confirming their wave-like behaviour predicted by de Broglie's relation. Since the X-rays produced by standard discharge tubes at the time were more penetrating than electrons, they lent themselves more easily towards medical imaging and were almost immediately seized upon for this usage. It wasn't until the advent of modern vacuum equipment in the 1941 that electrons began to be used for imaging experiments [20].

In general there is a large overlap between the use of electron and photons for microscopy. However, it is useful to provide a discussion of the limitations of both techniques.

Fundamentally, since electrons are charged, they interact with both the positively charged nucleus and the negatively charged electrons of sample atoms. This makes the interaction slightly more complex, but much more comprehensive compared to the predominantly electron scattered photons.

However, this more complex interaction does mean that the reduced mean free path before rescattering of a probe electron is much shorter than that for photons. This places a limitation on the thickness of a sample. Typically electron microscopy samples must be a maximum of 100 nm thick, and, for carbon based samples <60nm is recommended [21]. Whilst microtoming is possible, it does change the sample to be imaged due to distortions from the blade used. X-rays and EUV have a much higher penetration and so do not encounter this problem to such a degree. Hard X-rays usually require sample thicknesses between 100 μm - 1 m, soft X-rays 1-50 μm and for EUV 100 nm to 1μm is typical. This makes optical based probing more useful for cultured biological tissue and thicker manufactured thin films.

Radiation damage is a crucial issue for both electron and optical imaging, especially to biological samples, and has been studied in detail for hard [22] and soft [23] X-rays, and also for electrons [24] [25] and, if necessary, cryo-protection is employed. For EUV radiation, damage is less well reported on and primarily focusses either on CCDs in space science [26], or optics for XFEL applications at FLASH [27], neither of which provide suitable comparison to the experiments reported in this thesis. However, we note that during the experiments reported on during this thesis, no radiation damage to the samples was noticed .

It is hence possible to write down some basic and very general criteria with which to assess which probe radiation is best to use for a given sample.

- In general, if a sample can be thinned and stained without too much damage, or if it is thin by nature, it is usually better to image with electron microscopy than optically.
- For thicker samples, where the damage tolerance is not critical, hard and soft-Xrays can be used. Where damage tolerance is critical, the better of the two techniques should be chosen, although for some samples femtosecond imaging such as that carried out at XFELs might circumvent this problem, although they are limited by flux at high resolution.
- If very high resolution is not critical and unstained samples are necessary, EUV imaging can be used.
- If sub-ps time resolution is required then laser based sources can be implemented. HHG sources can reach atto-second time resolution, XFEL's and laser plasma sources can reach 5 femto-second resolution, where electrons are typically limited to ¿100 fs.

1.1.3 Possible sources

One also may wish to consider the accessibility and availability of the source of coherent radiation when deciding which is best for the purpose. Table 1.1 shows a matrix of important parameters.

Property	**Electron Source** (Laboratory based)	**EUV/Soft X-ray** (Laboratory based)	**Soft/Hard X-ray** (Synchrotron/XFEL beamline)
Cost	∼£200k	∼£1m	>£50m
Size	1-2 m	Up to 8 m	>250 m
Access	Laboratory based	Laboratory based	User facility

Table 1.1: Matrix of availability and access parameters for coherent sources of short wavelength radiation

This thesis focusses on a coherent source of lab-based EUV radiation, namely high harmonic radiation, for microscopy.

1.2 High Harmonic Generation

High harmonic generation (HHG) is a highly non-linear coherent optical interaction between an intense electric field and a bound electron that can serve as a tunable, coherent source of short wavelength radiation, extending down to the soft X-ray region of the spectrum.

This section introduces some simple models to provide insight into the nature of HHG radiation and how it may be generated. The practical considerations for the system used at Southampton are outlined and discussed.

1.2.1 The Keldysh parameter

The Keldysh parameter [28] is useful constant to bear in mind when dealing with interactions between atoms and high laser fields, since it provides insight into the nature of the interaction. The parameter is a quantitative measure of the frequency of outer electron tunnelling events (ν_{tunnel}) that occur per half optical cycle, where the frequency of the light is given by ν_{laser} and is given by equation 1.2.

$$K = \frac{2\nu_{laser}}{\nu_{tunnel}} = \left(\frac{I_p}{2U_p}\right)^{\frac{1}{2}} \tag{1.2}$$

Where the ponderomotive potential of the electron in the E-field is given as

$$U_p = \frac{e^2 E_0^2}{4m_e\omega^2} \tag{1.3}$$

Here, e is the charge on an electron and m_e its mass , E_0 is the maximum magnitude of the electric field of the light, and ω the frequency of the driving field.

If $K > 1$ then we are in the regime of *multi-photon ionisation* where the number of tunnelling events per optical cycle is much less than 1. Since the HHG process is dependent on these tunnelling events, the probability of HHG in the multi-photon regime is very low. Instead, HHG happens at the other limit where $K < 1$ generally known as the *tunnelling* regime. The mechanics of this process are explained fully later in this section, but for now we focus on calculating the Keldysh parameter for the laser system used for the work reported here, as is detailed in the next section.

1.2.2 The laser system

To achieve the high field strengths necessary for high harmonic generation, it is possible to use high peak-power ultra-short laser pulses focussed to a highly intense spot. To achieve this it is preferable to separate out the system in to two stages. The first consists of generating pulses with large relative bandwidth (6%) which can be compressed to ultra-short pulse lengths. The purpose of the second stage is to amplify the pulse peak power via a process of chirped pulse amplification.

A schematic and basic block diagram of the laser system owned and maintained by the group is detailed in figure 1.2. A frequency doubled diode pumped Nd:YLF (Spectra Physics Millenia) pumps a Ti:Sapphire (Spectra Physics Tsunami) oscillator which is Kerr lens modelocked [11], initiated by feedback from an acousto-optical modulator (AOM). The spectrum is selected by the slits (S1) to give the shortest pulse whilst remaining stable. The typical output from the oscillator is 5 nJ pulses at 82 MHz repetition rate with a pulse length of 30 fs centred at 790 nm.

The pulses then enter the amplifier system where they are stretched in time by a factor of 10^4 by a grating system before entering another Ti:Sapphire cavity (Spectra Physics Spitfire Pro). This cavity is pumped by a Q-switched frequency doubled laser (Positive Light Evolution) running at 17 W average power and a 1 kHz repetition rate. The infra-red (IR) pulses are switched into the cavity at 1 kHz to overlap with the pump pulses. The switching occurs by rotating the polarisation of the pulses, using a Pockels cell, so that they are transmitted through the thin film polariser. The pulses are kept in using a further Pockels cell and $\frac{1}{4}$ wave plate for 10 round trips when the polarisation is again flipped so that the pulses are coupled out. A compression grating system is used to counteract the dispersion of the stretcher and provides a final output of 40 fs pulses with 3 mJ energy at 1 kHz repetition rate.

The advantage of such a regenerative amplification system is that the oscillator provides a good temporal and spatial profile so that the amplifier can focus on optimising power. Usually, during alignment a good mode quality is preferred to high power. An M^2, a parameter related to the second moment of the spatial distribution of the beam, of 1.6 is typical.

Upon exiting the amplification system a small pickoff is taken for diagnostics. Here a frequency resolved optical gating device (FROG) is used to characterise the temporal and spectral complex fields. The particular FROG used for this project is called a GRENOUILLE (GRating-Eliminated No-nonsense Observation of Ultrafast Incident Laser Light E-fields) and works on a single shot basis, spatially splitting the beam to use it as its own reference. The

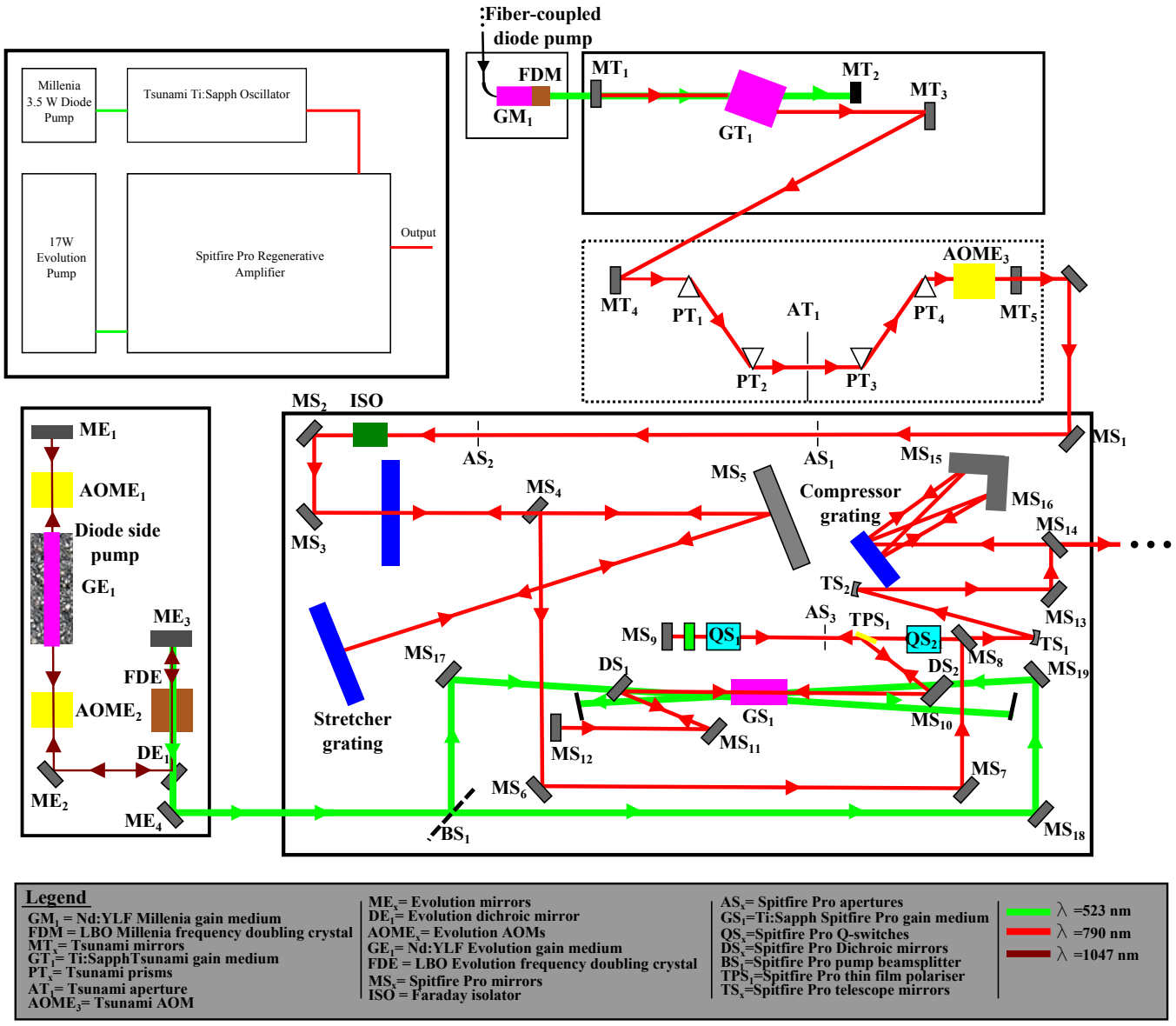

Figure 1.2: The Spectra Physics laser system. Inset: A block schematic of the system showing the Millenia pumped Tsunami oscillator coupling to the Evolution pumped Spitfire Pro regenerative amplifier. Main: A more detailed schematic of the system. The Tsunami Ti:Sapph gain crystal (GT1) is pumped by the Millenia. The dispersion of the Tsunami cavity is then modified by the prisms (PTx) and the aperture (ATx) to obtain stable, high bandwidth pulses. The transform limited pulses then pass in the amplifier, whose Ti:Sapph gain crystal is pumped by the Q-switched Evolution. After being temporally stretched by a factor 10^4 by 4 passes of the stretcher grating, pulses from the 82 MHz oscillator train are then gated at 1 kHz by the Q-switch (QS1), rotating the polarisation to allow transmission by the thin film polariser (TPS1). The pulses are kept inside the cavity for 10 round trips, via a combination of a $\frac{1}{4}$ waveplate and a second Q-switch (QS2). The aperture in the cavity (AS3) allows optimisation of the mode. After the 10 round trips QS2 switches the polarisation of the pulse so that it can exit the cavity. The beam divergence is set by a telescope (TSx) and re-compressed via 4 passes of the compressor grating.

FROG technique solves a similar phase problem to the Gerchberg-Saxton algorithm explained in section 1.5.4, where the magnitudes in both spectral and temporal spaces are measured and constrain the phase such that it can be solved via an iterative principal component analysis (PCA) algorithm- a different class of algorithm to those used to solve the phase problems in the rest of this thesis.

The beam is then split 40:60 into two beamlines. The 40 % beamline (BL2) is used by the group for source development and other investigations concerning the non-linear propagation of the pump pulses in a gas filled capillary [29], however these results are not a subject of this thesis.

Instead, we focus on the 60% imaging beamline (BL1) where the beam is focussed 5° off-axis by a 0° 50 cm focal length mirror to a spot with $w_0 = 25\mu m$ inside a gas cell (section 1.2.4) typically filled with 80 mbar Argon inside a 10^{-6} mbar backing vacuum. The vacuum is necessary to improve the penetration of the strongly absorbed EUV radiation.

For such a gas cell geometry, the gas atoms experience a field strength of $|E| = 9.206$ x 10^{10} Vm^{-1}, providing a Keldysh parameter of 0.0272 putting these experiments firmly in the tunnelling regime where the probability of HHG occurring is much higher.

For each experiment described in this thesis the experimental set up is varied considerably and so this will be explained fully in the experimental sections.

1.2.3 Semi-classical model for HHG

To fully model the process of HHG a quantum model is required. However, whilst this is essential for the source development side of the project, for the work detailed in this thesis a good understanding of the mechanics of the high harmonic process and the characteristics of the generated radiation can be obtained by treating the interaction as semi-classical.

A typical high harmonic spectrum is demonstrated schematically in figure 1.3.

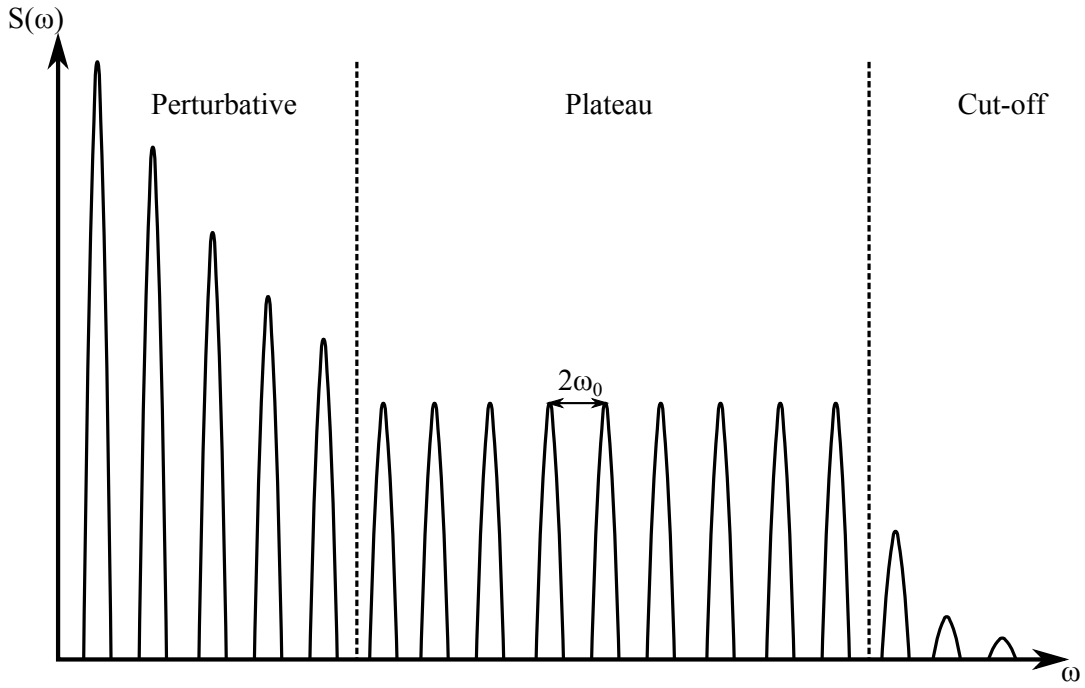

Figure 1.3: A schematic of a high harmonic spectrum. The generation can be separated into 3 main stages according to the energy of the generated photons: perturbative, plateau and cut-off.

Whilst low order harmonics can be treated as a perturbation of the classical atomic polarisation tensor, $P = \epsilon\chi E$, this does not acount for the plateau and cut-off regions observed experimentally.

In 1992, Corkum *et al.* proposed a semi-classical model to describe the various regions where the electronic model can be broken down into 3 main steps: ionisation, propagation in continuum and recombination - as shown in figure 1.4.

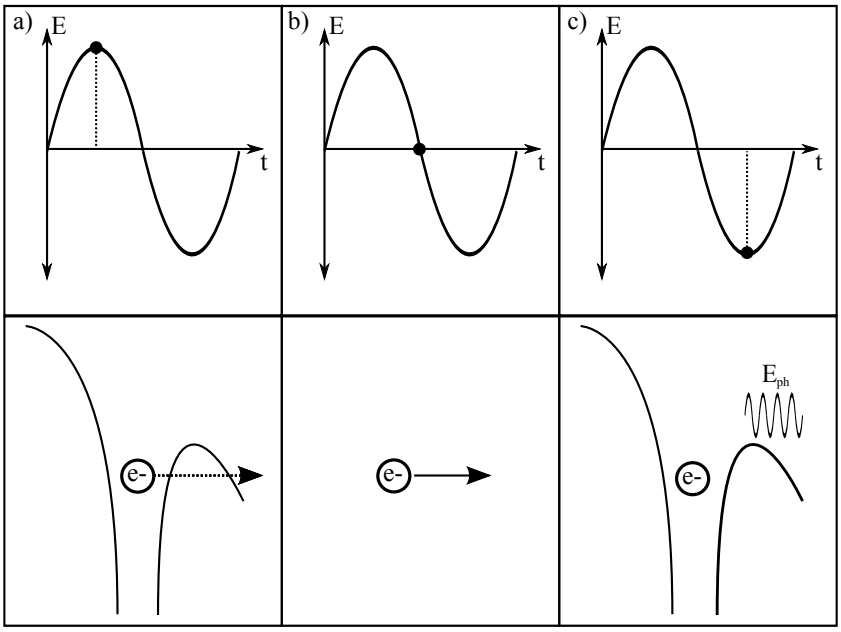

Figure 1.4: The semi-classical method of HHG. a) The electron tunnels through the atoms coulomb potential barrier. b) The free electron is then accelerated in the laser electric field. c) The electron is accelerated back to the parent atom, where it recombines. The interaction releases a photon of high energy radiation.

When a strong laser E-field interacts with an atom, it can distort the Coulomb potential such that an electron can tunnel through the barrier. The propagation of the released electron can then be modelled by considering Newtons equations of motion for an electron travelling in an oscillating E-field, $E = E_0 \sin(\omega t)$.

$$\ddot{x}(t) = \frac{eE_0}{m_e} \sin(\omega t) \tag{1.4}$$

where e is the charge on an electron and m_e its mass. E_0 is the maximum field strength during the interaction, ω is the angular frequency of the laser E-field and t is the time evolution. We have here assumed that at $t = 0$ the electron is at rest at $x = 0$.

Integrating this equation to find the velocity ($\dot{x}(t)$) and displacement $x(t)$ of the electron assuming at the time of release $t_{release}$, $\dot{x}(t_{release}) = 0$ and when the electron returns at t_{return}, $x(t_{return}) = 0$ we obtain

$$\dot{x}(t) = \frac{eE_0}{\omega m_e}[\cos(\omega t) - \cos(\omega t_{release})] \tag{1.5}$$

and

$$x(t) = \frac{eE_0}{\omega^2 m_e}[\sin(\omega t_{return}) - \sin(\omega t) + \omega(t_{return} - t)\cos(\omega t_{release})] \tag{1.6}$$

A plot of the trajectories $x(t)$ is shown in figure 1.5.

It is possible to note several interesting features of figure 1.5. For any electron tunnelling out between 0 and 0.25, and 1 and 1.25 periods of the driving field, the restoring force of the harmonic oscillator will be less than the force exerted by the driving field. This means that the trajectories associated with these release times will result in the ejection of the electron to infinity.

For the rest of the trajectories, since the E-field changes sign every half period of the laser laser, the electron can return to $x = 0$ at twice the laser frequency. The electron is acting as an oscillating dipole, which will radiate and the corresponding radiation will hence be separated by twice the fundamental frequency in the spectral domain at harmonics of the laser frequency. Due to the π phase shift between generation times, the even Fourier components in this transform cancel, and so only odd harmonics are propagated.

To get some idea of what the maximum energy that can be generated is, it is useful to plot the kinetic energy (KE) of the electron trajectories as a function of their travel time, $\tau = t_{return} - t_{release}$. To calculate this, we set $x(t_{return}) = 0$, and substitute $\tau = t_{return} - t_{release}$ into equation 1.6 giving

$$t_{return} = \frac{1}{\omega}\left[\frac{1 - \cos(\omega\tau)}{\omega\tau - \sin(\omega\tau)}\right] \tag{1.7}$$

Substituting this into equation 1.5 allows us to calculate the kinetic energy, which is plotted as a function of travel time in figure 1.6.

We find from figure 1.6 that for any field strength, the maximum of this curve is at 3.17 U_p. Due to the conservation of energy, this gives a maximum photon energy of

$$E_{ph} = 3.17U_p + I_p \tag{1.8}$$

where I_p is the ionisation potential of the atom or molecule and U_p is the ponderamotive potential already defined. This defines our cut-off region shown in figure 1.3, and is the only energy that can be caused by a single time delay.

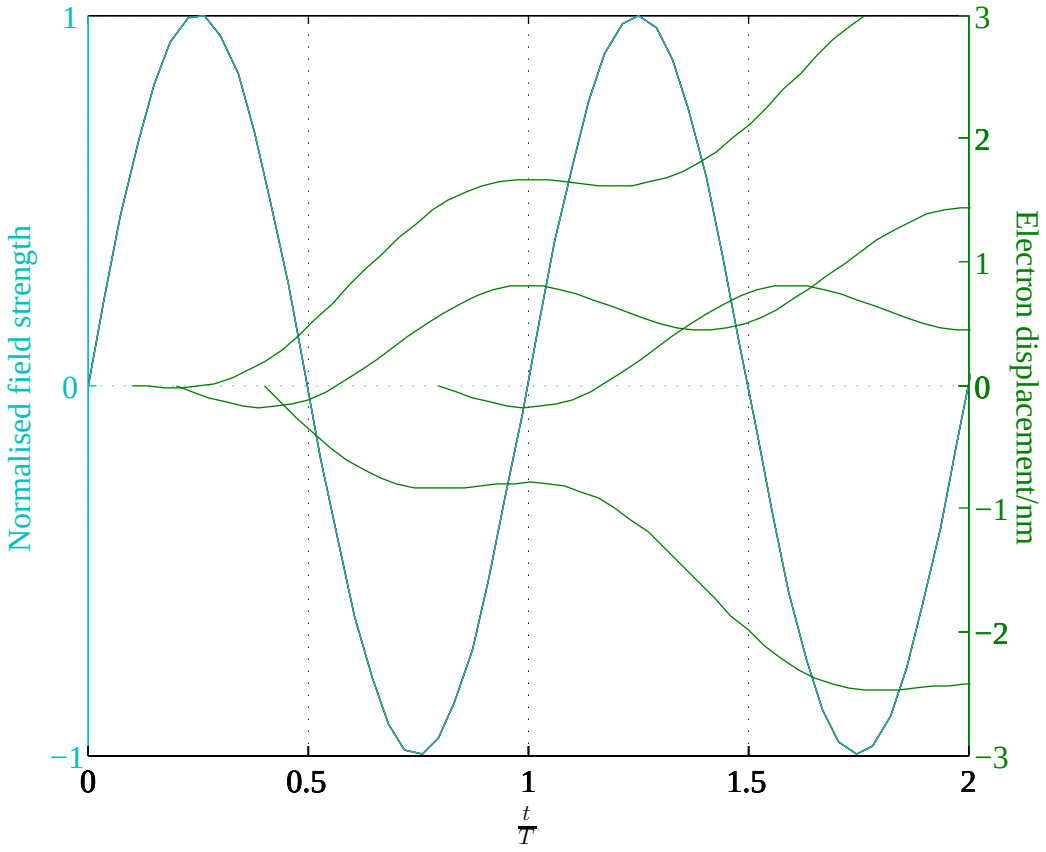

Figure 1.5: The classical electron trajectories as a function of driving field period. Between 0 and 0.25, and 1 and 1.25 periods, the restoring force is not strong enough to bring the electron back to the 0 position. For these trajectories, the electron is ejected to infinity. For the other trajectories, the electron returns and photons emitted.

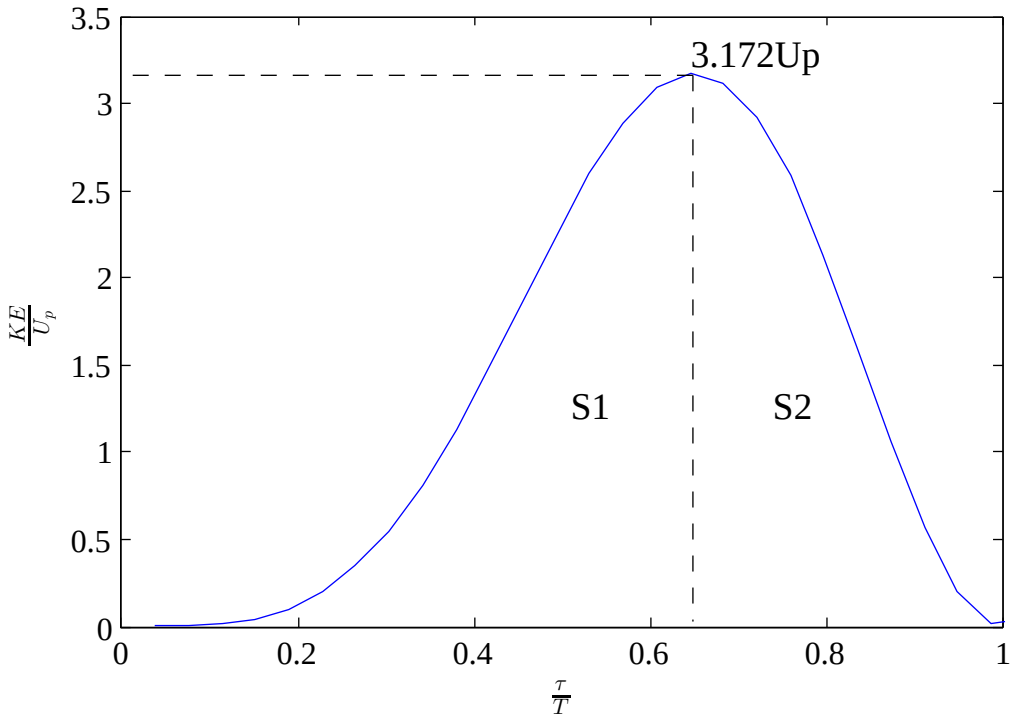

Figure 1.6: A plot of electron travel time vs. electron kinetic energy on its return to $x = 0$. It is shown that the maximum energy is $3.172U_p$ where U_p is the ponderamotive potential of the driving field.

Other energies can be created by 2 different travel times, which we class as the short ($S1$) and long ($S2$) trajectories. These will be discussed further a little later in this thesis.

1.2.4 Phasematching

When ensembles of atoms are considered, the net effect of the of the contributions describe before are affected by their phase in relation to each other. To maintain a continuous build-up of generated radiation, the newly generated light must be in phase with that which is already propagating. In order for this to occur, the phase velocity for the pump frequencies must be the same as for the generated radiation. This is termed "phasematching" and can be expressed for harmonic number q, with wavevector $\mathbf{k_q}$, when pumped with light of wavevector $\mathbf{k_{pump}}$, as a difference in wavevector Δk which must be minimised as described by equation 1.9

$$\Delta\mathbf{k} = \mathbf{k_q} - q\mathbf{k_{pump}} \tag{1.9}$$

Δk is related to the non-linear coherence length l_c, the length over which coherent build up is possible, by the following relation.

$$l_c = \frac{\pi}{|\Delta\mathbf{k}|} \tag{1.10}$$

For the imaging beamline, the generation geometry used is a that of a simple gas cell as shown in figure 1.7, where the generation region is confined to half the non-linear coherence length to optimise harmonic build up.

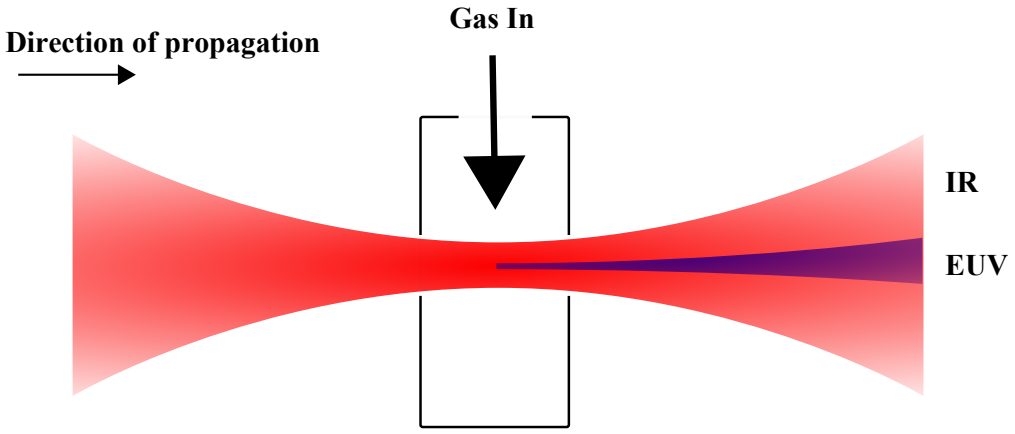

Figure 1.7: The simple gas cell geometry used for HHG during this thesis. Around 80 mbar of Argon flows in from the top of the cell and escapes through the holes in the sides of the cell. The laser beam is focussed through these holes into the gas, where the HHG process takes place.

For this geometry there are contributions to the difference in dispersion from the plasma ($\Delta\mathbf{k}_{\mathbf{plasma}}$), neutral gas ($\Delta\mathbf{k}_{\mathbf{neutral}}$), the focussing geometry ($\Delta\mathbf{k}_{\mathbf{Gouy}}$) and the atomic delay ($\Delta\mathbf{k}_{\mathbf{atomic}}$). $\Delta\mathbf{k}$ can be hence expressed as equation 1.11.

$$\Delta\mathbf{k} = \Delta\mathbf{k}_{\mathbf{plasma}} + \Delta\mathbf{k}_{\mathbf{neutral}} + \Delta\mathbf{k}_{\mathbf{Gouy}} + \Delta\mathbf{k}_{\mathbf{atomic}} \tag{1.11}$$

This section will consider each of these terms in turn and examine their importance and origins.

Neutral gas and plasma terms

The neutral gas term here includes not only the non-ionised fraction of the gas, but also the ions that are left by stripping the electrons from them. Since the pump is far from absorption edges of the Argon gas typically used, the removal of an electron does not change the refractive index of the gas by a large amount. It is therefore common for these calculations [28] to make the assumption that the ionised gas and neutral gas have the same refractive index. In this case the difference in magnitude of the wave-vector due to this effect can be expressed simply as

$$\begin{aligned} \Delta k_{neutral} &= \frac{2\pi q P}{\lambda_{laser}}[Real\{n(\lambda_q)\} - Real\{n(\lambda_{laser})\}] \\ &= \frac{2\pi q P}{\lambda_{laser}}[\delta(\lambda_q - \delta(\lambda_{laser})] \end{aligned} \tag{1.12}$$

Where P is the pressure of the gas, related to the number density of gas atoms.

For the plasma term, the EUV radiation does not interact with the plasma due to its high frequency being far from the plasma frequency of the gas, and so for high order harmonics the additional dispersion is solely due to the interaction of the IR pump with the plasma. The refractive index that the IR experiences is given by

$$n(\omega) = \left(1 - \frac{\omega_{plasma}^2}{\omega_{laser}^2}\right)^{\frac{1}{2}} \tag{1.13}$$

where ω_{plasma} is the plasma frequency given by

$$\omega_{plasma} = \left(\frac{n_e e^2}{m_e \epsilon_0}\right)^{\frac{1}{2}} \tag{1.14}$$

Where, n_e is the number density of electrons, e is the charge on an electron and m_e its mass and ϵ_0 is the permittivity of free space.

The contribution to the phase mismatch is therefore

$$\Delta k_{plasma} = \frac{2\pi q}{\lambda_0}\left(1 - \frac{\omega_{plasma}^2}{\omega_{laser}^2}\right)^{\frac{1}{2}} \tag{1.15}$$

In reality, this statement is actually more complicated since the plasma is time dependent due to the dynamics of the interaction with the pulse. However, for the purposes of the work in this thesis, equation 1.15 is a sufficient model.

Gouy phase term

The Gouy phase is a spatially dependent phase shift experienced by a Gaussian beam through a focus. This is combined with a spherical wave phase term and can be expressed as

$$\exp[i\phi(r,z)] = \frac{1}{2}\frac{1}{z_R + iz}\exp[-\frac{kr^2}{2(z_R + iz)}] \tag{1.16}$$

Where z_R is the Rayleigh range and r is the radial co-ordinate with $r = 0$ defined as being on axis. This can be rearranged to give the phase explicitly as

$$\phi(r,z) = -\frac{1}{2}\left[\underbrace{\frac{k_r^2}{z_R + iz}}_{\text{Spherical phase term}} \underbrace{+i\arctan\left(\frac{z}{z_R}\right)}_{\text{Guoy phase term}}\right] \tag{1.17}$$

The phase mismatch due to the Gouy phase shift can hence be expressed as

$$\Delta\mathbf{k}_{\mathbf{Gouy}}(r,z) = \nabla\phi^{\mathbf{q}}_{\mathbf{Gouy}}(r,z) - q\nabla\phi^{\mathbf{laser}}_{\mathbf{Gouy}}(r,z) \tag{1.18}$$

Due to the reciprocal relationship of the wavelength in equation 1.17, the mismatch due to high order harmonics is very much smaller than that of the fundamental and so is discounted in this analysis. Therefore the total mismatch due to the Gouy phase is given by

$$\Delta\mathbf{k}(\mathbf{r},\mathbf{z}) = \frac{q}{2}\nabla\left[\frac{\mathbf{k_r^2}}{\mathbf{z_R} + \mathbf{iz}} + \mathbf{i}\arctan\left(\frac{\mathbf{z}}{\mathbf{z_R}}\right)\right] \tag{1.19}$$

Atomic phase term

A final term is important in the phasematching process, that of the so-called atomic phase delay. This is caused due to the frequency shift experienced by the travelling part of the electron wavefunction after it has tunnelled out of the atom as it increases its kinetic energy with respect to the bound part. All electron trajectories need to be considered for this term.

Mathematically, this is expressed in terms of the quasi-classical action $s(t_{release}, t_{return})$ where

$$\begin{aligned} s(t_{release}, t_{return}) &= \int_s ds(KE - PE) \\ &= \int_s ds\frac{1}{2}m_e v(t)^2 + I_p \end{aligned} \tag{1.20}$$

for a given kinetic energy (KE) and potential energy (PE), for electrons of mass m_e travelling at a velocity of $v(t)$. The gas ionisation potential is given by I_p.

The atomic phase is hence given by

$$\phi_{at} = -\frac{s(t_{release}, t_{return})}{\hbar} + q\omega t_{release} \tag{1.21}$$

and the contribution to the phase mismatch is

$$\Delta \mathbf{k_{at}} = \nabla \phi_{\mathbf{at}} \tag{1.22}$$

Out of all of these terms, the plasma terms is the one that dominates in a typical gas cell geometry. The remaining terms, in order of most important first, are: the neutral gas term, the Gouy shift followed by the weak atomic phase term.

1.3 Diffractive imaging

As outlined in the introduction of this thesis, the technological difficulties involved in producing EUV /soft X-ray optics of high enough quality to form an aberration free image make it somewhat impractical at present for them to be used in a regular microscopy set-up. This section will discuss the theoretical and practical aspects of diffractive imaging with a focus on techniques used when imaging with high energy photons. The necessity of phase retrieval techniques is discussed and the algorithms used throughout this project are explained.

1.3.1 Diffraction

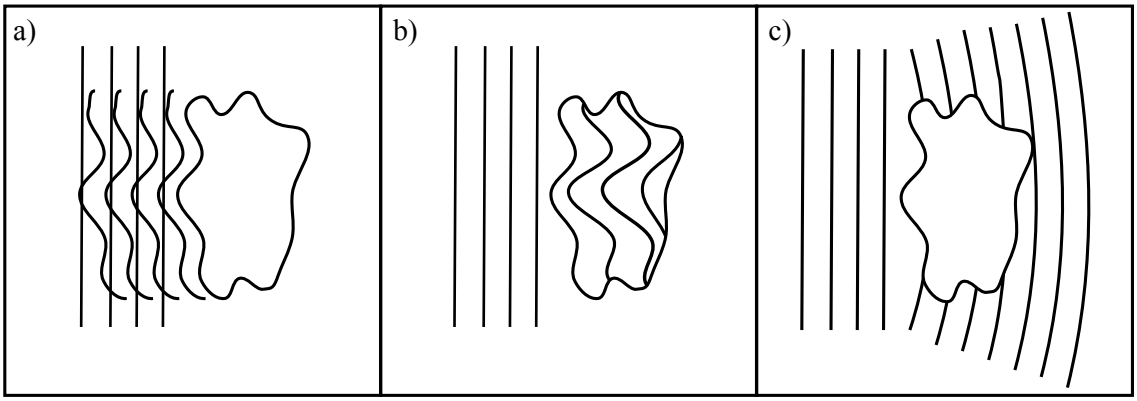

Figure 1.8: The 3 main classes of interactions of light with an obstacle. a) Reflection: The wave vector is reversed and the wave propagates back down the path that it came from with perturbations from the interaction with the obstacle boundary. b) Refraction: Light propagates through the obstacle, but its wavefront is modified according to Snell's law due to the difference in refractive index at the boundary of the obstacle with the external medium.c) Diffraction: The obstacle occludes part of the wavefront, and the light scatters on passing it due to the perturbation.

The behaviour of light at interfaces can be classed as one of three effects: reflection, refraction and diffraction as depicted in figure 1.8.

Reflection is defined here classed as an inversion of one of the wavevectors about an axis of symmetry. Refraction refers to the propagation of light as it passes from a medium of refractive index n_1 to one of refractive index n_2 , which includes dispersive effects.

Diffraction, with which this thesis is primarily concerned, is the effect of the distortion of a barrier on an incident wavefront. Such a distortion can be caused by either positive (particles) or negative (holes) objects which clip the wavefront as it propagates through free space. It is also possible, in any given interaction for light to experience any combination of these three effects. Strictly speaking, the diffraction phenomenon can be split still further, with true diffraction arising from large periodic arrays of scatters. For a single particle, the event is termed scattering. Interference is used to describe situations that lie somewhere between these definitions. Since in this thesis we are mostly dealing with weakly scattering light by aperiodic objects, the term scattering will be used.

The following sections outline the angular spectrum model [30], which is a technique that considers the propagation of the Fourier components of light as it interacts with an obstacle, and provides us with some key results and useful criteria to characterise a given scattering experiment.

1.3.2 The Angular Spectrum Model

The geometry of a typical scattering experiment is show in figure 1.3.2. A plane wave with wavelength λ is incident on a perturbing obstacle in plane S at $z = 0$. The incident wave propagates parallel to the surface normal $\hat{n}$. After interacting with the obstacle, we consider the propagation exit wave field (EWF), which is expressed as $U(x, y, 0)$ until it reaches the plane S' at $z = z'$, where the field distribution can be described as $U(x, y, z')$. In the absence of any strong polarization of the medium which would predispose it to interact with the medium more in one dimension, we can assume the scalar wave approximation. We also make the time-independent approximation; assuming that the situation is static and stationary.

The EWF, $U(x, y, 0)$ can hence be decomposed by Fourier transform into the components of its angular spectrum , $\tilde{U}(\alpha, \beta, 0)$ as given by equation 1.23.

$$\tilde{U}(\alpha, \beta, 0) = \frac{k_z}{2\pi} \int_{-\infty}^{\infty} U(x, y, 0) \exp[ik_z(\alpha x + \beta y)] dx dy \qquad (1.23)$$

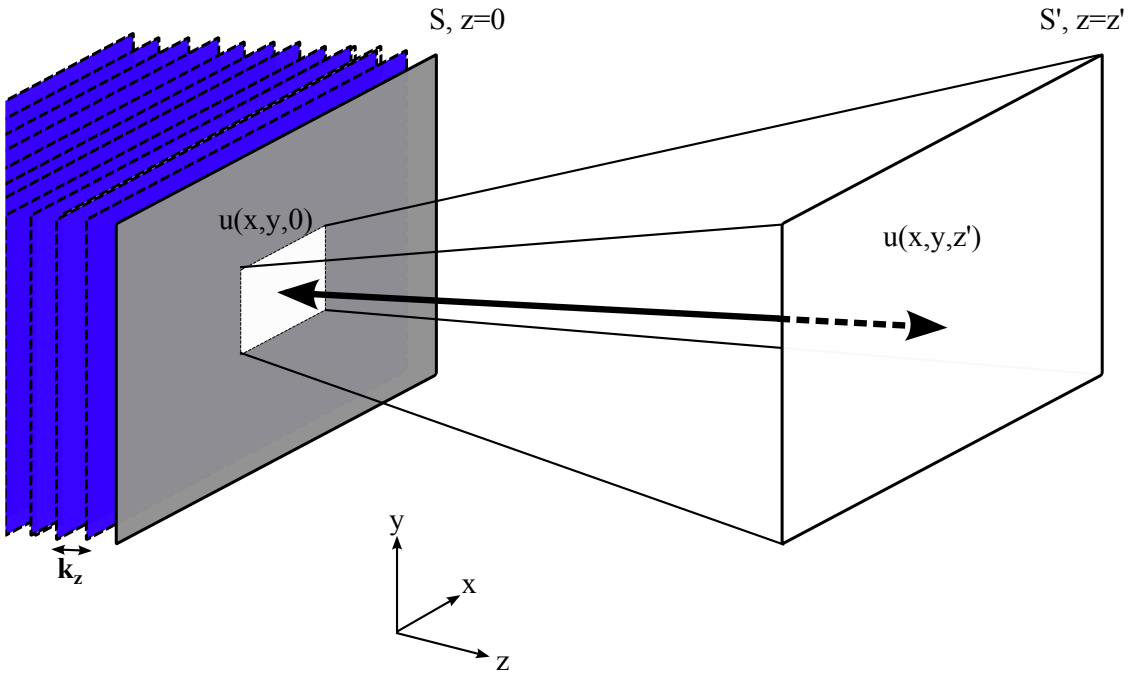

where α and β are the "spatial frequencies" in the x and y directions respectively. Spatial frequencies are related to the spatial period of features contained within the sample bounds.

The angular spectrum model (ASM) has the key result that, the propagation of the angular spectrum by a distance z' can be expressed as equation 1.24

$$\tilde{U}(\alpha, \beta, z') = \tilde{U}(\alpha, \beta, 0) \exp[ik_z z' \{1 - (\alpha^2 + \beta^2)\}^{\frac{1}{2}}] \tag{1.24}$$

Taking the inverse Fourier transform of this provides the spatial dependence of the wave-field at z', as given by equation 1.25.

$$U(x, y, z') = \frac{k_z}{2\pi} \int_{-\infty}^{\infty} \tilde{U}(\alpha, \beta, z') \exp[-ik_z(\alpha x + \beta y)] d\alpha d\beta \tag{1.25}$$

We can learn a lot about the way that the scattered wave is propagating by looking in more detail at the multiplicative factor in equation 1.24, namely the $\exp[ik_z z' \{1 - (\alpha^2 + \beta^2)\}^{\frac{1}{2}}]$ exponential term.

The first interesting case is when $\alpha^2 + \beta^2 > 1$. In this case, the term just becomes an exponential decay. Physically, this describes the spatial

frequencies that are scattered to angles higher than $\frac{\pi}{2}^c$ i.e. the evanescent field.

The next interesting case is when $\alpha^2+\beta^2 << 1$. In this situation, equation 1.23 becomes:

$$U(x,y,z') = \frac{k_z e^{ik_z z'}}{2\pi} \int_{-\infty}^{\infty} \tilde{U}(\alpha,\beta,0) \exp[-ik_z(\alpha x + \beta y)] d\alpha d\beta \tag{1.26}$$

Which is just the Fourier transform of the EWF. This means that when the detecting plane S' is a large distance away from the perturbing obstacle, the relationship between the field at this point and the field at $z = 0$ is just a Fourier transform relationship. This approximation is known as the Fraunhofer condition. In order to clarify what is meant when we say "very far away", we can look still further at the exponential term.

If we assume that α and β are small, but not so small as to be negligible in this term, then we can expand it in a binomial series, so that equation becomes

$$U(x,y,z') = \frac{k_z e^{ik_z z'}}{2\pi} \int_{-\infty}^{\infty} \tilde{U}(\alpha,\beta,0) \exp[-\frac{ik_z z'}{2}(\alpha^2+\beta^2)] \exp[-ik_z(\alpha x+\beta y)] d\alpha d\beta \tag{1.27}$$

where the $O(4)$ terms are sufficiently small enough to be neglected.

If we assume that the perturbing obstacle is the simple case of a square hole with half width a, giving a top-hat output we can substitute into equation 1.27 to give equation

$$U(x,y,z') = \frac{k_z e^{ik_z z'}}{2\pi} \int_{-\infty}^{\infty} \frac{\sin(k_z \alpha a)\sin(k_z \beta a)}{k_z^2 a^2 \alpha\beta} \exp[-\frac{ik_z z'}{2}(\alpha^2+\beta^2)] \exp[-ik_z(\alpha x+\beta y)] d\alpha d\beta \tag{1.28}$$

Since this equation is now separable into spatial frequencies α and β, we can, without loss of generality specify a single axis to investigate, and make a simple substitution to make further manipulation clearer.

$$U(x,y,z') = \frac{e^{ik_z z'}}{2\pi a} \int_{-\infty}^{\infty} \frac{\sin(v)}{v} \exp[-\frac{iz'v^2}{2k_z a^2}] \exp[-iv] dv \tag{1.29}$$

with

$$v = ka\alpha$$

We now introduce the Fresnel number, F defined by 1.30 for the above aperture of half width a at a distance z' illuminated with light of wavelength λ.

$$F = \frac{a^2}{z'\lambda} \tag{1.30}$$

This can be rearranged and substituted into equation 1.29 to give:

$$U(x, y, z') = \frac{e^{ik_z z'}}{2\pi a} \int_{-\infty}^{\infty} \frac{\sin(v)}{v} \exp[-\frac{iv^2}{4\pi F}] \exp[-iv] dv \tag{1.31}$$

This statement in the limit of $F << 1$ reduces back to the Fraunhofer limit as expressed in equation 1.26. As F gets larger the extra term becomes more important, but quite how important depends very much on the geometry of the experiment.

1.3.3 Some useful Fourier relations

Since all of the projections here rely on Fourier transforms, the following sections list some useful relations that can help to further our understanding of the diffractive process. To make the following derivations easier to follow, we define the two dimensional Fourier transform operator $\hat{F}$ and its inverse $\hat{F}^{-1}$.

Shift theorem

The spatial distribution of light at $z = 0$ is described as $U(x, y, 0)$, and its angular spectrum as $\tilde{U}(\alpha, \beta, 0)$. By ASM in the Fraunhofer limit this is also the same as $U(x, y, z')$.

If the distribution at $z = 0$ is shifted in both axes by x' and y', the far-field angular spectrum can be expressed as

$$\hat{F}[U(x-x', y-y', 0)] = \int U(x-x', y-y', 0) \exp[-2\pi i(\alpha x+\beta y)] dx dy \tag{1.32}$$

By changing variables so the $\zeta = x - x'$ and $\xi = y - y'$, we obtain

$$\hat{F}[U(x-x',y-y',0)] = e^{-2\pi i(\alpha x'+\beta y')} \int U(\zeta,\xi,0)\exp[-2\pi i(\zeta\alpha+\xi\beta)]d\zeta d\xi \tag{1.33}$$

Since the integral is now just $\tilde{U}(\alpha,\beta\,0)$, this can be reduced to

$$\hat{F}[U(x-x',y-y',0)] = \tilde{U}(\alpha,\beta\,0)e^{-2\pi i(\alpha x'+\beta y')} \tag{1.34}$$

So a shift in real-space is the same as multiplying the angular spectrum by a linear phase ramp. The relation is also reciprocal. This is an important result for all far-field diffractive imaging techniques since only the magnitude of the angular spectrum is measured, a linear shift in co-ordinates can give the same diffraction/speckle pattern. This ambiguity is trivial to solve by various image registration techniques and so doesn't impact the robustness of the solution.

Convolution theorem

The convolution theorem is paramount to the interpretation of diffraction patterns by eye, and indeed a lot can be gleaned from a result with no post-processing by just applying this theorem.

If we define two functions $a(x,y,0)$ and $b(x,y,0)$ with angular spectrums $\tilde{a}(\alpha,\beta,0)$ and $\tilde{b}(\alpha,\beta,0)$ respectively, then the convolution (denoted by the $\circledast$ operation) of these two functions can be defined by:

$$a(x,y,0) \circledast b(x,y,0) = \int a(x,y)b(x'-x,y'-y)dxdy \tag{1.35}$$

If the Fourier transform of both sides of this relation is now taken, and shift theorem recognised, we arrive at

$$\hat{F}[a(x,y,0) \circledast b(x,y,0)] = \tilde{a}(\alpha,\beta,0)\tilde{b}(\alpha,\beta,0) \tag{1.36}$$

And so the convolution operation is identified as being equivalent to the inverse Fourier transform of the product of the functions respective angular spectra.

Autocorrelation theorem

With the convolution theorem in mind we can note that if function $b(x,y,0) = a*(x,y,0)$ then the following relation holds true.

$$\begin{aligned}\int a(x',y')a^*(x-x',y-y')dxdy &= \hat{F}[a(x,y,0) \circledast a^*(x,y,0)] \\ &= \tilde{a}(\alpha,\beta,0)\tilde{a^*}(\alpha,\beta,0) \\ &= |a(\alpha,\beta,0)|^2 \\ &= |a(x,y,z')|^2\end{aligned} \tag{1.37}$$

Which shows that the inverse Fourier transform of a measured far-field scatter pattern is actually the autocorrelation of the EWF at $z = 0$

1.3.4 Extension to discrete Fourier Transform

All of the above theorems can be extended by various means to cope with the transition between continuous data sets to those that are quantised by discrete measuring processes.

For the case of a scatter pattern measured on a sensor, a CCD for example, the spatial co-ordinates in the sample plane are determined by the highest recorded k-vector

$$dx = \frac{2\pi}{k_{max}} \tag{1.38}$$

where we are assuming a 1-dimensional system, with an element of k-space dk defined as

$$dk = |k|d\theta \tag{1.39}$$

where $d\theta$ is the angular acceptance of a single pixel on the detector and $|k|$ relates to the radius of the Ewald sphere. k_{max} is hence directly related to the total acceptance angle of the detector, $Nd\theta$ for N pixels. For now we assume the detector is curved to match the Ewald sphere. We can rewrite 1.38 as

$$dx = \frac{2\pi}{|k|Nd\theta} \tag{1.40}$$

The associated Fourier transform can be expressed as

$$\tilde{U}(\alpha,\beta,z) = \frac{1}{N}\sum_{x=-\frac{N}{2}}^{\frac{N}{2}-1}\sum_{y=-\frac{N}{2}}^{\frac{N}{2}-1} U(x,y,z)\exp[\frac{-2\pi i(x\alpha+\beta y)}{N}] \tag{1.41}$$

with its inverse transform

$$U(x,y,z) = \frac{1}{N} \sum_{x=-\frac{N}{2}}^{\frac{N}{2}-1} \sum_{y=-\frac{N}{2}}^{\frac{N}{2}-1} \tilde{U}(\alpha,\beta,z) \exp[\frac{2\pi i(x\alpha+\beta y)}{N}] \tag{1.42}$$

This means we can take advantage of the Fast Fourier Transform (FFT) routines outlined by Cooley and Tukey [31, page 395], which instead of inverting the Vandermonde matrices, instead use outer products to circumvent this computationally intensive process by a close estimate. For larger arrays it is more convenient to use general purpose graphics processing units (GPGPU) where the time taken to transfer the data to and from the graphics card is usually less than the time saved in computation. Using GPGPUs for CDI and ptychography means that usually the time bottleneck in the process is usually the time spent acquiring data, rather than that of solving for the phase; a statement that is particularly true for work in the EUV and X-ray regimes where coherent flux can be limited.

1.4 Coherence

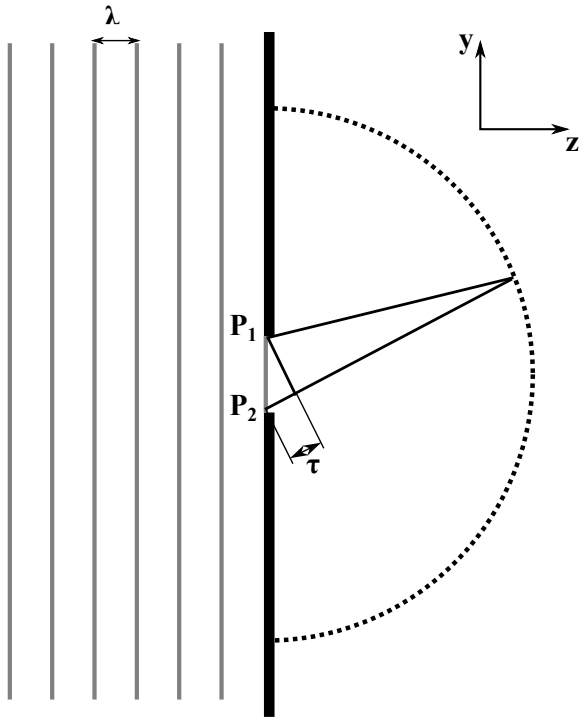

Figure 1.9: A schematic showing the path differences involved in a far-field interference experiment. Light of wavelength λ is incident on an aperture with edges defined by points P_1 and P_2. Waves scattered from these points has the maximum path difference τ.

Coherence is a very important property for diffractive imaging since it determines how well correlated a wave is with either another wave, or the wave itself. If two waveforms are correlated then they can interfere predictably and the previously described relationships hold true.

Since in diffractive imaging we are usually considering the interference of a beam with itself, it is *self-coherence* is the property of interest, and can define the mutual coherence function via the normalised autocorrelation as given by

$$\gamma_{11}(\tau) = \frac{\int a(x', y')a^*(x - x', y - y')dxdy}{a(0, 0)} \tag{1.43}$$

where x and y are defined as the variables under investigation.

Coherence can be explained by considering a simple diffraction experiment as shown in figure 1.9. Plane waves are incident upon an obstacle of width $P_1 - P_2$ and are then scattered into an angular spread. The path difference between scattering points is given by τ, the maximum possible path difference being given by the width of the obstacle. For the resulting scattering to be coherent the incident waveform must therefore be coherent across the maximum path difference. Incoherence in this format is apparent in two different forms; temporal and spatial.

The spatial coherence considers the correlation of the waveform across its spatial extent (y-axis in figure 1.9). It is clear from figure 1.9 that in order for coherent scattering to occur, the wave must be coherent across the entire width of the obstacle. A coherence length $l_{spatial}$ can be defined as the point when the magnitude of the mutual coherence function $|\gamma_{11}(\tau)|$ drops below 0.5. For a HHG source, the driving laser beam is fully spatially coherent, and the generation process maintains this coherence, and so the EUV beam can be considered to be the full width of the beam.

Likewise, the temporal coherence considers the correlation of the waveform across its duration. If the delay time associated with τ between scattered points is greater than the length of time which the wave is correlated with itself, known as the coherence time t_c then incoherent addition will occur for these points. We can associate this with a coherence length $l_{temporal} = ct_c$. For HHG sources, due to their laser driven nature, the temporal coherence length is not a single value since all driving pulses are correlated with each other in time. The limitations of this statement for CDI are examined experimentally in chapter 2.

1.5 Coherent Diffractive Imaging

As the previous section showed, the EWF immediately after the object can be determined by measurement of the field at a plane at distance from the object and inverting the field by the appropriate transform. Experimentally, since detectors count photons and do not measure their state the phase information is lost during detection. It is possible to extract this information by observing the coherent interference pattern produced as a function of delay. The processes of inline holography and Gabor holography are versions of interferometry that encode this phase information into the recorded intensities. The problem can then be directly inverted and the full EWF can be retrieved. However, these processes are ultimately limited by the signal to noise issues.

Instead, it is more common to record the magnitude of the field at z' and

resolve the phases by a process known as phase retrieval. It is by this process that the techniques of crystallography and CDI work.

1.5.1 History

In 1912, Lawrence Bragg successfully showed that it is possible to interpret the far-field diffraction pattern of crystals as reflections from different crystal planes. For simple structures it is sufficient to interpret the diffraction patterns from different sample orientations by eye. However, for more complex structures it is necessary to apply phase retrieval to determine the EWF, which is related to the density of electrons in the object.

The diffraction pattern from a simulated crystal of an acorn (figure 1.10a)) is shown in figure 1.10b).

It is possible to see the Bragg reflections forming in this imaging from the periodic array. The problem with the crystallographic method is that it requires the sample to be crystallised. This is a severe limitation on the nature of samples that can be imaged.

In 1954, shortly after releasing a paper on how to solve the phase problem for crystallography [32], David Sayre suggested that it may be possible to reconstruct the EWFs of aperiodic, non-crystalised objects if the far-field speckle pattern is sufficiently sampled. An example of such a speckle pattern from a non-crystalline object (figure 1.10c)) is shown in figure 1.10d). Sayre took the first ever speckle pattern image of a diatom in 1985 using synchrotron radiation [33], but no reconstruction was attempted from this data. The reason for this was presumably the lack of access to a computer of sufficient power, as well as the fact the fact that phase retrieval algorithms for aperiodic structures were still in their infancy. It took until 1999 for Miao *et al.* to take the first X-ray phase retrieval data and reconstruct it [34].

Even 20 years after Sayre presented his paper on the idea of CDI, many researchers remained unconvinced that unique phase retrieval from such a speckle pattern was possible. Even though the existing crystallographic methods allowed structure determination via phase retrieval, they relied on some fundamental *a priori* information- that the scattering structures were single atoms whose structure factors were fairly well understood. The configuration and molecular morphology of these atoms was the reason why crystallography was necessary.

In CDI, although the structure factors of the atoms are known, the objects under study are made up of many thousands of these and so interference between all of these scattered wavelets are what form the EWF. This is the unknown and is much harder to see a way to reconstruct the EWF uniquely without at least some prior knowledge of its characteristics. Gerchberg and

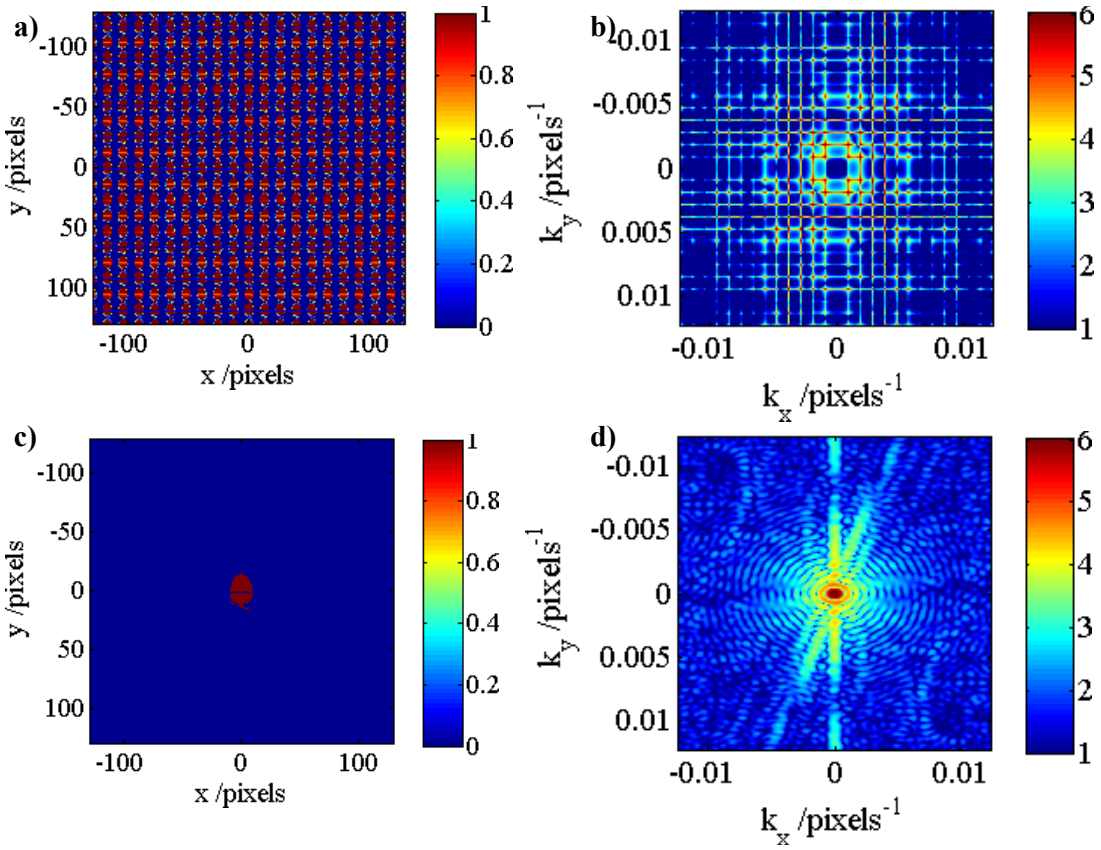

Figure 1.10: Comparison of crystal and aperiodic sample scattering. a)A simulated crystal array of an acorn with b) Its Bragg scatter pattern showing discrete well defined peaks.c) an isolated acorn sample with d) its oversampled speckle pattern. Both scatter patterns have log_{10} colour axes

Saxton (GS) [35], had shown in 1972 that if the field magnitudes in at least two planes were measured then the missing phase information could be reconstructed via an iterative algorithm. Fienup then formulated a modified version of the GS algorithm, whereby the initial realspace guess, otherwise known as the "support" was just a non-zero region inside a zero padded realspace [36]. This technique is termed "error reduction" (ER) and was the first *a priori* phase retrieval algorithm. In the same paper, Fienup then went on to improve this algorithm by including information from the previous iteration in the update for the next.

Since these algorithms were designed, understanding of 2-dimensional phase retrieval has leapt forward. The next sections put forward a formalism for the algorithms used in the work detailed in this report and detail the nature of their origin. First, however, we discuss the nature of the support and how this determines the required sampling of the signal in Fourier space.

1.5.2 Sampling requirements

The scaling of realspace in relation to Fourier space are given by equation 1.40. It is clear from this that the pixel spacing in one of these domains is inversely proportional to the total field of view (FOV) in the other. So the number of pixels in real space that lie outside of the support and provide no extra information for our reconstruction are actually working to sample the data points in Fourier space more finely. Indeed, it is upon this basis that Fourier based data smoothing works [31, page 495]. The effective redundancy of points, given by equation 1.44, is referred to as the oversampling ratio O.

$$O = \frac{\text{Total number of pixels}}{\text{Number of pixels inside the support}} \tag{1.44}$$

Now we have outlined this relation, the important task is to find out what oversampling factor is necessary for the recorded data to contain enough information to reconstruct the input faithfully.

If we consider the case of a 1-dimensional object as shown in figure 1.11a), with recorded diffraction pattern shown in figure 1.11b), the spatial autocorrelation of the object given by equation 1.37 allows a maximum space for the object to exist within as shown by figure 1.11c). Therefore, in order to appropriately sample all of our intensity data once, a real-space field of view is required that contains the entire autocorrelation: twice the width of our object. This sets the number of pixels per fringe in Fourier space. In actual fact, to prevent aliasing, the signal should be sampled at twice the Nyquist frequency, giving an oversampling factor of 4. Since interesting EWF's for use in CDI are actually complex valued, and the width of the autocorrelation

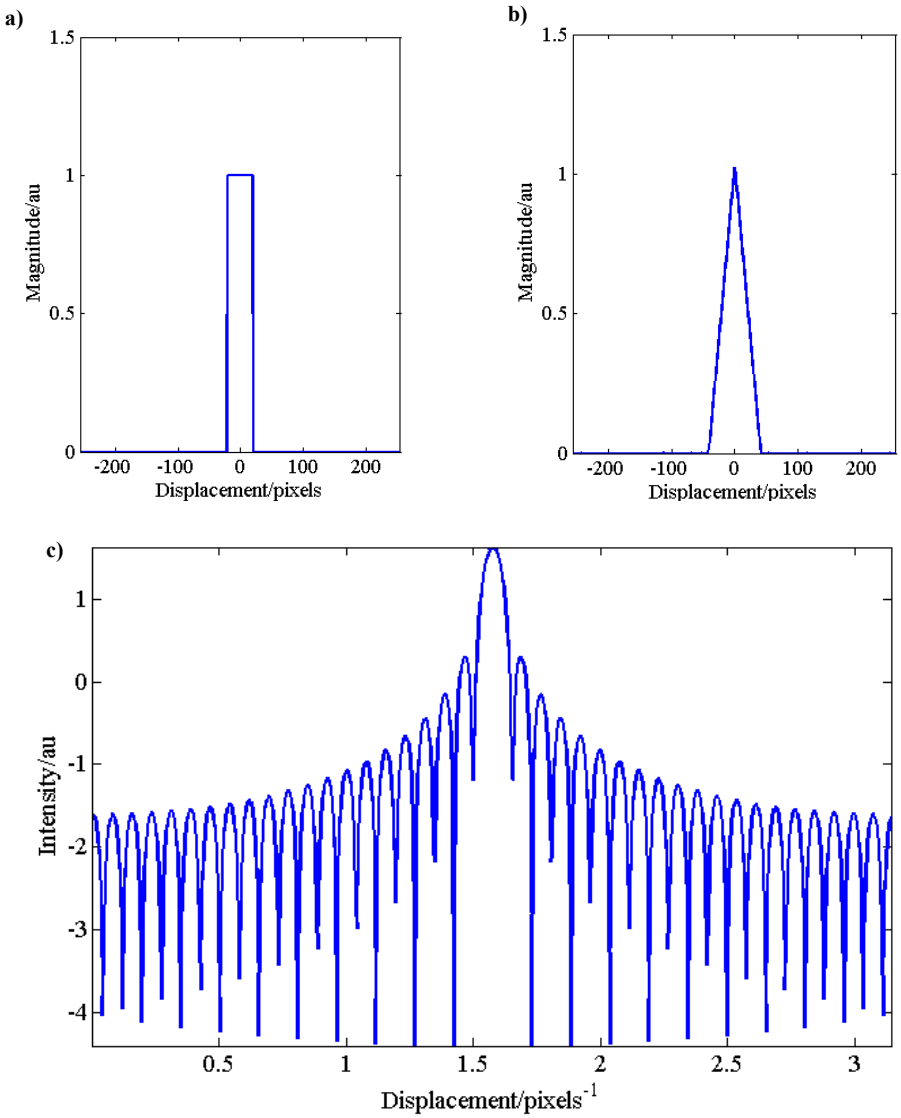

Figure 1.11: The 1-dimensional oversampling criterion. a) A simple object. b) The autocorrelation of a) showing the minimum area we can suppose a) will take up in realspace. c) The speckle pattern (with amplitude on log_{10} scale.

also depends on the phase information, the minimum 1-dimensional oversampling ratio required is usually taken to be 5 [37]. It is actually possible for this reason to use a thresholded autocorrelation as the support for a phase retrieval routine [38], so long as the oversampling condition is met.

Now, if we try to generalise this rule to higher dimensions, a first approximation [ref] is that we must oversample by the same criteria as the 1-dimensional case, but in each of the additional dimensions. For example, a 2-dimensional signal would have to be over-sampled by 5 in the x dimension, and 5 in the y dimension. However, Miao *et al* [39] pointed out in 1998 that, since in n-dimensional space, each voxel is constrained n times, the signal actually needs to be sampled less finely in each dimension by a factor of $\sqrt{n}$.

1.5.3 The modulus constraint

For all CDI phase retrieval problems, the hard constraint on which all reconstructions are based is that of an oversampled field-intensity measured at a given point. For this project the measured intensities are the square far-field magnitudes measured in the Fraunhofer regime. This gives a definite value that we know the recovered EWF must fit to be a solution to the phase problem.

For this case we can define the modulus constraint by the projection onto the set for all possible solutions (x equation 1.45) that fulfil the condition of matching the measured field magnitudes when propagated to Fourier space.

$$P_{mod}(x) = \frac{\sqrt{I_{Fourier}}\hat{F}[x_m]}{|\hat{F}[x_m]|} \tag{1.45}$$

where $\hat{F}$ is the Fourier transform operator in this case. Indeed this operator can change for difference geometries, but in general is the operation that minimises the distance to project on to each of the sets involved. $I_{Fourier}$ are the measured Fourier-space magnitudes.

With this as a given, the next stage of applying a constraint on the realspace projection can be approached in a number of different ways. Once these have been defined, the updated iterate can then be formulated. In the following sections a number of these methods are demonstrated.

1.5.4 Gerchberg-Saxton and ER algorithms

The original Gerchberg-Saxton (GS) and Error Reduction (ER) algorithms for CDI work under the same basic principles, but with slightly different support set projections.

The realspace projection

For GS, we can define the following realspace projection, where I_r are the measured realspace field magnitudes.

$$P_{rs}(x') = \frac{\hat{F}^{-1}[x']\sqrt{I_r}}{\hat{F}^{-1}[|x'|]} \tag{1.46}$$

where $\hat{F}^{-1}$ is the distance minimising *inverse* Fourier transform operator.

For the case of ER, where the support constraint is not measured, we instead define a guessed support D, and change the realspace projection to

$$P_{rs}(x') = \hat{F}^{-1}[x'] \ \in D \tag{1.47}$$

$$P_{rs}(x') = 0 \ \notin D \tag{1.48}$$

The update

The iterative update for both of these algorithms is achieved by applying the above projections in turn to the current iterant g_k, as given by equation 1.49. This gives the updated iterant x_{n+1} for iteration number n.

$$g_{k+1} = P_{rs}[P_{mod}(g_k)] \tag{1.49}$$

To get a feel for how this type of algorithm behaves, figure 1.12 shows a simple example of two complex sets represented by lines on an Argand diagram. The point that fits both sets is at the intersection of the two lines.

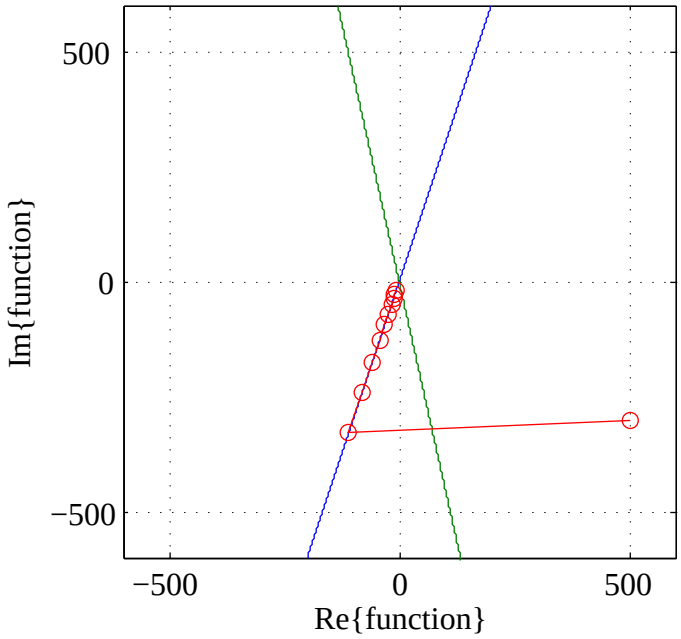

Figure 1.12: The convergence of the Gerchberg-Saxton/Error reduction algorithms in the simple case of two complex-valued line functions in the presence of one minima. Starting from a random point, the algorithm projects on to each set in turn, minimising the distance between each point. The algorithm converges at the crossing point since this is where the distance between projections is minimised. The iteration at each step is plotted here.

The algorithm starts from a randomly generated point and is projected onto each set in turn by minimising the distance between the set and the current projected point. As is clearly shown in figure 1.12, each iterant moves along one of the sets until it reaches the point when successive iterations have no additional effect. This point is the intersection between the two sets.

For such a simple problem, this approach is ideal since it finds the nearest minimum in constraint space. However, for more complex problems, in particular for those that are non-convex [40, Chapter 1] such as that shown in figure 1.13, this can cause stagnation of the algorithm in local minima which are dependant on the starting point chosen. For such problems, these algorithms are a good part of the solution process, but other algorithms such as those discussed in the next section are required in order to find global minima.

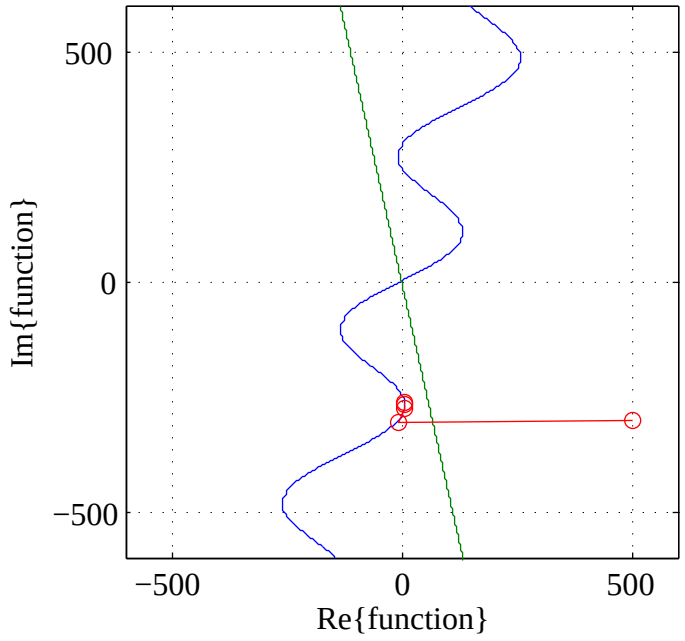

Figure 1.13: The convergence of the Gerchberg-Saxton/Error reduction algorithms in the simple case of two complex-valued line functions in the presence of a local minimum and a separate, global, minimum. Here, the algorithm has converged on the local minimum, a pitfall of these types of algorithms.

1.5.5 Hybrid Input/Output

The idea of a Hybrid Input/Output (HIO) algorithm was first proposed by Fienup in 1978 [36]. The basic concept is to use feedback from the previous iterant to update the solution. The idea is to prevent stagnation and the missing of global minima that are experienced in GS and ER. HIO is actually a special case of a family of algorithms called difference maps as we will see in a later section.

The realspace projection

For the HIO algorithm we can define a realspace projection P_{rs} that can be defined by the following equation for the m^{th} iteration.

$$P_{rs}(x'_m) = \hat{F}^{-1}[x'_m] \ \in D \tag{1.50}$$

$$P_{rs}(x'_m) = \hat{F}^{-1}[x'_m] - \beta\hat{F}^{-1}[x'_{m-1}] \notin D \tag{1.51}$$

where β can be any positive or negative value, but $\beta = 0.9$ is the most typical value for work in this thesis. As with the previous section, D here represents the support in realspace.

The update

As with the GS and ER algorithms, the update for the next iterant g_{k+1} is just given by applying each of the projections in turn to the current iterant g_k.

$$g_{k+1} = P_{rs}[P_{mod}(g_k)] \tag{1.52}$$

If we again apply this to our basic model of the intersection of two complex lines, the convergence path is shown as in figure 1.14 below.

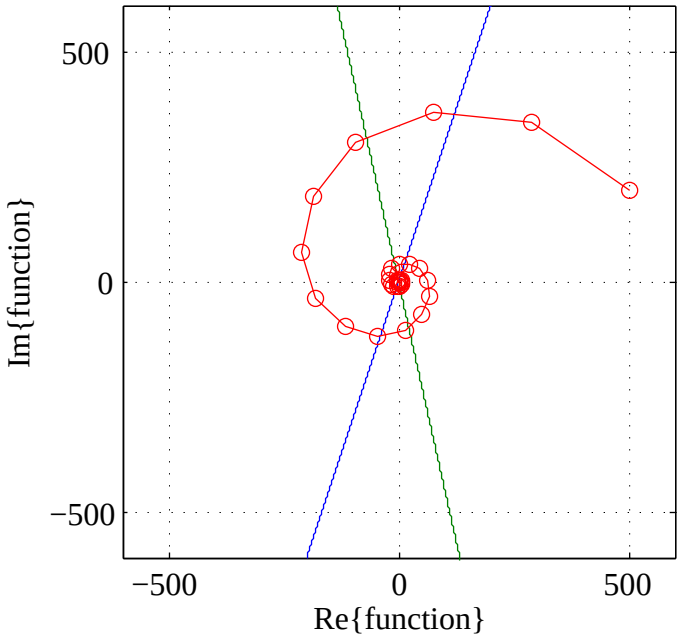

Figure 1.14: The convergence of the Hybrid Input/Output algorithm in the simple case of two complex-valued line functions in the presence of one minima. Starting from a random point, the algorithm projects on to both sets simultaneously. The difference between both of these projections is then taken, scaled according to a feedback constant, and added to current iterate. The algorithm converges at the crossing point since this is where the distance between projections is minimised, and hence the feedback tends to zero.

This algorithm does not keep the iterate constrained to the individual sets themselves, but instead is free to roam the complex space. This gives it the opportunity to explore all possible minima that could exist before converging on a global minima. Figure 1.15 shows the convergence of the HIO algorithm but for a situation where there are local minima. The iterate is actively repelled from the local minima, allowing it to explore and find the global minima. This makes it much more useful for non-convex problems such as that 2-dimensional phase retrieval. In reality this is used in combination with the ER algorithm, switching between them until the best fit to the data is found.

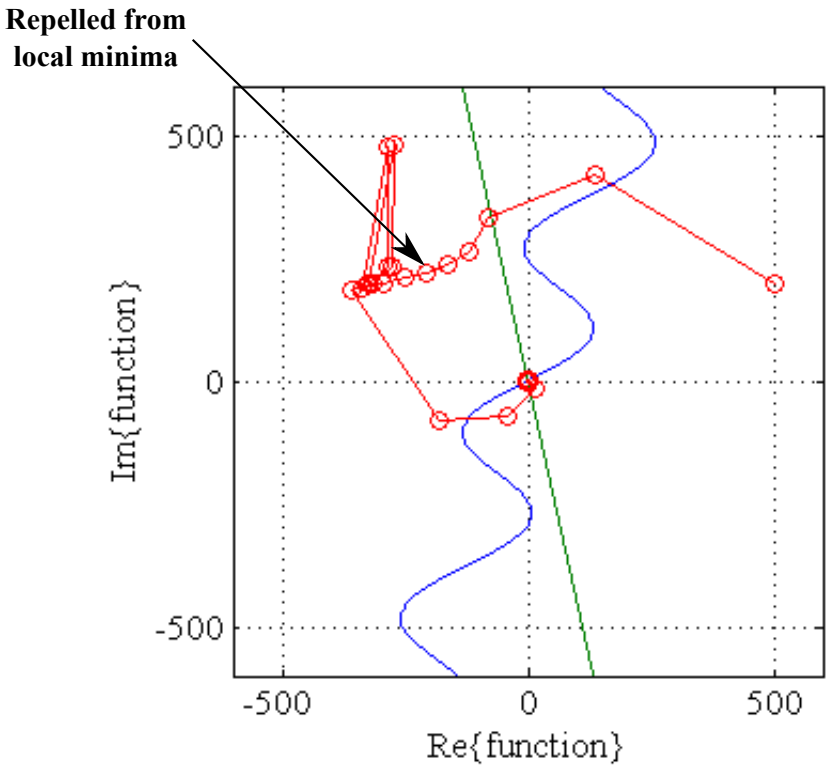

Figure 1.15: The convergence of the Hybrid Input/Output algorithm in the case of two complex-valued line functions in the presence of a local minima and seperate global minima. The algorithm is actively repelled by the local minima, since the distance between the two projections on to the sets at this point stays constant, and does not decrease to zero. The iterate is then attracted to the true global minima, where the difference tends towards zero.

1.5.6 Difference Maps

As previously mentioned, the HIO algorithm is a specific case of a class of algorithms referred to a *difference maps* (DMs). The DM method outlined in this section is that proposed by Veit Elser [41] and expounded upon by Pierre Thibault in his thesis [42].

The DM method comprises of taking increasingly more accurate estimates of the search space, the difference of which informs the update of the iterate.

Projections and estimates

For the case where the minimising projector is a Fourier transform, we can define the projections to each set as equations 1.53

$$P_r s(x) = \hat{F}[x] \tag{1.53}$$

and as shown in equation 1.54

$$P_{mod}(x') = \frac{\sqrt{I_{Fourier}}\hat{F}[x']}{|\hat{F}[x']|} \tag{1.54}$$

These projections are then applied to the current iterate to give two estimates y_1 and y_2

$$y_1(x) = P_{rs}[(1+\gamma_2)P_{mod}(x') - \gamma_2 x'] \tag{1.55}$$

$$y_2(x) = P_{mod}[(1+\gamma_1)P_{rs}(x) - \gamma_1 x] \tag{1.56}$$

where γ_1 and γ_2 are real-valued feedback constants which we will explore shortly.

The update

The update of the iterate for the DM method then used the difference between these two estimates to inform the feedback in the algorithm. This can be expressed for iteration number n as

$$x_{n+1} = x_n + \beta(y_1 - y_2) \tag{1.57}$$

This convergence is shown for our simple two line problem in figure 1.16 for a variety of different parameters. For $\beta = 0.9$,$\gamma_1 = \frac{1}{\beta}$ and $\gamma_1 = -1$, the difference map takes on the same characteristics as the HIO described previously a result that is proved combinatorially in [42].

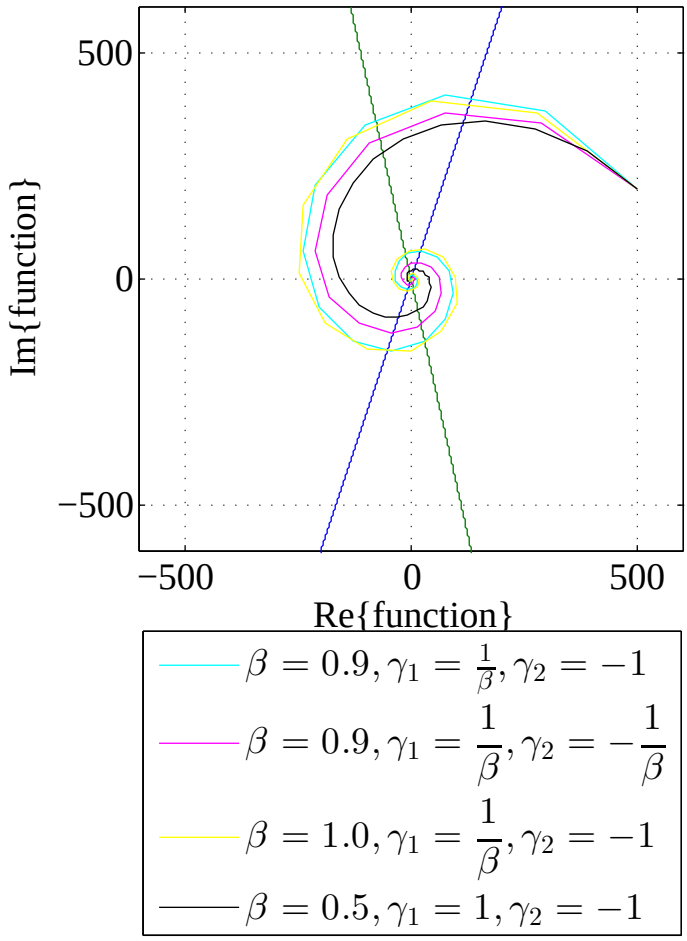

Figure 1.16: Difference map convergence on the intersection of two simple complex sets. It is seen that by changing either the value of the β or the γ coefficients, it is possible to change the size and how compressed the search space is.

The key thing to note about all difference map techniques is their propensity to avoid traps in local minima (demonstrated by the parameters plotted in figure 1.17), predominantly because the iterate is not actually itself confined to either of the sets. The size of the region of constraint space that is explored by the algorithm is defined by the γ and β coefficients, and so can

be tuned according to the particular problem. The solution is found when the difference between the estimates goes to zero (or below a preset noise threshold). At this stage, the iterate can be projected on to either one of the two sets to obtain the solution.

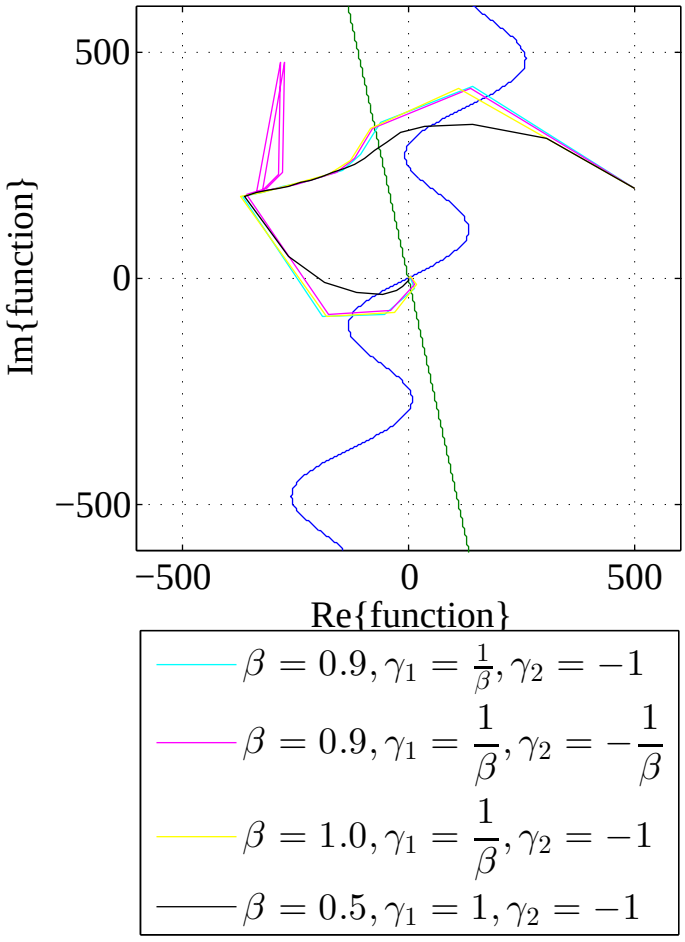

Figure 1.17: Difference map convergence on the intersection of two simple complex sets in the presence of both a local and global minima. It is seen that by changing either the value of the β or the γ coefficients, the convergence path is altered, but the iterate is always pushed away from the local minima and attracted towards the global minima.

1.5.7 Additions: Reducing the support

Whilst it is theoretically possible for combinations of the above CDI algorithms to converge to a solution with any initial support after a significantly high number of iterations, issues such as twinning and phase vortices [43] can cause a failure to converge. Unaided, this makes the choice of the support set a critical variable.

There have been various attempts at modifications to the phase retrieval 'recipe' that aim to change the support set as the algorithm iterate evolves, to provide a better constraint.

One of these methods was introduced by Fienup in 1999 and is known as the *reduced support method* [44]. This technique is specifically targeted at reducing the impact of the twin image problem on the convergence path. The concept is that after a fixed number of iterations of phase retrieval starting from an initial support of the object's autocorrelation, the support is halved in area for a small number of iterations before reverting to the original support constraint. The idea is to bias the solution towards a particular orientation in real-space; an idea that seems to work well in the literature.

For the work carried out in this thesis, another method designed by Marchesini *et al* [45] termed 'shrinkwrap' is used. This technique again involves reducing the support after a given number of iterations of HIO, typically 50 for the experiments detailed in this thesis. The idea is to improve the estimate of the real-space constraint by convolving the current iterate's amplitude with a normally distributed intensity mask with a small FWHM - typically 3-5 pixels - before thresholding to give a hard edge. This has the effect of blurring out the current solution, allowing room for relaxation of the next iterate, whilst biasing the current solution to a particular spatial distribution.

The shrinkwrap method has been adopted for reconstructions used in this thesis since it seems to work best for the data acquired.

1.6 Iterative Ptychography

Ptychography was initially conceived, in a similar fashion to holography, to overcome technical limitations of the resolution due to lens aberrations of scanning transmission electron microscopy (STEM) [46]. Broadly speaking, ptychography is a method of solving the phase problem by inverting a series of scatter patterns (in either the near or far field) to recover the complex transmission function of an object via the use of the convolution theorem, overcoming the inherent phase ambiguities in phase retrieval by modifying

the probe in a known way [47].

Most commonly, and for the case of the research detailed in this thesis, the probe modification is achieved by a lateral scanning of the probe relative to the sample in overlapping steps (see figure 1.18 with the deconvolution hence making use of shift theorem (section 1.3.3).

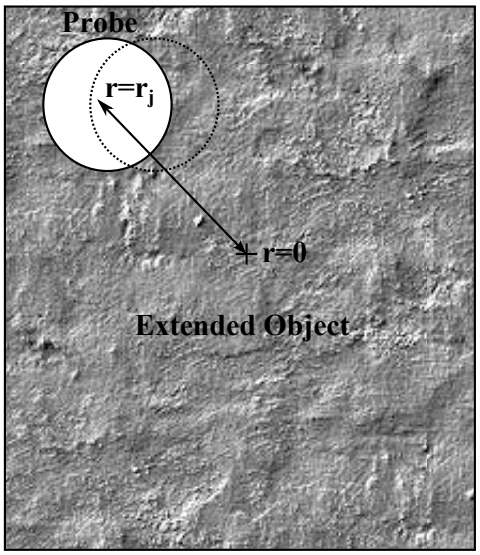

Figure 1.18: The basic premise of iterative ptychography. An extended object is scanned by apertured illumination at overlapping regions in real-space and the respective speckle patterns recorded. The phase is then solved for algorithmically.

Whilst direct inversion is indeed possible [48], a far more robust and commonplace methodology is to solve the problem iteratively. The first example of such a solution was shown by Rodenburg in [49] using the ptychographic iterative engine [PIE]. This first algorithm, whilst successful, requires very accurate knowledge of both the incident probe and the stage positions, which limit the possible resolution of the reconstruction.

To alleviate the problem of knowledge of the probe, a further extended ptychographic iterative engine (ePIE, [50]) was developed. Other algorithms were also developed independently of this [51], based on the difference map formulation shown in section 1.5.6. Furthermore, it was then shown that, due to the huge constraint provided by both the recorded data, and the scanning overlap, knowledge of the probe positions was also not required in such depth, and could in fact be retrieved in the algorithmic process without any further a priori information [52]. These two advancements made the

use of iterative ptychography for high resolution microscopy a completely standalone technique.

Since these developments, it has also been shown that iterative ptychography is somewhat immune to partial coherence in both spatial and temporal domains by a modal decomposition of the probe [53], [54]; an addition that has proved especially useful in the synchrotron community where coherent flux can be a limitation.

Finally, and most recently, it has been shown that, since the probe part of the convolution also includes the shift, and is hence 4-dimensional, the tradition CDI requirement of Nyquist sampling of the recorded intensities is lessened so long as the step size is decreased appropriately [55], [56].

Since its initial use in electron microscopy, the application of iterative ptychography to various material science and biological problems is a fast growing technology in optical and X-ray fields. Indeed there is even a company (Phase Focus Ltd, [57]) based on providing optical instruments for such purposes. At the cutting edge of present X-ray research in iterative ptychography are the team at the cSAXS beamline at the Swiss Light Source, who can currently achieve 11 nm resolution in their planar reconstructions [58], and 16 nm voxel size when combining ptychographic reconstructions of rotational projections with tomographic reconstruction techniques [59]. There is also a considerable push to apply iterative ptychography with laboratory based sources of short wavelength resolution, such as the work shown in chapter 3 of this thesis.

The following section describes the two most commonly used variants of iterative ptychographic algorithms as mentioned above; namely Rodenburg's ePIE and Thibault's difference map method.

1.6.1 Difference Map method

The difference map method for iterative ptychography is of a similar format to that described for CDI, but with a few alterations to the updates.

The Projections

As always with the phase retrieval routines the dominant constraint is that of the modulus constraint given here as a reminder as

$$P_{mod}(x) = \frac{\sqrt{I_{Fourier}}\hat{F}[x]}{|\hat{F}[x]|} \tag{1.58}$$

which must be true for all Fourier projected views.

For the difference map routine, the support projection for each view is defined as being the product between the object and probe wave fields. For the j^{th} view with the probe at displacement r_j these can be expressed as

$$P_{rs} = \hat{P}(r - r_j)\hat{O}(r) \tag{1.59}$$

where $\hat{O}$ and $\hat{P}$ are defined as follows

$$\hat{O}(r) = \frac{\sum P^* x_j(r)}{\sum |\hat{P}(r - r_j)|^2} \tag{1.60}$$

and

$$\hat{P}(r) = \frac{\sum O^* x_j(r)}{\sum |\hat{O}(r + r_j)|^2} \tag{1.61}$$

The Update

We again define our two estimates y_1 and y_2, but here we set $\gamma_F = -1$ and $\gamma_{RS} = \frac{1}{\beta}$ and $\beta = 1$ as the most common values used [51].

$$\begin{aligned} y_1 &= P_{RS} x \\ y_2 &= P_F[2P_{RS}x - x] \end{aligned} \tag{1.62}$$

The update is then given as

$$\begin{aligned} x_{n+1} &= x_n + y_2 - y_1 \\ &= x_n + P_F[2P_{RS} - x_n] - P_{RS}x_n \end{aligned} \tag{1.63}$$

For this algorithm the updates are carried out every full iteration of the algorithm and so it not so prone to stagnation in local probe iterate minima.

1.6.2 Extended Ptychographic Iterative Engine

The ePIE routine has a different approach to that of the DM routine, which will be described here.

The Projections

The real-space projection, is very similar to that for the DM routine, except applied at every view instead of every iteration. The real-space projection is hence expressed as the EWF for the j^{th} view, $\psi_j(r)$

$$\psi_j(r) = O(r)P(r - r_j) \tag{1.64}$$

The Update

In difference to the DM routine, each iterate is actually confined to the constraint sets. For this reason, the Fourier transform operators must be included in the updates for p_{mod} to still be valid.

$\hat{O}(r)$ and $\hat{P}(r)$ are defined very differently to the DM routine with

$$O_{j+1}(r) = O_j(r) + \alpha \frac{P^*(r - r_j)}{|P(r - r_j)|^2_{max}} [\hat{F}^{-1}[p_{mod}(\hat{F}[\psi_j(r)])] - \psi_j(r)] \quad (1.65)$$

and symmetrically

$$P_{j+1}(r) = P_j(r) + \alpha \frac{O^*(r + r_j)}{|O(r - r_j)|^2_{max}} [\hat{F}^{-1}[p_{mod}(\hat{F}[\psi_j(r)])] - \psi_j(r)] \quad (1.66)$$

Since the iterate is confined to each set in turn in ePIE, and also due to the update of the probe at each view, the convergence of this algorithm can be thought of as being closer to that of ER for CDI and can be more prone to stagnation in local minima. However since the phase problem for ptychography is so over-constrained, the difference between the two algorithms in experimental applications is more subtle than this and not particularly well understood.

1.7 Fitness Parameters

This section describes a couple of useful parameters that can help determine when the phase retrieval algorithms previously described have reached a good fit to the data. These parameters are: The g and the Fourier-space error.

1.7.1 Real-space Error

The real-space error [42] gives a very good handle on how stable a given reconstruction is. The idea is that by taking the difference between the current iterate ($x_n(x, y)$) and previous iterate ($x_{n-1}(x, y)$) in a convergence path, and summing the array over all its spatial elements (x, y)(as per equation 1.67), any variances in these iterates can be found, and hence a final fit value determined.

$$rE_n = \sum_{\text{All x,y}} x_n(x, y) - x_{n-1}(x, y) \quad (1.67)$$

It can be noted that this parameter with the summation removed is actually the same as the difference term noted in the difference-map methods for phase retrieval (sections 1.5.6 and 1.6.1).

Whilst this measure is useful for measuring the convergence of ptychographic object reconstructions, it is not necessarily useful for monitoring the progress of CDI algorithms. This is due to the ambiguities inherent in far-field CDI reconstructions. Since only the magnitudes of the angular spectrum are measured, real-space reconstructions can be subjected to both arbitrary phase offsets and ramps, both which can make the real-space error unreliable for CDI reconstructions.

1.7.2 Fourier space error

The Fourier-space error [45] is another useful fitness parameter, which quantifies how close the current iterates Fourier transform ($\tilde{x_n}(\mathbf{k_x}, \mathbf{k_y})$) fits the input data ($I_{meas}(\mathbf{k_x}, \mathbf{k_y})$) as a whole. It is characterised by a cost function(1.7.2).

$$fE_n = \frac{\sum\limits_{\text{All } \mathbf{kx},\mathbf{ky}} (\tilde{x_n}(\mathbf{k_x}, \mathbf{k_y}) - \sqrt{I_{meas}(\mathbf{k_x}, \mathbf{k_y})})}{\sum\limits_{\text{All } \mathbf{kx},\mathbf{ky}} I_{meas}(\mathbf{k_x}, \mathbf{k_y})} \tag{1.68}$$

1.8 Resolution

It is apparent to any student of microscopy that there are a broad range of definitions of what constitutes the smallest resolvable feature in a microscope system. Indeed, usually the most useful criterion to know is actually the response of the system over all resolution components, characterised by a transfer function. This section describes three such functions: The crystallographers' R^2(section 1.8.1), the phase retrieval transfer function (PRTF)(section 1.8.1), and the Fourier ring correlation (FRC) (section 1.8.1).

However, when comparing microscopy systems it is also useful to be able to reduce this transfer function down to single figure of merit and compare this to the best that could be hoped to be achieved according to certain theoretical criteria. The criteria considered in the following sections are the Rayleigh criterion (section 1.8.2) and the Sparrow criterion (section 1.8.2).

1.8.1 Transfer functions

When comparing microscopy systems based on similar technologies, it is very useful to consider the response and stability of the microscope system for all resolution components. In the CDI case this information is dominated by the computational element. This is information that can be readily characterised by the various transfer functions that are described in this section.

The crystallographers' R^2 measure

For a single reconstructed wave-field, it is useful to use the crystallographer's R^2 parameter [60] defined by equation 1.69 to judge how accurately the reconstructed far-field magnitudes $\tilde{x}_{final}(\mathbf{q})$ match the recorded data $I_{meas}((q))$ for each spatial frequency $\mathbf{q}$.

$$R^2(\mathbf{q_i}) = \sum_{\mathbf{q_i}} \frac{\tilde{x}_{final}((q))}{I_{meas}((q))} \tag{1.69}$$

This is a useful data fitness parameter, but doesn't show how robust the given solution is. It may be that perhaps that a given feature only reconstructed once, and that is what is being quoted here.

The phase retrieval transfer function

To give a better judge of how reliable the resolution is for a given resolution element $\mathbf{q}$, it is more useful to run the same reconstruction many times ($>$ 100) and to look at the far-field phase $\psi(\mathbf{q}$ error over all of these for each spatial frequency when the trivial shift and absolute phase ambiguities have been removed. This corresponds to the phase retrieval transfer function (PRTF) [61].

$$\begin{aligned} PRTF(\mathbf{q}) &= |\langle \exp[i\psi(\mathbf{q}]\rangle| \\ &= |\langle \frac{\tilde{x}_{final}(\mathbf{q})}{|\tilde{x}_{final}(\mathbf{q}|)}\rangle| \end{aligned} \tag{1.70}$$

It is suggested that a resolution cut-off can then be taken to be measured when the PRTF drops to 0.5 [43]. Whilst useful for quoting a single figure of merit, as mentioned above, the real power of the PRTF is that it tells how the entire spatial frequency spectrum is transferred through the system, and so it is this entire plot that is interesting. Also, if the EWF under investigation has no features at a given spatial frequency, the PRTF may drop at these points due to the detector noise, which clearly is not a real result.

In some journal articles some researchers have found it useful to instead use the Weiner filtered version of the PRTF (wPRTF) [62], in order to get a smoother roll off at the higher resolution data as the signal to noise ratio gets worse. This helps to get a better 50% cut-off to give a single number for the resolution. However, as previously iterated: this is not what the PRTF is for. For this reason the wPRTF is not used in this thesis and instead the full PRTF curve will be shown and quoted along with the Sparrow criterion.

Fourier ring correlation

For ptychographic datasets, the PRTF is still a nice way of measuring the reliability of the reconstruction for a single view. However, when data for large numbers of views (> 100) are collected, it makes calculation, let alone interpretation, of these curves infeasible. For this reason it is useful to look at other, more developed areas of research to find a suitable figure of merit.

In macromolecular crystallography and 3D cryo-electron microscopy (cryo-EM), a standard measure of the reliability of data has been decided upon, namely Fourier shell correlation [63]. This measure involves finding the cross correlation of two data-sets of the same object as a function of recorded spatial frequency. For the lower dimensional data of 2D ptychography one can consider the similar process of Fourier ring correlation (FRC) [63] defined by equation 1.71 for radial (r) distributions F_1 and F_2.

$$FRC(r_i) = \frac{\sum_{allr_i} F_1(r) F_2^*(r)}{\sum_{allr_i} |F_1(r)|^2 \sum_{allr_i} |F_2(r)|^2} \tag{1.71}$$

This curve will have a magnitude of 1 for resolution features that are correlated perfectly between the two reconstructed images, and a value of 0 for features that are completely uncorrelated.

For both FSC and FRC, there is still the urge for researchers to quote a single number for the resolution, mostly for publication reasons. In [64], the authors argue that the best criteria one can suggest for the resolution cut-off is when the signal of this correlation disappears into the noise, i.e. when the signal to noise ratio = 1. In cryo-EM applications, the data recorded is usually redundant enough that reconstructions from a data set can be divided into two and compared to each other. For this reason the "half-bit" criterion was decided upon for the figure of merit, representing the point where the signal to noise ratio for each half data-set is 0.5 - the total dataset hence having a ratio of 1. However, for the ptychographic case, where the same probe function can be used across multiple objects of interests, we can take the FRC of the probe functions across full data-sets, keeping the cut-off at a

signal to noise ratio of 1. Even better than this would be taking the FRC of two independant object functions, if they are available.

For the work in this thesis, the full FRC curve will be shown for each ptychographic dataset presented along with the 1-bit cut-off.

1.8.2 Resolution by comparison to figures of merit

For comparison of results across different microscopic techniques, it is usually move preferable to obtain a single value for the resolution of an imaging system. Practically, this can be achieved by comparing the smallest resolvable feature to the theoretical limit of the capability of the microscope. In this sub-section, two of the most popular theoretical formulations for a microscope are discussed.

The Rayleigh/Abbe/Helmholtz diffraction limit

The most commonly used theoretical limit for a microscope is that set out by Abbe [8] and Helmholtz [9], building on work done by Rayleigh [10]. This limit is expressed mathematically for a circular objective by equation 1.72 for a wavelength λ and objective with a numerical aperture NA imaging a feature size δd.

$$\delta d = \frac{1.22\lambda}{NA} \tag{1.72}$$

Physically, this factor of 1.22 comes from the fact that the smallest object imaged by a circular lens will be a Bessel function. The smallest resolvable feature according to this criterion is when the peak of one Bessel function overlaps with the null point of a second one. This is shown graphically in figure 1.19.

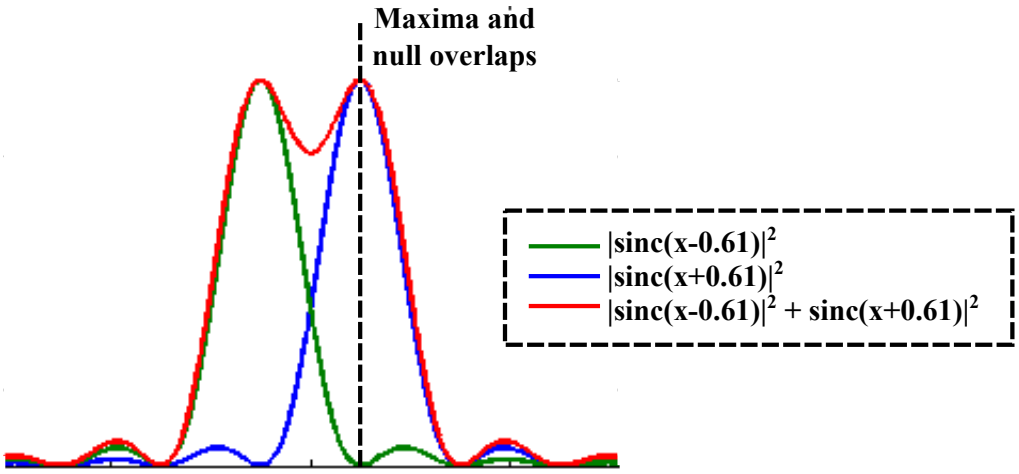

Figure 1.19: The Rayleigh diffraction limit. When two 1D Bessel functions are closer than 1.22 radians, they cannot be distinguished from each other since the null of one functions is masked by the maxima of the other.

At separations less than this distance, it is argued that the two shapes cannot be distinguished from each other since the signal does not drop down close enough to zero between the two features.

The Sparrow Criterion

The Sparrow criterion is another diffraction limit measurement commonly used for astronomical purposes, but provides a different take on the limit of resolution. The method was initially developed by C.Sparrow [65] for the spectrographic case and is more useful than the Rayleigh criterion since it can be adapted to measurements with a discrete grid.

As with the Rayleigh diffraction limit the case considers two point sources, represented by their respective Bessel functions for a circular objective aperture. Instead of the dip in the measured intensity signal as seen in Rayleigh limit, the Sparrow criterion instead considers the two objects unresolvable when the gradient of the incoherent sum between the two sources goes to zero. This is most useful for the discrete case considered here in this thesis since we can no longer distinguish between two points when their separation is less than two pixels on the discrete grid. At this stage the features are unrecognisable from each other. Again, this can be shown graphically as in

figure 1.20.

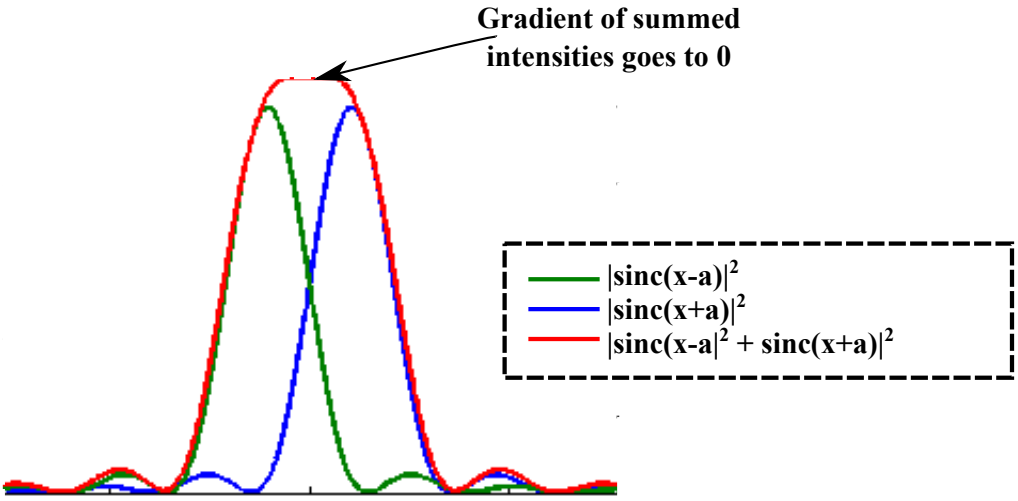

Figure 1.20: The Sparrow diffraction limit. When two 1D Bessel functions are close enough that the gradient of their incoherent sum is 0, they cannot be distinguished from each other.

1.9 Summary

This chapter has outlined the background and concepts for the work presented in this thesis. The general scope of how HHG CDI/iterative ptychography fits into general microscopy techniques was discussed and comparisons to other techniques were drawn.

The physics of the HHG process were introduced and their application and optimisation for the work presented in this thesis were discussed, along with details of the equipment required to generate such radiation in a laboratory environment.

Lastly, the algorithms used for phase retrieval were outlined and some simple examples of their behaviour were discussed for both CDI and iterative ptychography. Some parameters for monitoring the goodness of the fit during the algorithms progression were outlined. An overview of how to quantify and characterise the resolution of the resultant CDI/iterative ptychography images were put forward and clarified.

Chapter 2

Coherence in CDI

This chapter introduces ideas of how partial temporal coherence can be treated in the CDI process to reduce integration time and radiation damage. In comparison to work by other groups using a modified algorithm [66, 67], the limitations of the fully coherent CDI routines are investigated and a result showing a reasonable reconstruction using 20% bandwidth is presented. This work has been in the Institute of Physics Journal of Optics [68] and has been presented at multiple international conferences [69, 70].

2.1 Background

Since scattering by an aperiodic sample results in reduced signal to noise compared to by a crystal, it is essential in CDI to use as much of the probe flux as possible, which can require a compromise on the beam coherence properties.

A single exposure technique termed 'polyCDI' [66, 67], allows the use of broadband polychromatic radiation, alleviating the limitation on flux imposed by the need to monochromatize the X-ray beam; a technique complemented by [71] for spatial coherence. The concept of these algorithms is that if the EWF for each of the temporal/spatial modes have similar speckle patterns - i.e. the illumination wavelengths are away from absorption edges - then this provides an additional constraint in the fit to the recorded speckle pattern, allowing the spectrum to be recovered.

The limitation that the sample be non-dispersive does not limit the usefulness of the technique since the region of interest may be buried beneath a layer of material opaque to other forms of radiation, but transmitting and non-dispersive in the EUV or soft X-ray. An example of such an object is shown for clarity in figure 2.1 below.

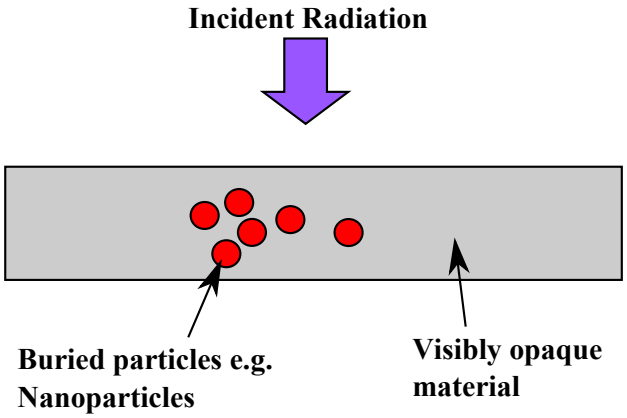

Figure 2.1: An example of a buried sample that could not be imaged via electron or optical imaging. Broadband X-ray CDI could recover the structures of such buried objects.

However, polyCDI algorithms generally require a good initial starting support of the object in order to break the ambiguity between spectral and spatial contributions to the scattering angle. A support for buried samples would be hard, if not impossible to determine. An alternative broadband technique is available for pulsed sources [72, 73], which modulates the spectrum via spectral interference from identical, but delayed-scanned probe pulses. However, such techniques have yet to be proven in the lower signal-to-noise, and higher resolution, far-field regime.

2.2 Theory

To fully understand and characterise the temporal coherence of any system it is necessary to find the complex mutual coherence function (see section 1.9). This provides a measure of how well the wave form correlates with itself over a large distance, and can be parameterised by a temporal coherence length l_c representing the half width at half maximum (HWHM) of the mutual coherence function. This definition is good for accelerator based sources of short-wavelength radiation where the coherence length is dependant on the relativistic length of the insertion device used to generate the radiation.

For most laser based sources however, the mutual coherence function can be quasi-infinite, so the effective coherence length is instead determined by the experimental requirements. In EUV CDI experiments, the beat period between the difference frequency components if much shorter than the measurement time (>1s), so an incoherent sum $|U_{tot}(x, y, z')|^2$ of the absolute

magnitudes of the wavelength-scaled far-field scatter patterns $U(x, y, z'(\lambda))$ is measured as denoted by equation 2.1 for a resultant field

$$|U_{tot}(x, y, z')|^2 = \sum_{all\lambda} |U_{tot}(x, y, z'(\lambda)|^2 \tag{2.1}$$

This results in a reduction of the fringe visibility V of the scattering peaks, defined by equation 2.2.

$$V = \frac{I_{max} - I_{min}}{I_{max} + I_{min}} \tag{2.2}$$

Spence et al. [74], propose a limit on the maximum energy spread $\frac{E}{\delta E}$ allowed for a CDI experiment to still appropriately sample (see section 1.5.2), and reliably retrieve the phase of the scattered far-field magnitudes and not be affected by reduced fringe visibility. This limit is expressed in equation 2 for an object of width W imaged with resolution defined by a spatial half-period d and represents the sampling of the non-zero density in sample space.

$$\frac{E}{\delta E} > \frac{W}{d} \tag{2.3}$$

This definition assumes the sampled spectral envelope is smooth and does not take into account any sub-structure of the spectrum such as that which is generated during the non-linear optical process of HHG. The HHG process produces a train of fully spatially and temporally coherent EUV pulses (see section 1.2), which in the spectral domain provides a harmonic comb down to a cut-off frequency. In far-field CDI imaging of non-dispersive objects, the scattered signal from each of the harmonics will be similar, with a wavelength scaled scattering angle.

The impact on fringe visibility of the incoherent sum of scattered signals for a theoretical source with finite bandwidth is illustrated in figure 1 where an incoherent sum of analytically derived Young's slits experiment is plotted for two different spectra. Figure 2.2a) shows simulated spectra of the sources, one broadband, and one harmonic with similar envelope. Figure 2.2b) and c) show the fringe patterns from a simulated Young's slits experiment illuminated with the two sources shown in a), with a slit width and separation of 1 micron. Fringes from the harmonic source, c) retain visibility at high spatial frequencies, unlike the envelope case b). Since the scatter patterns from different spectral components from a non-dispersive objects are the same, simply scaled by wavelength, the improvement in visibility is attributed to overlapping speckles from different spectral components. In the envelope case, the speckle minima are washed out by the other spectral components.

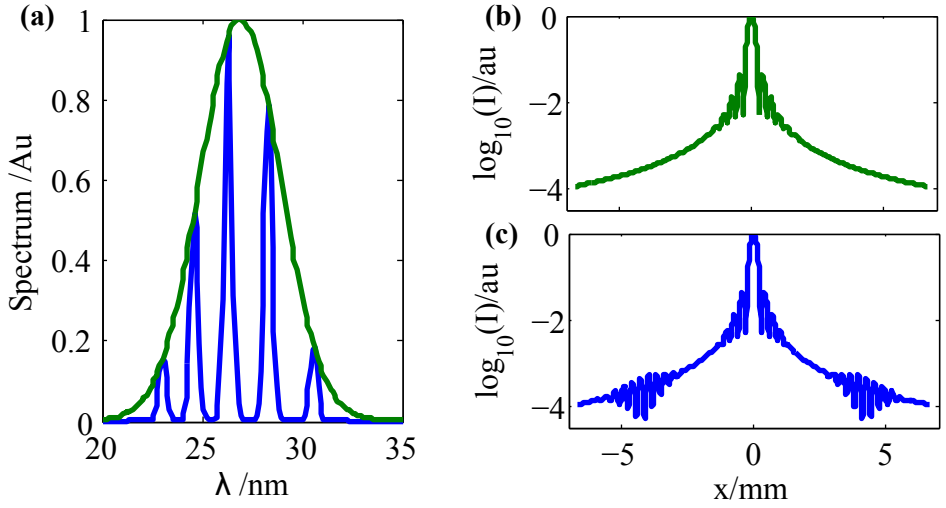

Figure 2.2: a) A simulated 20% bandwidth spectral envelope (green line) and a modulated, harmonic, spectrum with the same bandwidth (blue line). A simulated 1 μm separated Young's slits experiment for the envelope b) and the harmonic c) spectra in the same geometry as the experiments in this chapter. The plots represent an incoherent sum of an analytic Young's slits scatter pattern

Previously on synchrotron based CDI experiments it has been shown that standard CDI reconstructions fail completely when a bandwidth of greater than 1 % is used [67].

In the following experiment and analysis, by comparing speckle patterns collected from the same sample illuminated via broadband and narrowband illumination the required integration time for experiments is reduced and further understanding of how partial coherence is treated through the CDI process is obtained.

2.3 Experiment

The experimental set-up for the experiments detailed in this chapter are shown in figure 2.3. A 50% pick-off of the Spectra Physics laser system described in section 1.2.2 is focussed using a 50 cm spherical dielectric mirror into a gas cell containing 80 mbar Argon gas to generate the high harmonic radiation. The EUV imaging chamber is held at a 10^{-6} mbar high vacuum to increase transmission along the optical path. Two sets of Al free-standing thin film filters (Lebow) are used in the beam path to separate the infrared (IR) beam from the generated EUV. These filters are each composed of two

100 nm films layered together to avoid the pinhole effects induced by oxide window formation [75, 76, 77]. The experiments detailed in this paper can be classified into two separate experimental configurations: narrow-bandwidth (NB, figure 2.3 a)) and broad-bandwidth (BB, figure 2.3b)).

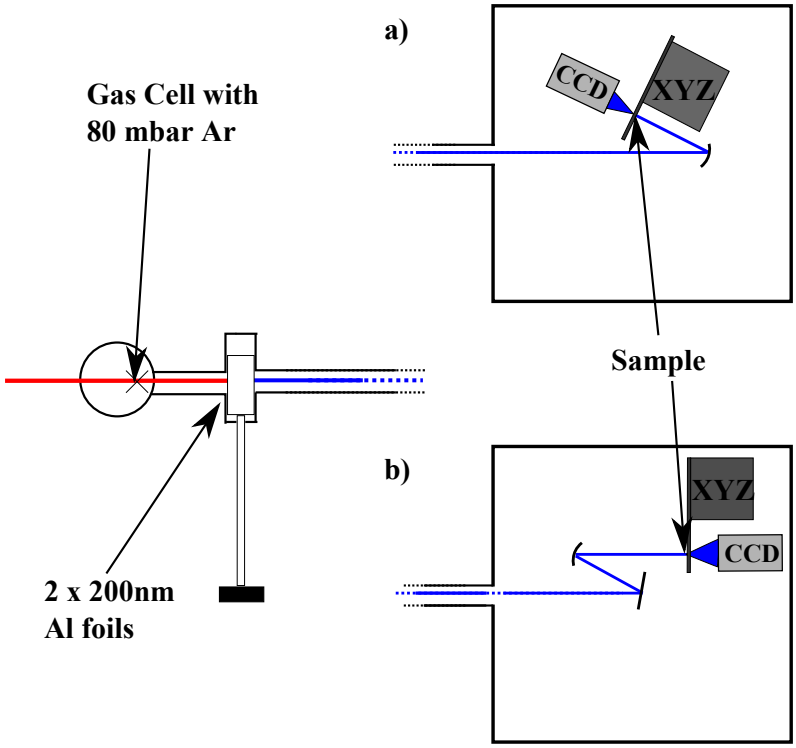

Figure 2.3: The two experimental geometries used for this experiment. The pump infrared is focused into a gas cell containing 80 mbar Argon to generate the high harmonics. The pump is then filtered from the generated harmonics by free-standing Al foils. a) The experiment for the broadband geometry. The light is focussed off a single 50 cm spherical multilayer mirror. b) The narrowband experiment. Before being condensed by the same spherical mirror, the light is incident first on a flat multilayer mirror. The reflectivity curves of these mirrors overlap so as to isolate a single harmonic.

For BB experiments, the EUV transmitted through the filters is further spectrally filtered by a spherical Mo/Si multilayer coated focussing mirror with 50 cm radius of curvature, giving a spectrum with a relative envelope bandwidth of 20% (figure 2.4a)) incident on the sample. In the NB experiment the EUV spectrum was filtered further (figure 2.4b)) by a flat Mo/Si multilayer mirror fabricated by Sasa Bajt from the X-ray optics group at DESY. The reflectivity curve of this mirror overlaps with that of the focussing

mirror, isolating a single harmonic with bandwidth 0.7%. This monochromatic optic reduces the total flux by 80%.

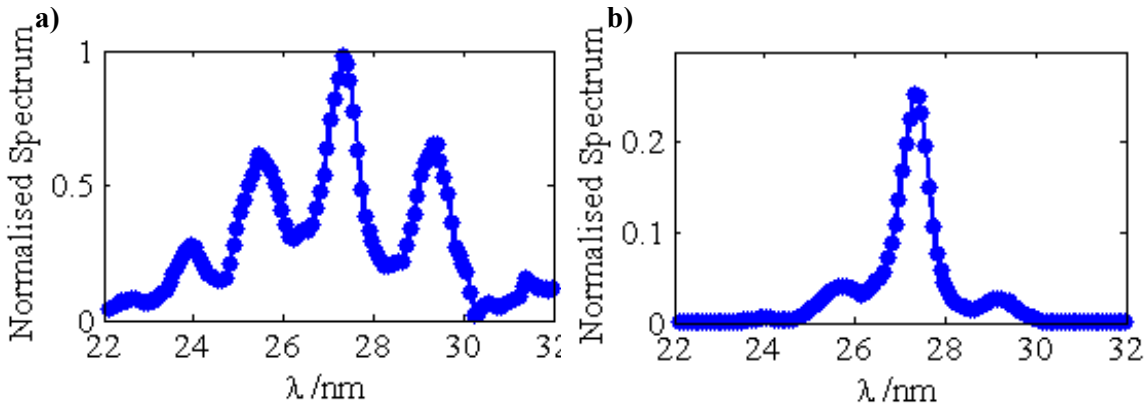

Figure 2.4: The two different spectra used to illuminate the sample.a) Broadband: The beam filtered only by the condensing multilayer has a bandwidth of $\tilde{2}0\%$ but has a harmonic structure to it. b) Narrowband: A single, dominant, harmonic is isolated by also filtering using the flat multilayer.

The sample for these experiments was an amplitude mask manufactured in collaboration with the University of Southampton Electronics and Computer Science (ECS) Nanofabrication department. A scanning electron micrograph of this sample is shown in figure 2.5a). A 50 nm thick low stress silicon nitride (non-stoichiometric, low-stress, SiN, Silson Ltd) membrane was coated by the author with a 95 nm thin film of Au deposited via electron beam evaporation. A 5 nm layer of Cr was deposited first onto the SiN to improve the adhesion of the film. A structure, a pictoral representation of a methanol molecule, was milled through all of these layers using a focussed beam of gallium ions (FIB) by Stuart Boden (ECS). A schematic of the cross-section of this sample is shown in 2.5b). The extremely low transmission coefficient ($< 10^{-4}$ at 27 nm [78]) of the combined deposited material compared to the complete transmission of the milled hole validates the non-dispersive scattering approximation. Some key dimensions of features include its 2-dimensional full extent of 2.5 μm x 2 μm. The 'arms' of the object are 200 nm across and the circular tips are 300 nm in diameter. The diamond shape in the centre of the sample has a width of 400 nm.

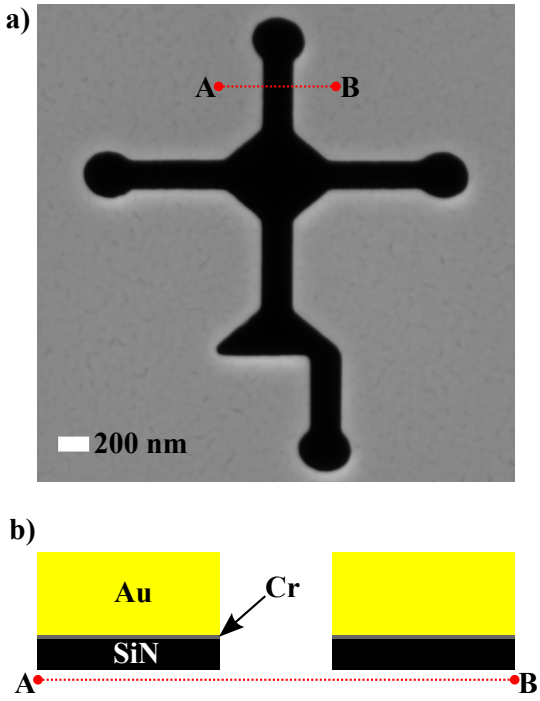

Figure 2.5: The sample used for these experiments. a) A SEM of the sample. b) a schematic cross section through the red line in a) showing the composition of the sample. The high attenuation of the sample coating compared with the FIB milled hole gives this sample binary transmission characteristics.

In the CDI experiment the scattered photons were collected on a 1024 x 1024 X-ray charge-coupled device (CCD, Andor DV434) with 13 μm pixels. For these experiments the sample to CCD distance is fixed at 15 mm, which, for 27 nm radiation gives a diffraction-limited resolution by the Sparrow approximation (section 1.8.2 of 61nm with numerical aperture (NA) of 0.22. This means that the $\frac{W}{d}$ value defined in equation 2.3 can be calculated for this experiment to be 42. For the NB experiment $\frac{E}{\delta E} = 153$, which easily fulfils the limits in equation 2.3. It follows that the effective coherence length for the NB experiments is 5 μm, fulfilling the standard imaging criterion that the coherence length be larger than the sample. For the BB experiment $\frac{E}{\delta E} =$ 5 and the effective coherence length is 135 nm putting the experiment firmly into the regime where the image quality should be affected by incoherence.

Data collected for the NB experiment was integrated over a single 220s exposure. Due to the overlapping and summed DC Fourier components from the different harmonic components, data for the BB experiment was summed over 5 x 45s exposures to increase dynamic range giving a total integration

time of 225s, approximately the same as for the NB dataset.

Both data sets were centred, background subtracted and any cosmic rays/hot pixels removed by rejection of any pixels outside a 3σ range. The data were then projected to the Ewald sphere of the central scattering wavelength by cubic spline interpolation. To improve the accuracy of this interpolation the data was first smoothed by zero-padding the Fourier transform of the signal by a factor of 5 for this process. The signal was then down-sampled similarly afterwards.

2.4 Data analysis

The upper left quadrant of the signal on the CCD for BB and NB data sets collected during the experiments are presented in figure 2.6. It is immediately clear from the expanded views and line plots, the impact that the broad bandwidth has on the reduction of the visibility of the recorded scatter pattern. By comparing the DC peaks of both datasets we can deduce that by using a beam block in this experiment, to increase the dynamic range of the detector, the integration time could be reduced by a factor of 5.

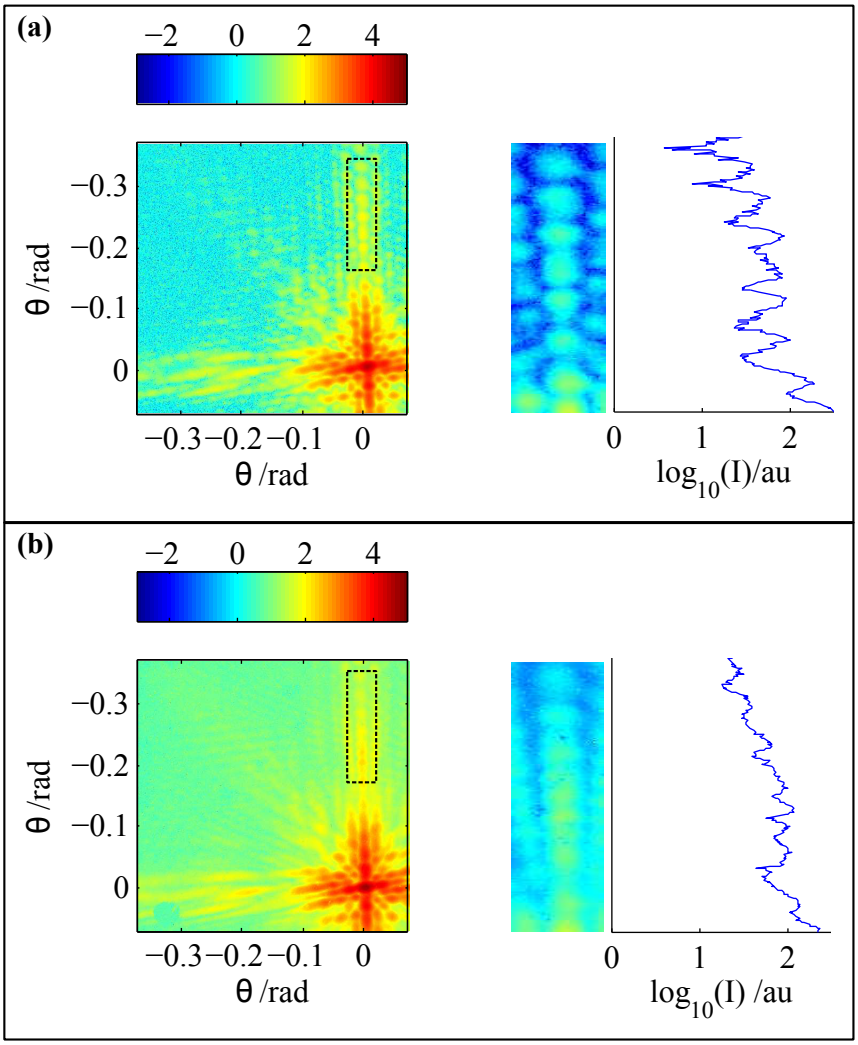

Figure 2.6: Comparison of the speckle pattern for a) the narrowband and b) the broadband illuminations.a)Narrowband: The speckles in the narrowband image are quite sharp and easily resolved. This is particularly clear in the close up of the area inside the dotted box, shown in the inset with a cross section though its central region.b)Broadband: This image is of the same portion of the speckle pattern as shown in a) but under broadband illumination. One can see from the inset image of the area enclosed within the dotted box that the speckles indeed have lower visibility as expected.

By taking the inverse Fourier transform of the speckle patterns, the autocorrelations of the sample are obtained (see section 1.3.3).The logarithm of the magnitudes of the autocorrelations are shown in 2.7a) left (broadband) and right (narrowband). By summing in the vertical axis (2.7b)) it is clear

to see that the narrow bandwidth data has a factor of 20 greater range in magnitude in its autocorrelation than the broad bandwidth data. The main broad peak in the centre however, looks very similar in both cases suggesting that this information is the same between the two datasets.

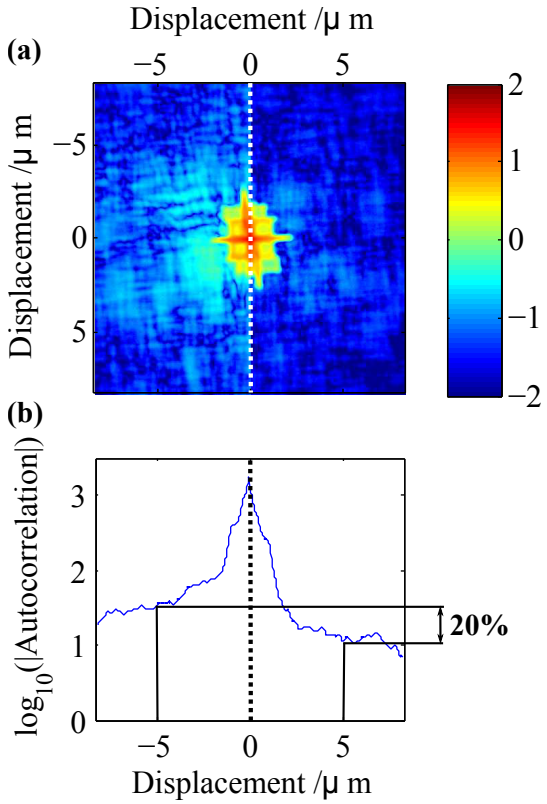

Figure 2.7: A comparison of the two-dimensional autocorrelations of the real-space magnitudes.a)A $\log_{10}$ plot of the autocorrelations for broadband (left) and narrowband (right) data sets. The white line separates the data sets. It can be seen that the broadband set has a considerable amount of structure outside the main density of its autocorrelation in comparison to the narrowband autocorrelation.b) A vertical sum of a), emphasising the difference in densities outside the main body of the autocorrelations between the narrow and broadband data.

In the case of data with zero noise it would be possible to obtain a poorly resolved version of the mutual coherence function by taking the ratio of these datasets. However, for real data this is hard to implement and does not aid recovery of the object by a single illumination - the focus of this work - so instead we apply techniques to remove those areas that are different between the two results.

2.5 Comparison of phase retrieval results- Narrowband vs. Broadband Illumination

Figure 2.9 shows a comparison of the phase retrieval results for the NB and BB experiments. For the NB reconstructions, a standard recipe of 5000 iterations Hybrid input/output (HIO) with β= 0.9, shrinkwrapping every 50 iterations followed by 5000 iterations with no shrinkwrap and β=1 was implemented. The solution to the phase retrieval is determined when the real-space error (see section 1.7.1) varied below a 10^{-7} threshold between iterations. For the BB experiments, the routine is run for 1000 iterations of HIO with β=0.9 and shrinkwrap every 20 iterations. The real space projection selected for analysis and further use is that which corresponds to the minimum Fourier error over the 1000 iterations. For this set of reconstructions this happens before 60 iterations of the routine. This corresponds to a nearby local minimum, which, in general, is that which most closely resembles the object.

The shrinkwrap technique explained in section 1.5.7 is similar to applying a variable low pass filter, working to optimise the result so that it matches the scattering intensities, but also reduces the area of the non-zero support to find the best edge. This has the effect of restricting the amount of data outside of the main body of the autocorrelation that is present in the solution. For quasi-monochromatic scattering data, such as that in the NB datasets, this has the effect of increasing the resistance of CDI to noise. In the case of broadband illumination with a spectrum containing significant gaps, not all the speckles will average away, allowing useful information to remain in the pattern, as shown in figure 2.2. The loss of information at points where the speckles average is similar to the effect of a noisy speckle pattern. Rather than apply a fixed low pass filter to restrict this noise however, it is more favourable to use a variable low pass filter to select the parts of the signal that fit the reconstruction best.

A reconstruction that best matches the data under a phase retrieval routine utilising shrinkwrap, will have the lowest Fourier error (see section 1.7.2) and also the smallest mask size. Once the algorithm has reached this reconstruction, it may rapidly diverge since it is not a solution to the phase problem.

The reconstruction algorithms were run 50 times for each data set from a difference quasi-random starting seed. The Fourier-space and real-space error corresponding to the iteration where the final reconstruction was chosen is indicated in figure 2.8. The conjugate (i.e.inverted) object is also a solution to the phase problem, so the solutions were then flipped to the same orientation

and registered using the algorithm described in [79].

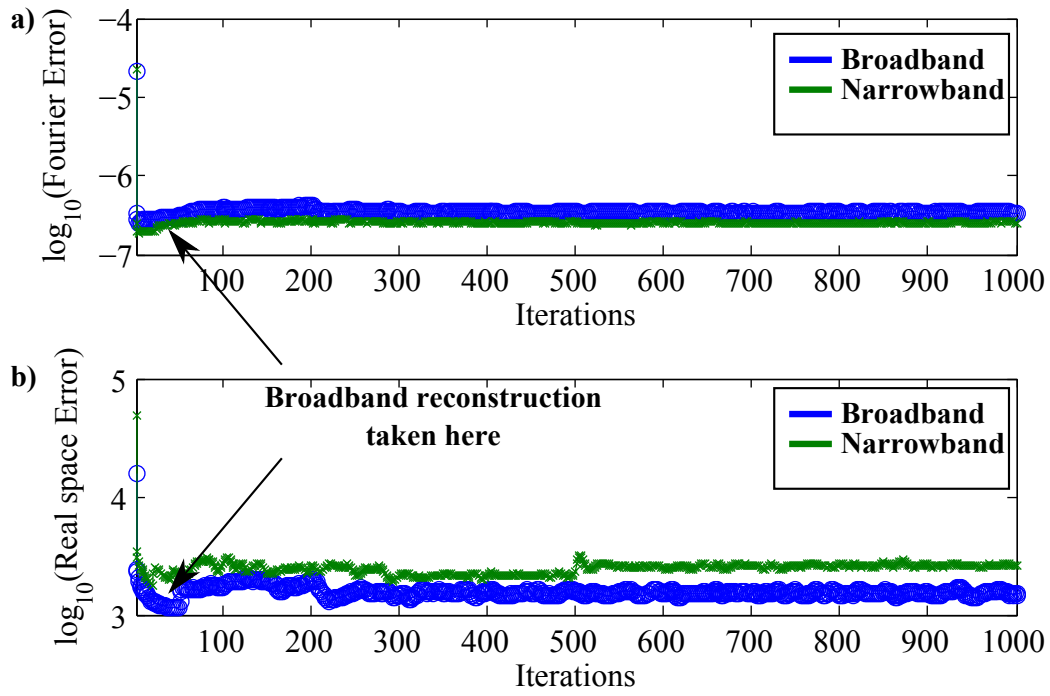

Figure 2.8: The real-space a) and Fourier-space b) errors for the reconstructions. Whilst the narrowband reconstruction was taken at the end of the full number of iterations, the broadband result was taken where the Fourier-space error was minimised. This occurred after 23 iterations of the routine for the error shown.

Figures 2.9a) and 2.9b) show the average and standard deviation of the BB reconstructions in real-space. Figure 2.9c) and 2.9d) show the same information but for the NB data. As expected, the NB data shows excellent stability across the 50 iterations, but, more unexpectedly perhaps, the BB data is surprisingly stable considering it is not a solution. The mean normalised variance is especially low within the main density region.

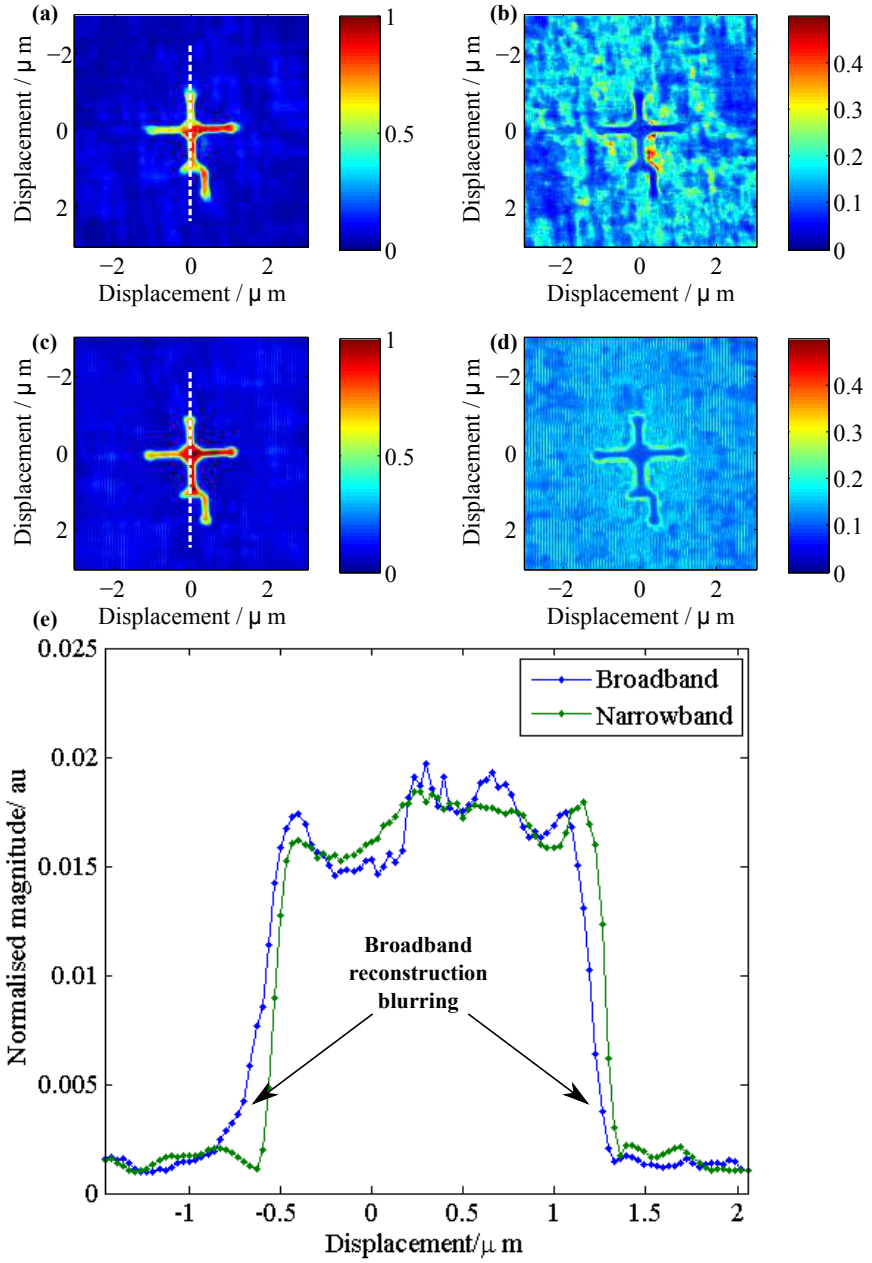

Figure 2.9: The mean of the absolute value of the reconstructed exit wave field from 50 runs of the phase retrieval routine with the same parameters, but different starting phases for (a) broadband and (c) narrowband data. (b) and (d) show their respective mean normalized variances. e) A cross section along the white dashed line of the mean averages in a) and c). It is clear that the broadband data appears blurred compared to the narrowband data.

The key difference between the results to note is a blurring around the edges of the reconstruction in figure 2.9a), much like what would be expected from an aberrated image from a conventional light microscope. This is shown in better detail in the cross section in 2.9e), where the gradient on the rising and falling edges of the signal is much slower for the broadband image than it is for the narrowband image.

The increased variance in the low density region is attributed here to the reduced contrast in the autocorrelations shown in figure 2.7, the main difference between the two data sets. The area outside the main body of the average reconstruction has higher density fluctuations than that in the narrowband reconstruction. This is due to the side-band information visible in the autocorrelation information in figure 2.7. Some parts of the density have been generated by the algorithm to fit the extra data probably because it appears as background noise on a monochromatic signal. This extra density is typically within 0.3σ of the total reconstructed intensity, and could be thresholded if necessary for further use.

To further analyse the impact of the additional bandwidth on the reconstructions, it is useful to look in more depth at each resolution component by way of the PRTF. Figure 2.10 shows the PRTFs for both the BB and NB data taken over the same 50 reconstructions previously described in figure 2.9.

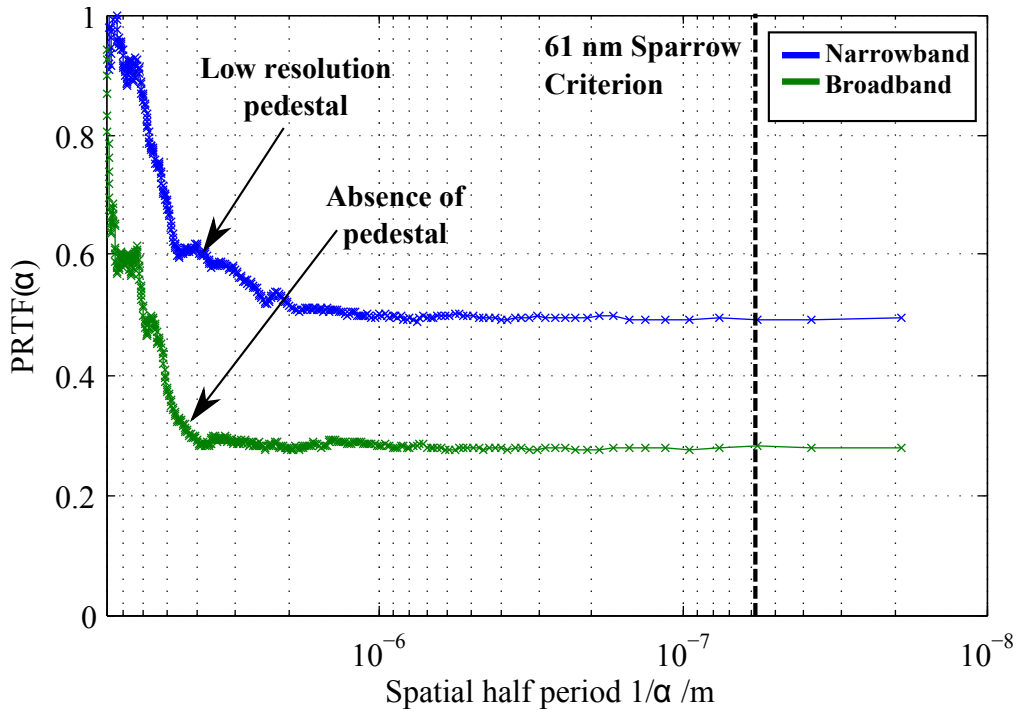

Figure 2.10: The phase retrieval transfer functions for the reconstructed data. The narrowband curve represents the PRTF for 50 separate starting seeds run in the algorithm according to the stated recipe for 1000 iterations. The broadband iterates were selected when the Fourier error was minimised. The data were set to have the same phase offset and centred by image registration before the PRTFs were calculated.

This shows that at high spatial resolution, the transfer function follows the same curve, although the information is less reliably reconstructed for the broadband illumination resulting in a lower value for the PRTF.

At low resolution the PRTF for the broadband data shows the absence of a pedestal for 2-4 μm resolution data, the same resolution information that appears blurred in figure 2.9a). This suggests that the blurring seen in the average is a manifestation of poor reconstruction stability for these spatial frequencies, a similar result noticed as in the case for poor signal to noise ratio data. This is a similar and related result to that obtained earlier in the simulation of Young's slits. For some spatial frequencies, there is just enough information due to the increase in visibility of the speckle pattern, to reconstruct. For others however this is not the case and that resolution component is lost.

In comparison to previous research using the polyCDI algorithm on high harmonic sources, the reconstructions shown here are of similar quality al-

though they were achieved without prior knowledge of the spectrum being required. Since the spectral components are not separated, the phase of the reconstruction in figure 2.9a) does not have a physical meaning [35] and hence this reconstruction is not a solution to the phase problem, unlike that shown in [67, 66]. Instead, these reconstructions should be considered as an approximation to the solution, albeit a very good approximation.

2.6 Summary

In conclusion, it has been demonstrated that it is possible to use monochromatic phase retrieval techniques on ultra-broadband scatter patterns to obtain a good first approximation to the object amplitude reconstruction using CDI. Whilst such broadband reconstructions are generally not stable, it is believed that this will increase the stability and noise tolerance of algorithms such as the polyCDI algorithm [67, 66], and also provide new routes to full solutions in these cases. The technique could be applied to radiation from other sources as long as the spectrum is filtered or scanned to increase the visibility of speckles at the required spatial frequencies. This work provides a way to dramatically reduce limitations on flux requirements imposed by spectral filtering on both large scale and lab-based sources of EUV and soft X-ray radiation by increasing the tolerated bandwidth to 20 %.

Chapter 3

Iterative Ptychography experiments

This chapter presents preliminary results implementing iterative ptychography using a HHG source. To provide some context, and to gain experience with real data, I participated in an experiment as part of Ian Robinsons group at University College London (UCL). The work in section 3.1 is presented with their permission. Results imaging a test sample at the I13 beamline are presented and contrasted to those achieved on the HHG source at Southampton.

The work at Southampton, detailed in section 3.2, is the first reported iterative ptychography experiment using a laboratory-based source in the world. This work also documents the first imaging of a biological sample from a laboratory-based source of EUV.

3.1 Ptychography at Diamond light source I13 beamline

To gain some experience implementing ptychography using real data, I participated in a beamtime with Ian Robinsons group (UCL). The results presented in this section were taken with Joerg Schwenke and Laura Shemilt from this group. The I13 beamline produces a spatially and temporally coherent beam, specifically targeted at implementing CDI and iterative ptychography technologies. It is hoped that by comparing the results between this and the HHG source at Southampton more can be understood about how the ptychographic process deals with noise, beam drift and other experimentally important factors.

3.1.1 Experiment

Figure 3.1 shows the beamline set-up for this experiment. After the X-rays are generated via the relativistic electron interaction with an undulator insertion device (ID), they are focussed by way of a compound refractive lens (CRL), situated near the source, 250 m away. Due to the difference in divergence of the X-ray beam in the horizontal and vertical axis, the focus produced in the sample plane is astigmatic. For this reason, guard slits 4 cm before the sample are used to shape the beam to an even spot with size $w_0 = 15$ x 10^{-6}. Since at Diamond the electron beam is very small and a the I13 beamline very long, the spatial coherence is very high >100 μm. The beam is then monochromated by way of a double pass single silicon crystal monochromator, aligned in single circle mode, giving a final bandwidth $\frac{E}{\delta E} = 10^4$ at 7.5 keV $\pm$ 25 eV. The error in energy here comes from phase error in the ID over its 50 period magnetic array; the monochromator is tuned to the peak of the relativistic cone [80].

The light then propagates in vacuum until it is spatially defined with a final pair of slits. The light is then incident on the sample, propagating through another 14.5 m section of vacuum until it is recorded on the detector. The detector for this experiment was a Quad Maxipix CMOS photon counter, using Medipix2 chips made up of 4 panels of 256 x 256 pixels. The signal is centred on one of the panels of this detector providing an NA of 2.43 x 10^{-4} fulfilling the small angle approximation, so no further projection to the Ewald sphere is necessary. The 1D oversampling ratio for this experiment is 2.38 which provides 5.26 pixels per scattering peak. The object space pixel size is 87 nm and so by the Sparrow criteria the diffraction limited resolution is 174 nm.

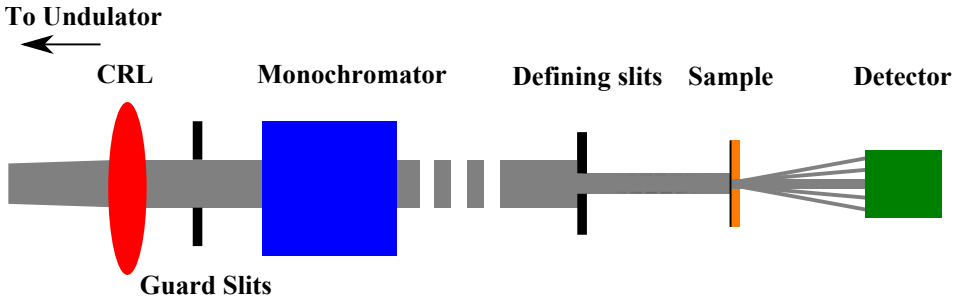

Figure 3.1: A schematic of the experimental layout at I13 for this experiment. The beam comes in from the left and is incident on the detector on the right after passing through the chain of components

The sample for the experiment reported here was a test sample made

of low stress silicon nitride coated with 200 nm tungsten. The pattern was etched into the tungsten using e-beam lithography to reveal the transmitting structures as shown in figure 3.2 a). The large square structure in the middle of the pattern is a phase plate with different thicknesses of material. The star structures are Siemens stars which are commonly used in microscopy to characterise the resolution of a system. Figure 3.2 b) shows a schematic cross section through part of the sample.

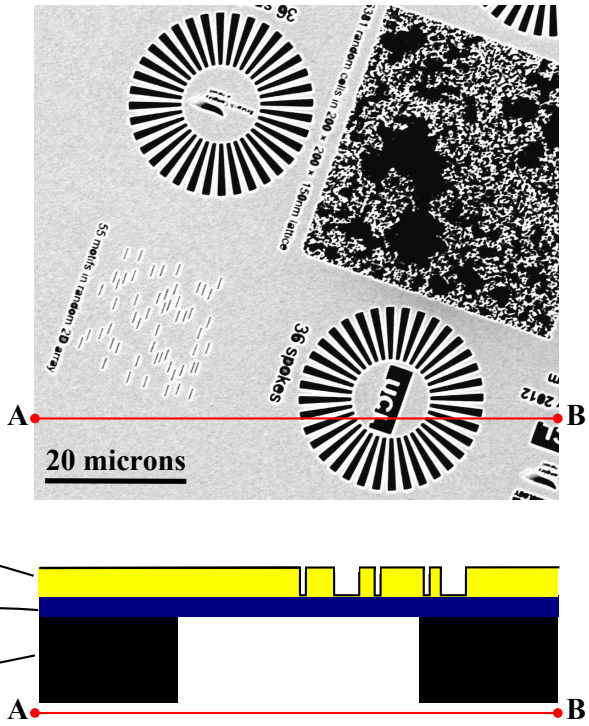

Figure 3.2: Top: An SEM of the resolution test sample designed by the UCL group. Bottom: A schematic of the sample cross section through line AB. The sample is SiN coated with Tungsten. The Tungsten is then removed via e-beam lithography to reveal the structures

The sample was scanned behind the slit defined beam in a round ROI [51] spiral format. The scan positions are shown in figure 3.3 a). At each point an exposure of 10 s was taken. A single shot of the total exposure is shown in figure 3.3 b), with a total of 300 views collected. The centre of the speckle pattern demonstrates some defects due to a tungsten beam stop that was used to increase the dynamic range of the signal that could be recorded at each dwell point. The signal at these points was multiplied by a constant factor calculated by calibration of the beamstop to bring the signal up to the correct value.

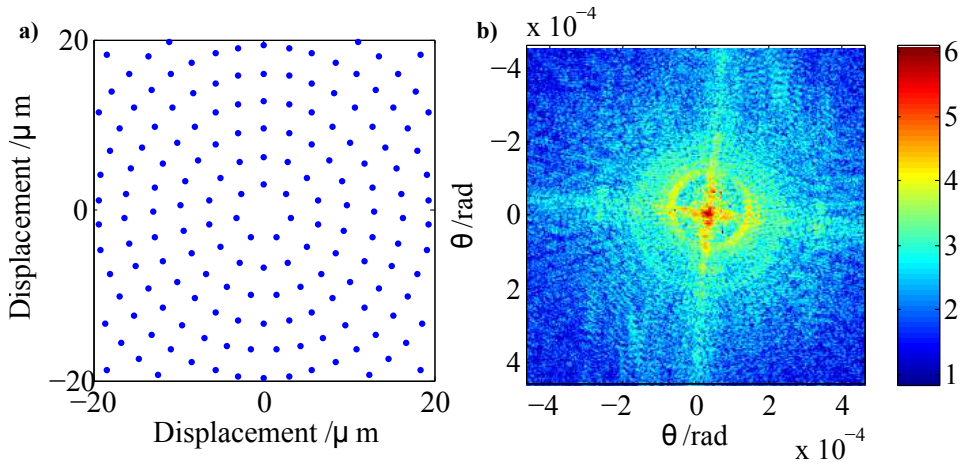

Figure 3.3: a)The round ROI scan position map which was input directly to the piezo motors to perform the ptychographic scan. b) A sample data-set from a single view taken whilst the Siemens star was aligned to the probe

The advantage of collecting such a large amount of data is that it allows some statistical analysis to be applied to the signals. Figure 3.4 shows a plot of $\frac{\sigma}{mean}$ (the mean-normalised variance) for each pixel over the whole 300 views. Analysis of 3.4 allows us to state several things about the data.

Firstly, the data shows a large variation across a broad range of scattering angles, which demonstrates that there is a lot of view dependant signal across the total data set. This is a good first check to tell whether the data is viable for reconstruction via iterative ptychography.

Secondly, there is a lot of information that is relatively independent between views. This data extends out to the very edges of the collected scattering angles, suggesting that the probe is very well defined within the data. This means that a weak guess at the initial probe should be sufficient to reconstruct; a 'model' probe of a top hat function with a radius equal to the half width of the defining slit separation was chosen for this work.

Lastly, it is possible to discern several data points which have either abnormally low or high $\frac{\sigma}{mean}$ values. Those which are very low correspond to either dead or hot pixels on the detector. Those which are high correspond to cosmic ray events which occur for a single exposure. The low $\frac{\sigma}{mean}$ data points are left to "float" in the algorithm and hence are not used to constrain the far-field magnitudes, instead being filled in by the iterative nature of the algorithm. The high variance data points are examined a little more thoroughly, with points along each pixels distribution that fall outside of $\frac{2\sigma}{mean}$ floated only for the views for which they occur, since they have low enough significance to the data to be excluded.

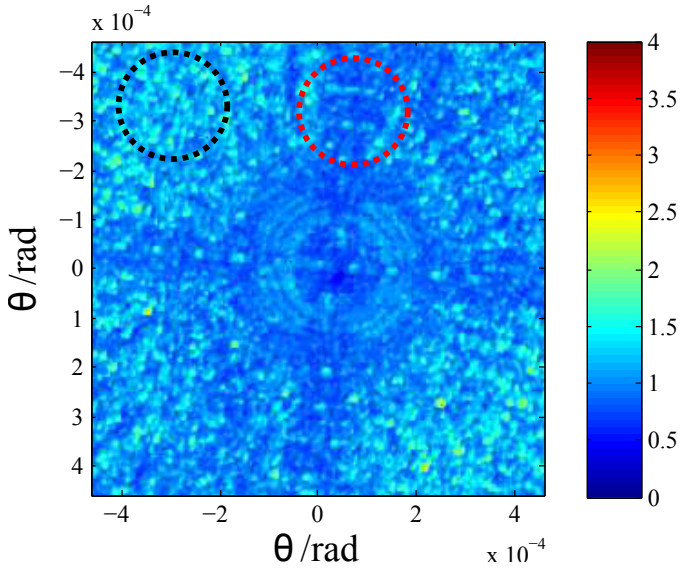

Figure 3.4: A plot of $\frac{\sigma}{mean}$ for each pixel across all recorded views. Areas which have a high value (an example of which is inside the black circle) are those which change between views and can be associated with the object wave-field. Low values (red circle) are independent of the view and so correspond to the probe wave-field

3.1.2 First attempts applying the ePIE algorithm

To begin with, a naïve assumption was made that the experimental data would behave exactly as theoretical data would do, and a basic, unmodified, ePIE algorithm (see section 1.6.2) was applied. A $30\mu m$ diameter circular model probe was used as a starting guess for the first 10 iterations of the algorithm, which was then allowed to update according to equations 1.65 and 1.66 in section 1.6.2 for the remaining 200 iterations. This was tried a number of times from different starting seeds and probe sizes, with the best results shown for the object wave-field shown in figure 3.5a), the probe 3.5b) and the Fourier space error 3.5c) as the algorithm progresses.

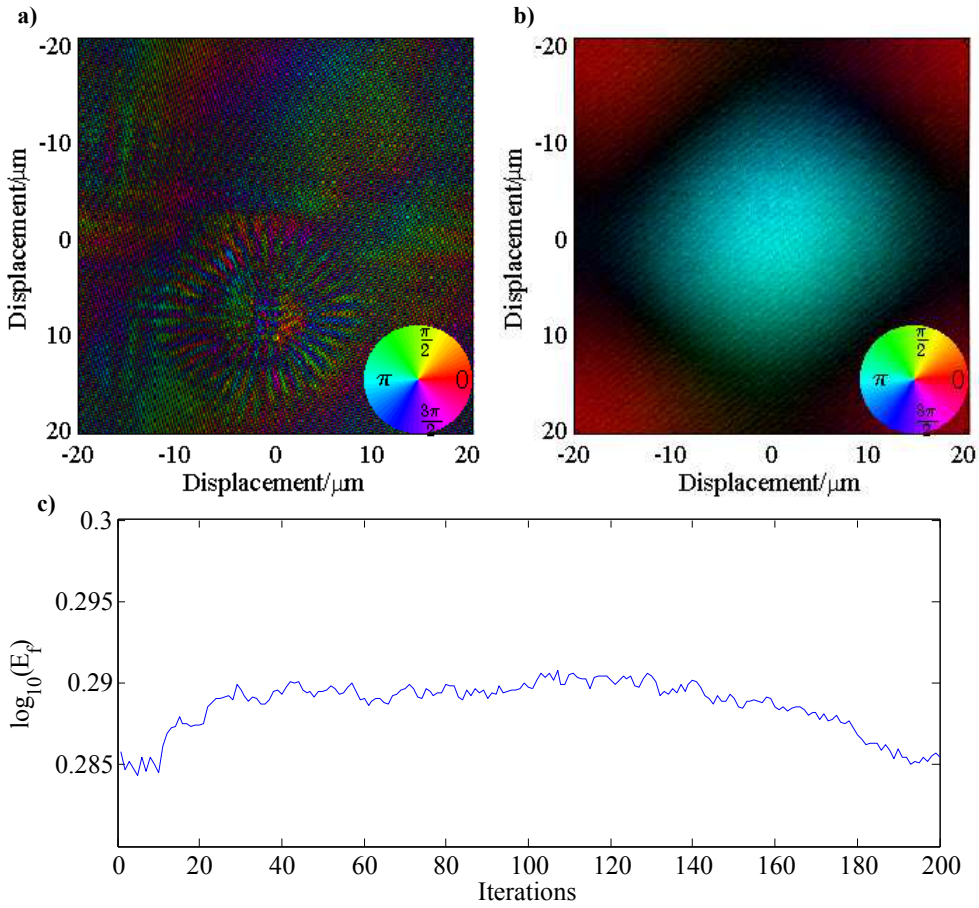

Figure 3.5: The initial results using unmodified ePIE on the collected data. Some structures are visible in the object wave-field a) but further processing is required.b) The reconstructed probe wave-field showing that it has moved out to the edges of the array. c) The Fourier error of the reconstruction as function of iteration, showing that it is not smooth or stable.

Judging by the Fourier error shape in 3.5c), this reconstruction is an unstable fit to the data since after the initial estimate, the residuals from the comparison of the current iterate to the data are increasing. However, it is possible to note some structures in the reconstructed object wave function that look similar to the Siemens star in the test sample (see SEM figure 3.2). This suggests that the algorithm is somewhat close to the correct solution, but needs more care and constraining when applying the ePIE routine. A glance at the probe reconstruction shows that the probe function has spread out into the corners of the array, another good indication that something is wrong with the reconstruction, since we expect it to have some resemblance

to the square aperture provided by the defining slits.

3.1.3 Optimising the reconstruction

To improve upon the previous results, a mask was applied to the probe support. This mask was a circular mask occupying 70% of the total probe space, applied with the aim of constraining the probe to the centre of its support, counteracting the behaviour seen in the previous attempt. Further, another dataset was introduced taken during the same experiment, but of a different region of the sample. The probe function from a reconstruction with one of these data-sets was iterated between both of them in turn as an improved starting guess. This approach was continued until the Fourier error and probe field did not improve significantly with further iterations. A reconstruction showing this applied to the same data as figure 3.5 is shown in figure 3.6a) and 3.6c) and demonstrates a considerable improvement in the reconstructed probe and object phase in comparison to the SEM image. Figures 3.6b) and 3.6d) show the object and probe wave fields for the second data set under investigation and 3.6e) the errors for both sets of reconstructions respectively.

It is apparent from the smoothly decreasing error functions (3.6 e))that the probe has stabilised between the two reconstructions, and so the additions to the method have aided the convergence. The Siemens star and phase plate features in the object wave fields (3.6 a) and b)) have increased in sharpness and contrast and compare much more favourably with the SEM image. The probe functions (3.6 c) and d)) also seem to look very similar to each other. It is even possible to detect the edge of a slit-like structure to the left hand side of the probe functions.

To try and quantify this somewhat, we can calculate the Fourier ring correlation of the calculated probes from the two datasets as described in section 1.8.1. This is shown in figure 3.7

This curve is far from clean, and indeed it crosses the threshold curve twice; once at 9.6 μm and again at 300-400 nm. Since the 9.6 mum detail actually corresponds to one of the dead spaces between the chips on the Maxipix detector which are floated in the reconstruction, it is perhaps unsurprising that the data here is less well correlated than one would like. Since this information is view independent it is natural that it would be picked up as an artefact in the probe.

For the remainder of the FRC, the two curves nearly cross a number of times, but this mostly happens at around the 350 nm point, hinting that this may be the limit on the resolution of what this data can yield.

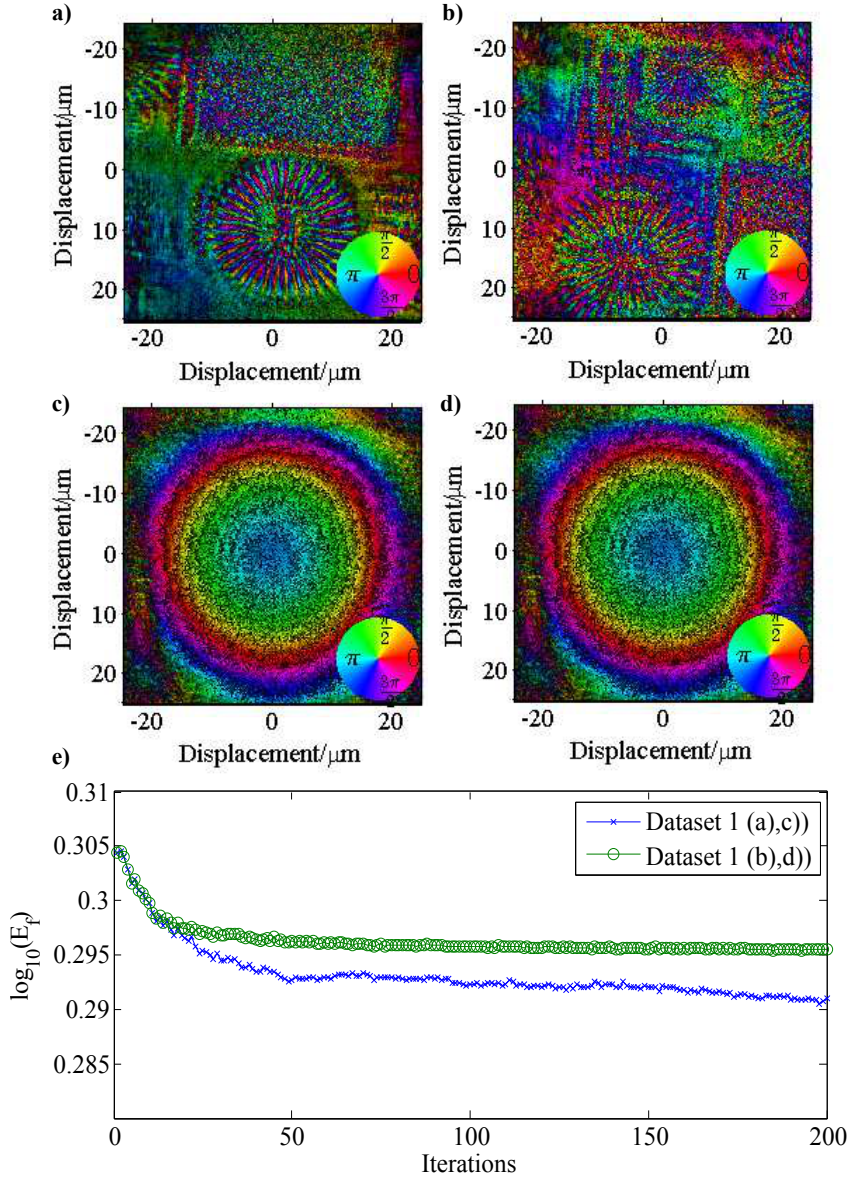

Figure 3.6: The improved ePIE reconstruction using a probe support.a) and b) are the reconstructed wave-fields for both data-sets showing a much sharper and clearer definition which corresponds nicely to the SEM. c) and d) are the reconstructed probe wave-fields corresponding to these object reconstructions. The probe looks very similar in amplitude and phase between the two reconstructions suggesting that an reasonable solution has been found. e) The Fourier error as a function of iteration for both reconstructions. The error comes down smoothly as the algorithm progresses until it reaches a plateau, indicating that the reconstruction has reached a stable solution

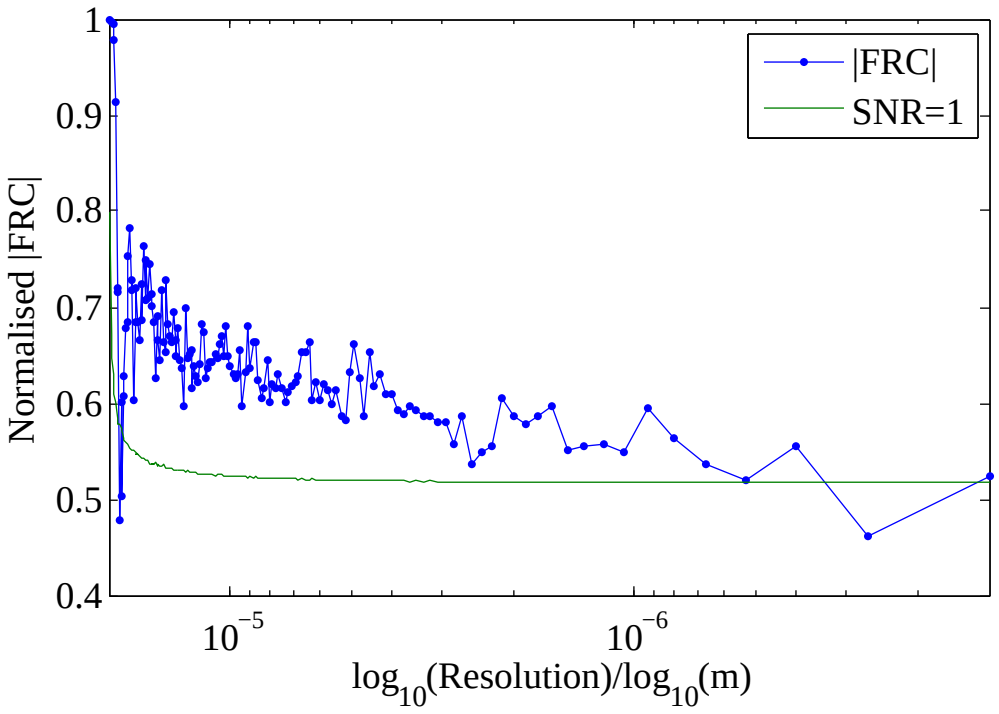

Figure 3.7: The Fourier ring correlation between the two reconstructed probes. The curve shows a strong agreement between the two functions and suggests that the cut-off for reproduceable solutions should be around 350 nm, where the signal meets the noise.

3.1.4 Summary

Before moving on to the results obtained on the HHG source, a new source for iterative ptychography experiments, it is useful to summarise this section in terms of the key points to look for in reconstructing ptychographic data.

1. Applying a support to the probe seems essential to get repeatable reconstructions from real data. Otherwise the probe may tend to move to the edges of the support.

2. If the independence between all views is high, it would seem that a simple modelled probe guess can be used.

3. Using the same probe across two independent data sets improves the stability of the probe and hence object field reconstructions.

4. Floated pixels may cause multiple threshold crossing points and hence issues with the interpretation of the FRC and so a standard cut-off cannot be used for the figure of merit for resolution.

3.2 Iterative ptychography using a High Harmonic source

The previous section of this chapter described a basic experiment using synchrotron radiation to image an extended test object. Iterative ptychography using synchrotron radiation is fast becoming a mainstream technique to characterise a broad spectrum of samples including biological objects at the water-window [81]. However, such sources are ultimately limited by their size, typical coherence properties and also by radiation dosage to the sample.

To complement these experiments, HHG iterative ptychography offers the potential for characterisation of extended samples in the soft x-ray/EUV spectral ranges. Whilst lower in flux and less penetrating than synchrotron radiation, the lower dosage and ease of access available for such sources is a nice advantage.

An example of an experiment that would benefit from such a source is for imaging sensitive tissues such as hippocampal neurons. These samples are of particular interest for the studying of neuro-degenerative diseases such as Alzheimers. In Alzheimers, the neural synapse is subjected to plaque growth. This growth is thought to slow down the transfer for information between neurons. However, the process of the growth and its effects are not yet well understood, and such understanding is vital to the future of drug development.

Ultimately, one would like to image the live cells as they degenerate in a petri dish environment; such a test would be impossible using synchrotron radiation due to its highly ionising nature. However, such images may well be possible to achieve using future HHG CDI/ iterative ptychography experiments. Iterative ptychography would be the preferable technique here since its relatively low sensitivity to noise compared to CDI would allow a lower dose per view. However, to date, no attempts to to apply iterative ptychography techniques or to image biological samples using lab-based high energy photon sources has been reported.

One key reason for the lack of ptychographic results are apparent when one considers the Fresnel numbers of apertures that are required to enforce the support constraint for ptychographic experiments.

For a $5\mu m$ pinhole illuminated by a plane wave at $\lambda = 1.5$Å (7.5 keV) and $\lambda = 27nm$ (44 eV), to achieve a high enough Fresnel number ($F > 2$), and hence maintain a well defined illumination function, the required pinhole to sample distance is given by z where

$$z_{HHG} = \frac{a^2}{\lambda F} = 115\mu m \tag{3.1}$$

compared to

$$z_{synchrotron} = 2cm \tag{3.2}$$

Since the Fresnel number of the focussed HHG beam varies considerably through the Rayleigh range due to the change in radius of curvature (the total Fresnel number being the addition of the source and object Fresnel numbers [6]), z in equation 3.1 can be increased slightly to maintain the same overall Fresnel number. However, this does not alleviate the technical difficulties in achieving this proximity to the sample, and so work on such experiments has been stalled. Indeed some research [82], has suggested that a projected pinhole maybe be used to obtain some phase retrieval results. Whilst this is a useful technique for the visible spectral regime, where optics are considerably easier to fabricate with the required resolution, in the EUV this may be impractical and defeat the advantage of lens-less imaging.

The following sections detail work carried out to engineer a pinhole alignment system that can achieve the required mobility. The sample choice and composition is outlined and some preliminary ptychographic data sets and reconstructions are presented; the first such result using HHG radiation in the world.

3.2.1 Experiment

This section will describe and discuss the experimental procedures and equipment used to record the ptychographic datasets of complex-valued objects using the high harmonic source at Southampton.

Beamline Layout

The beamline layout for this experiment is depicted in figure 3.8 and is similar to the narrow bandwidth set-up used for experiment in chapter 2.

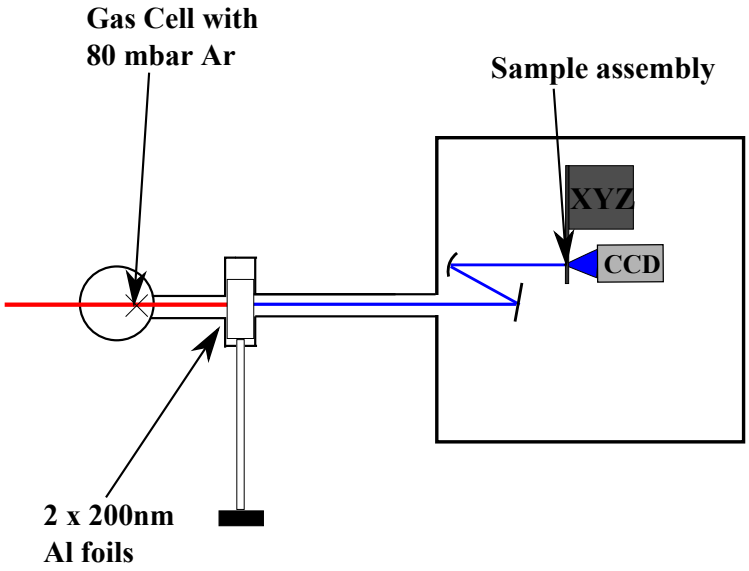

Figure 3.8: A schematic of the ptychography experiment set-up at Southampton. The beam enters from the left and reaches the detector on the right after passing through the apparatus. The experiment is nearly identical to that used in chapter 2, with the exception of a modified sample mounting scheme.

Pulses of 42 fs duration and 1.4 mJ energy at 1 kHz repetition rate were focussed into a gas cell containing 90 mbar Argon. Two sets of Al free-standing thin film filters (Lebow) are used in the beam path to separate the infrared (IR) beam from the generated EUV. These filters are each composed of two 100 nm films layered together to avoid the pinhole effects induced by oxide window formation as was previously discussed in chapter 2. The harmonics were then spectrally filtered and condensed using a combination of two multilayer coated optics. The sample assembly was placed in the plane of the circle of least confusion of the slightly off-axis spherical multilayer mirror.

The resultant speckle patterns were then captured in the far-field on a CCD (Andor DX-434) after 20 mm of propagation in 10^{-5} mbar vacuum. The highest scattering angle recorded during the experiment means that the cropped data provides an NA of 0.15, the pixel size in the sample plane is 90 nm and hence a predicted Sparrow resolution of 180 nm. The oversampling ratio of the signal was 22 allowing the signal to be binned twice to increase the signal to noise ratio.

Sample Preparation

The samples of choice for this experiment were cultured cortical mouse neurons from the hippocampal region and were prepared by Rachel Card, a joint

student between the group and the Institute for Life Sciences (IfLS) also at Southampton. These samples were used instead of a more simple test sample purely due to their availability at the time of the experiment. In this subsection we provide a brief introduction into the structure of hippocampal neurons and show some images from general microscopy techniques of these samples.

The hippocampus is the region of the brain responsible for memory and some motor function. Figure 3.9 shows the location of the hippocampus in a human brain.

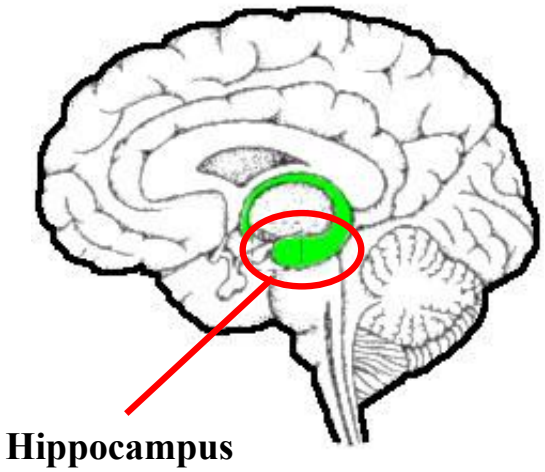

Figure 3.9: A schematic of the hippocampus in a human brain. The hippocampus is responsible for memory and motor function.(Underlying schematic from [83])

One of the reasons for studying the hippocampus is that it is the region of the brain that is affected by neurodegenerative diseases such as Alzheimers and Huntingtons. To understand how such diseases affect the hippocampus, we must consider the process on a cellular level.

Figure 3.10, shows a generalised schematic of a neuron cell with its associated process. Although a neuron may have several dendrites exiting the soma, it will have only one axon, which it uses to send out signals to other cells. The axon is identifiable in general by a myelin sheath which coats the neurite structure [84]. Myelin is a material which not only protects the axon, but also helps electrically insulate the neurite so that it can transmit signals

more quickly and clearly. There are periodic breaks in this structure where the neurite can take on additional ions to change the conductivity of the neurite at that point. These gaps are known as the nodes of Ranvier after Louis-Antoine Ranvier who first recorded them [84]. The gaps are typically under a micron in size.

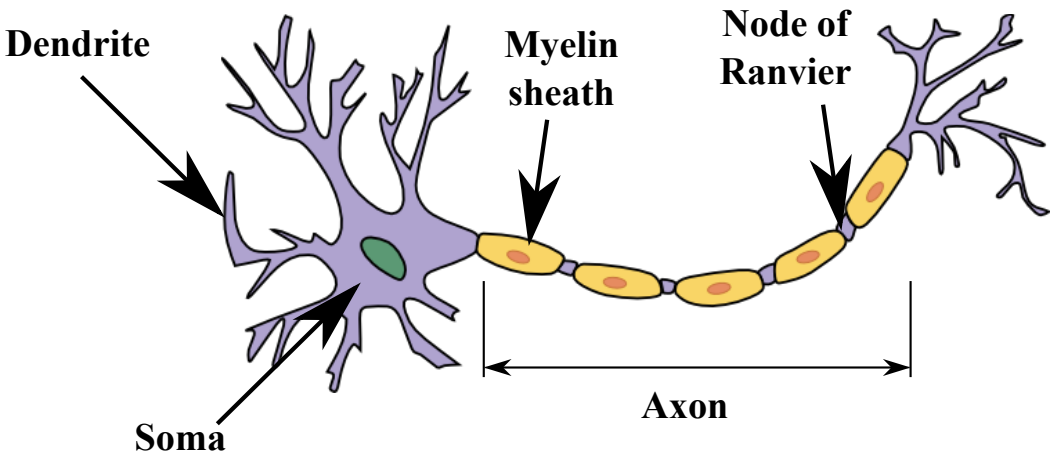

Figure 3.10: A schematic of a neuron. The key parts of interest for this study are the dendrites and axon. Each cell only has one axon, which it uses to communicate with other cells. Axons are identifiable by their myelin sheath, which is broken periodically by a node of Ranvier.([85] for underlying schematic)

In contrast to neurons that are found elsewhere in the nervous system, the myelin sheath around hippocampal axons is very thin, if it exists at all. The neuron samples used for the work in this chapter were cultured from day 3 mice, and such sample shave been previously shown [86] to have not only a myelin layer, but also the Ranvier nodes.

A microscope image of one of the samples used for this thesis is shown in figure 3.11 b) next to a schematic cross-section in 3.11c).

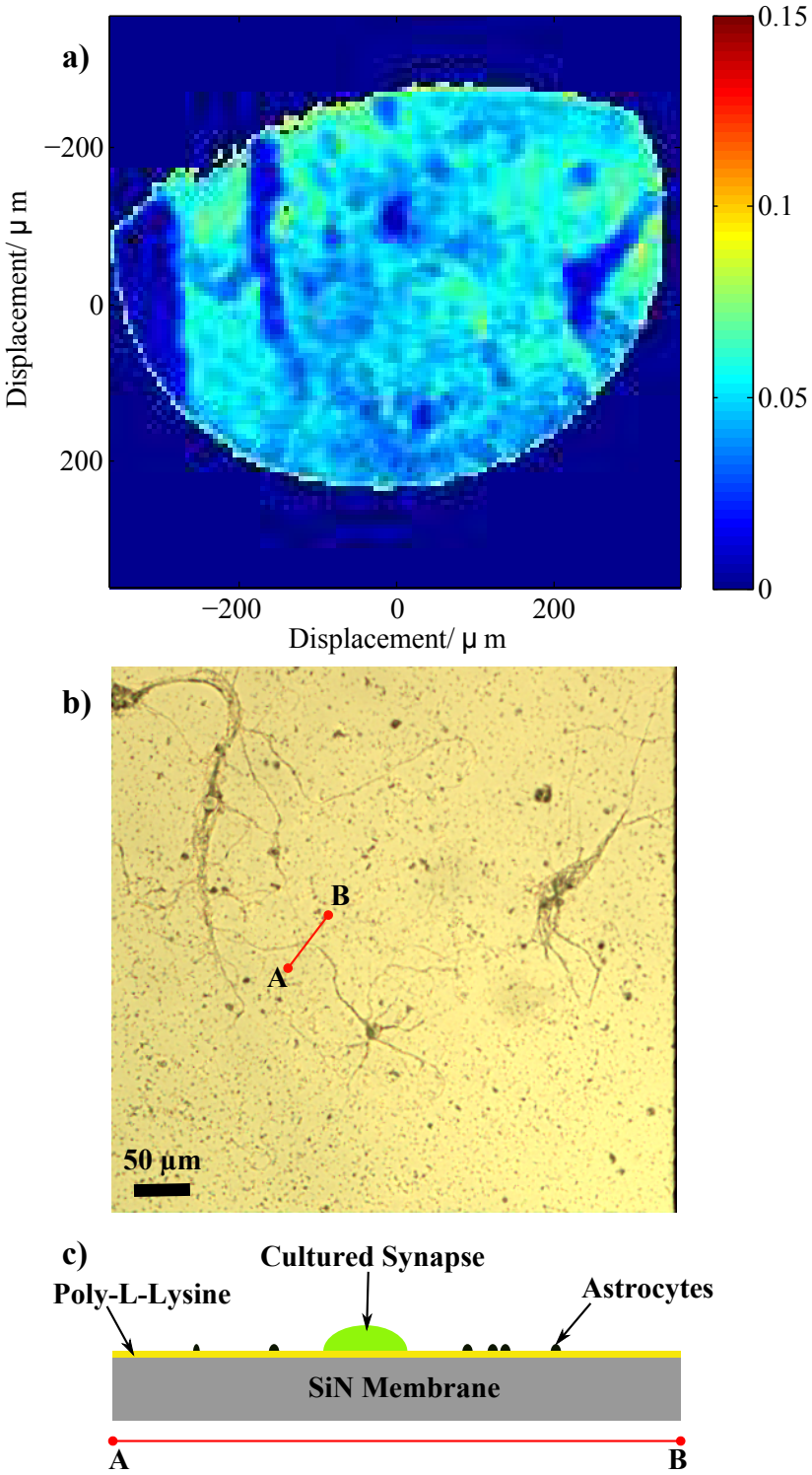

Figure 3.11: a) An EUV shadowgram of the sample to be imaged. The sample was placed away from focus and illuminated with a plane wave. The image is normalised to show the transmission values. b) A light microscopy image of a cultured cortical neuron sample. c) a schematic cross section through the sample to reveal the preparation method.

To prepare the samples, neurons are cultured on to a low-stress silicon nitride (non-stoichiometric SiN) membrane of 50 nm thickness. To ensure the samples grow on the substrate, they are first treated by dipping into a solution of poly-L-lysine, a complex protein. The dissected neurons are placed in suspension in a culture medium above the prepared SiN membrane. The neurons are then cultured for 2 weeks before being fixed using a methanol dip.

Since the culture medium is fairly thick layer (around 30 nm) of organic material, it was useful to check the transmission of the sample before commencing a ptychography experiment. An EUV transmission image was taken by placing the neuron sample in the beam far away from the focus of the system in figure 3.8. By dividing this shadow image by the intensity distribution of the beam when the sample is removed, the spatially resolved transmission values can be found as shown in figure 3.11a). The oval shape of the field of view in this image is due to the shape of the beam at this position, the 5 degree off-axis focussing causing a tighter spot in the horizontal axis.

By comparison of this low resolution EUV shadow image to the microscope image in figure 3.11b) it can be seen that whilst the main bodies of the cells are too thick for transmission at this wavelength, the thinner neurites are transmissive. It can also be seen that the poly-L-lysine coating also has a slightly variable transmission.

The dendritic structures corresponding to the processes of the neurons, the part of the sample under investigation, correspond to spatial frequencies that are below the diffraction limit of the 20x 0.4NA objective used to produce figure 3.11. Even when a more powerful 40x 0.6NA objective was used (figure 3.12a)) to image another sample from the same cultured batch, the image suffers from poor contrast due to the dynamic range of the detector; the increased contrast is part of the reason why using EUV as the probe is desirable. However the resolution of the EUV shadow image in 3.11a) is still too poor to define any dendritic structures.

For this reason, these cultured samples were also characterised by dark field optical microscopy using the same objective 3.12 c) and scanning electron microscopy (SEM) 3.12b), the latter being carried out by Jennifer Holter (Research Complex at Harwell). Figure 3.12d) is a software processed version of 3.12b), where the colour map has been inverted and the contrast improved by the imageJ processing package. This was carried out in order to make it easier to pick out the dendrites by eye.

It can be seen that in the dark-field and SEM images, the sample appears to be criss-crossed with many dendritic features. These are the neural processes that are sent out from a living neuron. When two of these meet they form a synapse over which information can be exchanged between the

cells. The joined processes are then termed neurites, and understanding of their structure, connection and degeneration is an essential tool in the search for cures for Alzheimers and other neuro-degenerative diseases. It is these structures which the following experiment attempts to image. Figure 3.12e) is a cross section through one such section, marked out by the red line in 3.12d), showing that it is roughly 100 nm across.

These images are of a sample from the same preparation batch as the one used in the ptychography experiments.

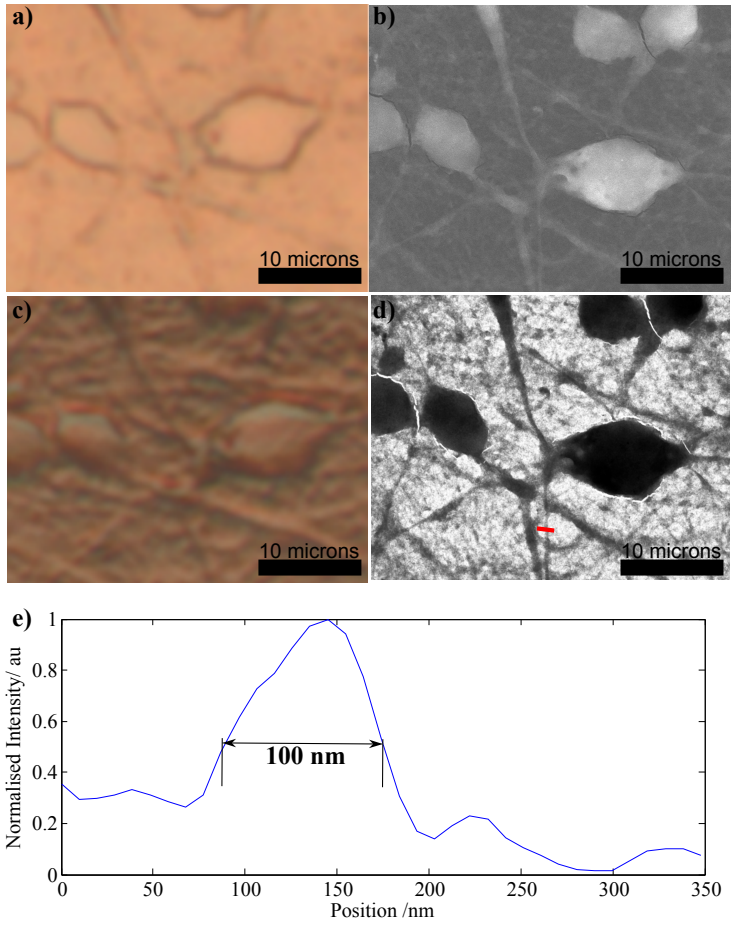

Figure 3.12: Optical bright field a) and dark field c) images of an example neuron structure using a 40x, 0.6NA objective. b) An SEM of the same sample scaled to the same field of view. d) An image processed version of b) showing better contrast. All images exhibit the same criss-crossed pattern of dendrites.

Aperture assembly

To define the support for ptychography, a laser drilled molybdenum 5 μm pinhole (Edmund Optics) is used. This is glued to a self-made support piece shown in figure 3.13 a). This piece fits into a $\frac{1}{2}$" mirror mount (Thorlabs) which in turn is attached to another self-made mount. This attaches to the front of the frame of a Princeton Instruments (PI) piezo stage (model 733). The sample is mounted on a plate on the moveable centre of the stage.

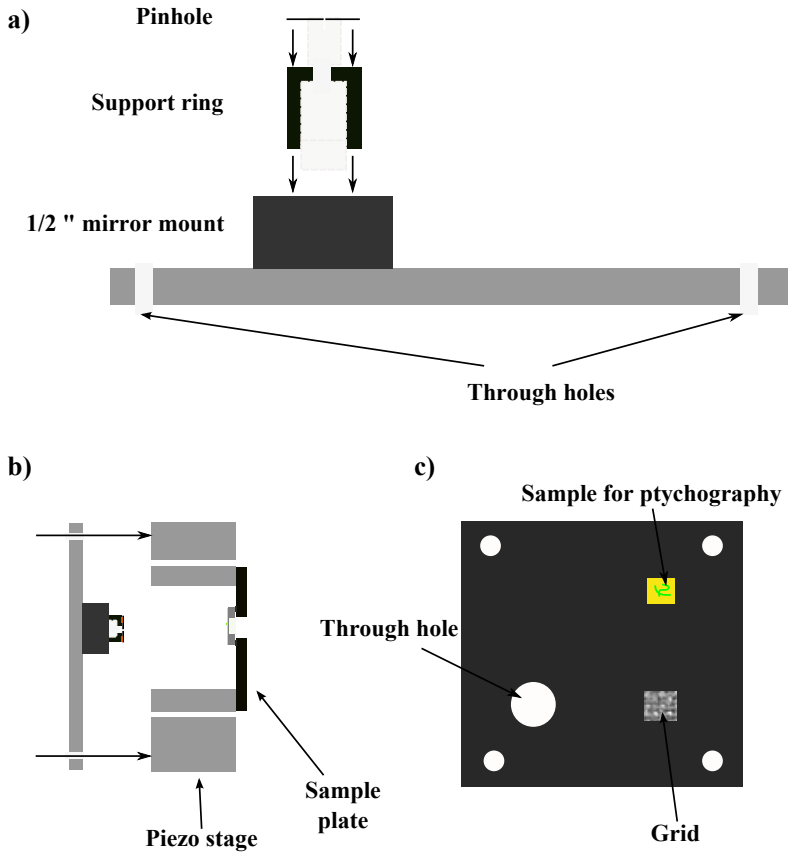

Figure 3.13: A schematic of the sample.a) The pinhole mounting system. This was attached to the stationary outside frame of the piezo stage mount, while c) shows the sample mount itself, which was mounted to the moveable part of the piezo stage so it could be scanned behind the pinhole.b) shows how the parts were assembled.

To align the pinhole to the sample, a travelling microscope technique is employed as is schematically shown in figure 3.13a). By illuminating the sample and pinhole from the top and bottom it is possible to bring the

surface of the pinhole to within 10±2 μm. Figure 3.14b) shows the finished alignment viewed via a 20x 0.4NA objective under illumination from both sides of the sample.

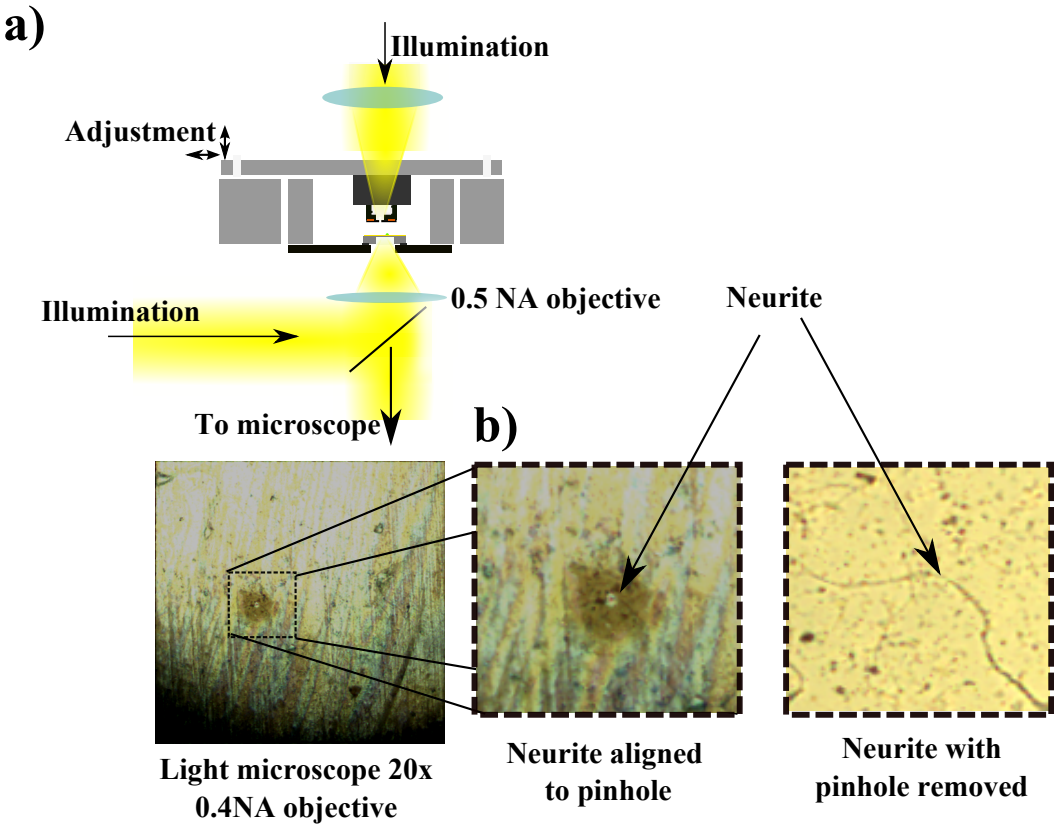

Figure 3.14: a)The sample-pinhole alignment technique. The pinhole was both back and front illuminated so that it could be seen at the same time as the sample. Since the sample is optically transparent, the pinhole could be brought down using a calibrated travelling microscope technique until it sat $>$ 10 microns away from the sample. The pinhole was then translated by hand to align to the sample until it was in range of the piezo-stage travel. b) The finished alignment with the pinhole aligned to a neurite on the substrate.

3.2.2 Raw data collection and analysis

The exposure time for a single view of the ptychography experiment was 4 minutes, with a readout time of 32 μs per pixel. A previous beam stability experiment using the same sample at a fixed position shows that the speckle pattern slowly drifts over the course of an hour (figure 3.15a)) an effect attributed to the thermal drift of the oscillator coupling into the amplifier.

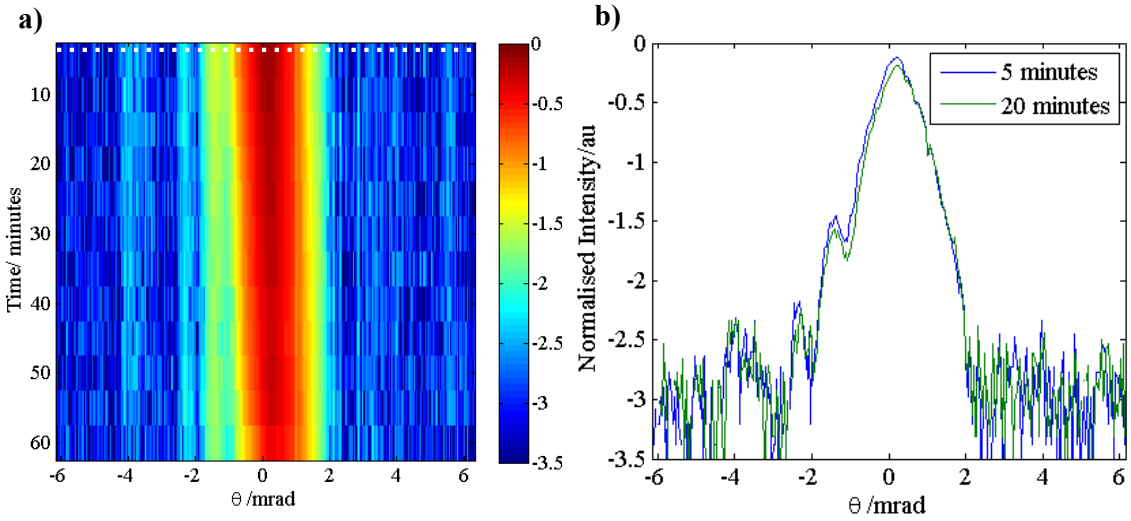

Figure 3.15: The far-field movement of the beam through the 5 μm pinhole vs. time. a)A $\log_{10}$ plot of vertical slices through the centre of the far-field speckle pattern of the pinhole aligned over an empty region of the sample are shown vs. time over an hour. It is apparent that over this time there is a slight (80 μm) drift to the right hand side of this plot, demonstrating the beam moving down on the detector. To minimise the impact of this on the ptychography experiment, the experimental duration was kept to 20 minutes.b) A comparison of the speckle patterns after 5 and 20 minute intervals showing minimal change in their structure.

For this reason, only 4 views were taken for each ptychographic dataset to ensure that the beam stayed stable throughout the course of the experiment. A total of 2 datasets were taken during the experiment over two independent areas of the sample. Since only a small number of views were to be collected, a raster scan of data was taken, with an offset in each direction to attempt to reduce grid artefacts appearing in the data, a technique described in [50]. The two regions which data were taken over correspond to the neurite region of the sample isolated and shown in figure 3.14 (data set 2) and another arbitrary region of the sample taken as a reference and chosen for its higher transmission (data set 1).

Since the oversampling for this data is very high, a consequence of working in the far-field at EUV wavelengths, the background subtracted data can be binned twice in each dimension without losing any information, increasing the signal to noise of the data [31]. Also the data is cropped to the outermost spatial frequency visible above the noise. Due to the relatively low NA of this experiment, the small angle approximation still holds and so no further

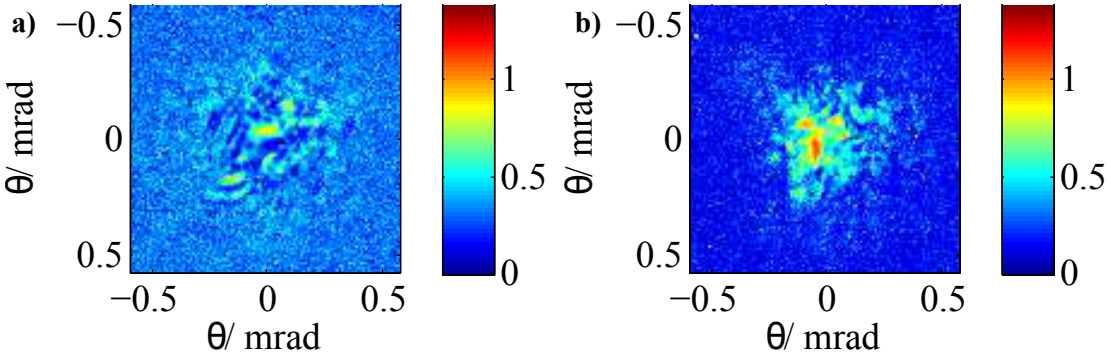

Figure 3.16: The two dimensional mean normalised variance of data-set 1 a) and data-set 2 b). Since their are a lot more view dependent speckles than independent ones, we can deduce that the probe may be poorly constrained in the reconstruction.

projection to the Ewald sphere was necessary.

As with the synchrotron data in the previous section, it is useful to plot the 2-dimensional $\frac{\sigma}{mean}$ for each pixel as shown in figure 3.16a) for the first data set and 3.16b) for the second dataset.

Although the number of data points for each pixel is small here compared to the synchrotron data, it is still useful to note any outliers to the distribution which can be removed as noise and floated in the reconstruction, as explained for the synchrotron experiment.

Figure 3.16 also shows that, although the data is limited in terms of resolution by the maximum scattering angle recorded, it is still possible to discern regions where the speckles are independent and regions where they are related. Unfortunately, there are a lot more view dependant speckles than independent ones and so we can expect the the probe reconstruction to be poorly constrained, although the object should be relatively well defined.

Probe reconstructions

Learning from the experiments at I13, we know that it is useful to focus on the stability of the probe as an indicator of good reconstruction. A perfect circular pinhole was initially assumed in the form of a top hat function for use in the reconstructions, backed up by a support of 70% of the the probe area as described in section 3.1.3. The probe was fixed for the first 10 iterations of the algorithm and then allowed to update according to the standard ePIE rules. The reconstruction that was obtained from the first data set is shown in figure 3.17, next to 2-dimensional means and standard deviation maps of the reconstructed field starting from 50 different random seeds.

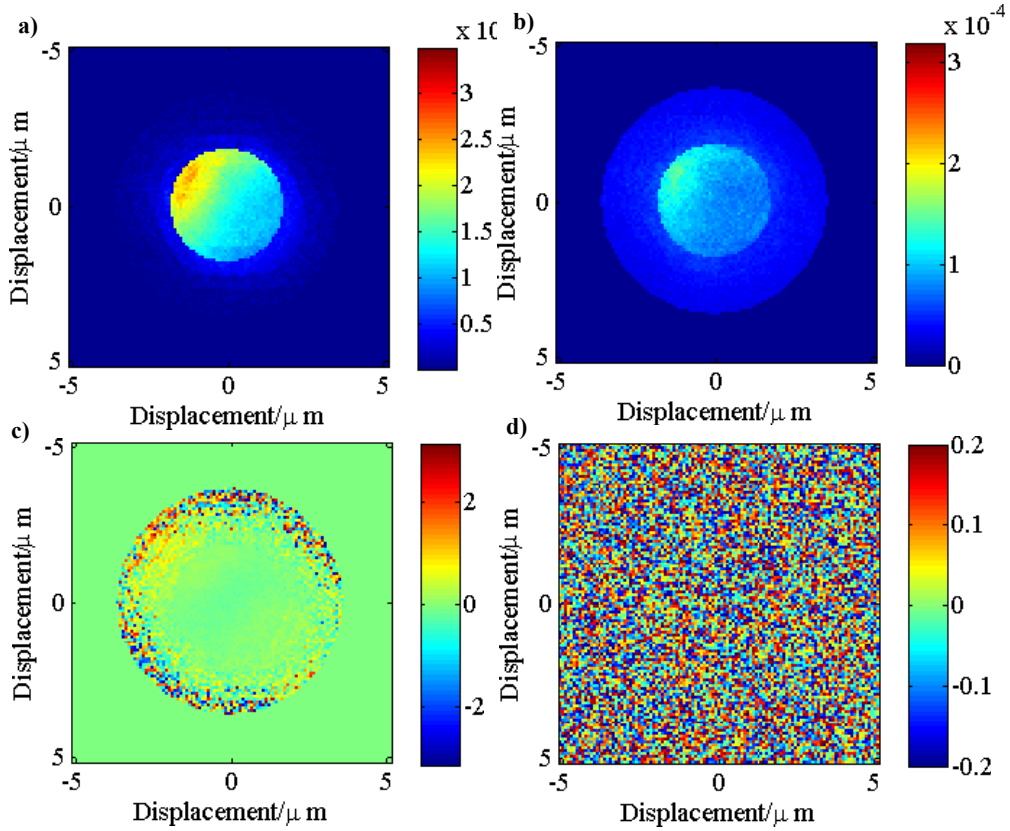

Figure 3.17: Probe reconstructions from data-set 1 using a top hat model probe to start with a) The average and b) the mean normalised variance of the probe wave-field magnitudes c) The average and d) the mean normalised variance of the probe wave-field phases. It is clear from the lack of structure in the variance of the phase that this probe guess has not helped the algorithm to converge to a solution.

and from the second set in figure 3.18.

By looking at the large variance in these reconstructions, it can be inferred that these reconstructions have not worked and are too unstable to make any concrete statements with regards to the object or probe. The reason for this is that, as shown in figures 3.16a) and b), the constraint on the probe is not strong due to the small amount of data collected. It should therefore be expected that we would have to put in a better starting guess for this function. However, ideally information from external sources or microscopy technique would not be entered into the algorithm, since this loses the *a priori* nature of the algorithm.

By re-examining the plots in figure 3.16, it is possible to improve our

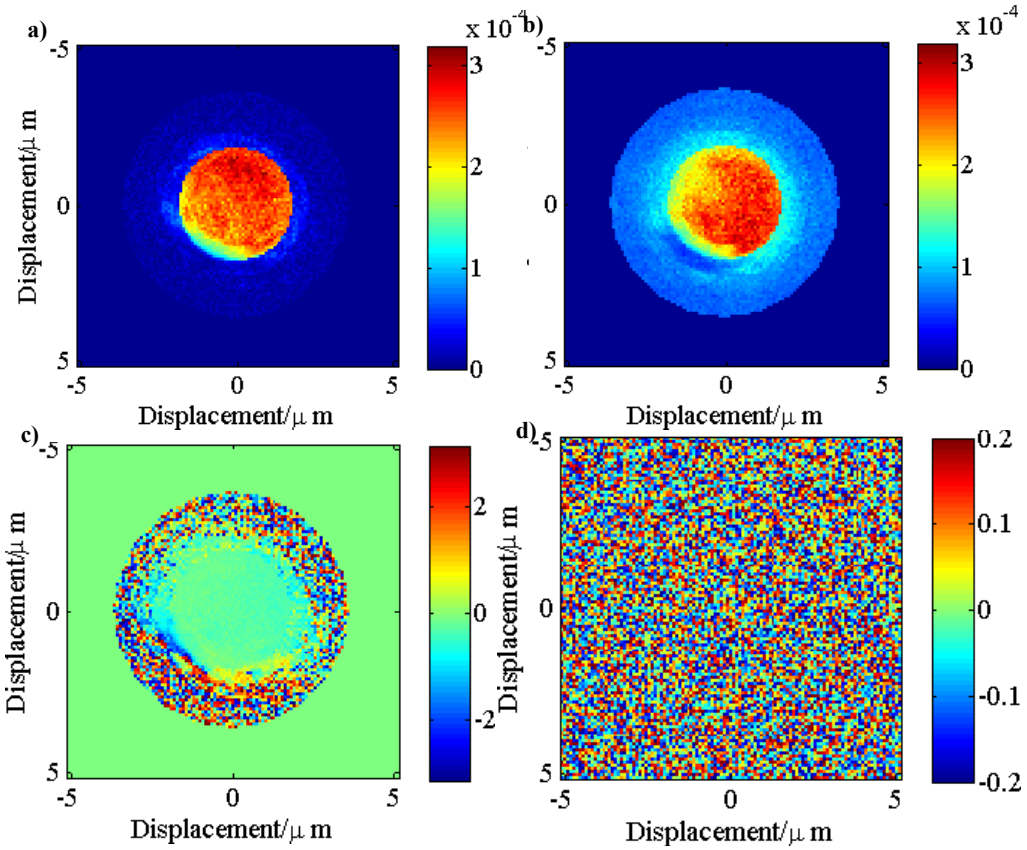

Figure 3.18: Probe reconstructions from data-set 2 using a top hat model probe to start with a) The average and b) the mean normalised variance of the probe wave-field magnitudes c) The average and d) the mean normalised variance of the probe wave-field phases. It is clear from the lack of structure in the variance of the phase that this probe guess has not helped the algorithm to converge to a solution.

estimate of the probe function by first selecting the parts of the averaged speckle pattern that are have a low $\frac{\sigma}{mean}$ from each data set and averaging them. By inverse Fourier transforming this pattern and thresholding at 0.5% of the maximum amplitude, provided an improved estimate of the probe support is obtained as shown in figure 3.19, a function related to the probe autocorrelation.

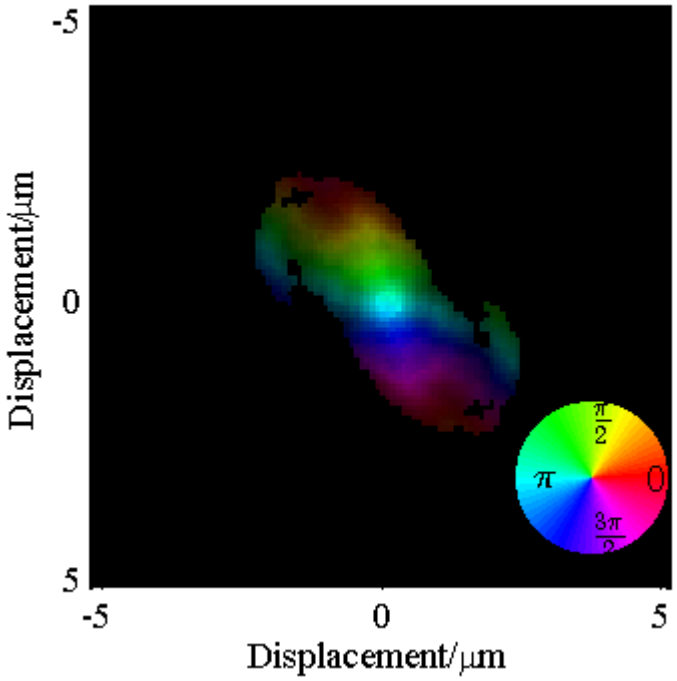

Figure 3.19: The magnitude and phase of the crude probe autocorrelation obtained from the low variance data in both data sets. This was entered into the algorithm as an improved starting guess for the probe.

The processing chain that was followed to optimise the data is shown in figure 3.20 for clarity. The new probe function shown in 3.19 was used in the ePIE reconstruction for the first dataset, and the updated probe from this entered into the second dataset. This process was then continued, iterating between datasets and keeping the output probe from each step as an improved starting probe. Initially the probe function was supported with a mask of 50% of the area of the probe array. This support was gradually increased in size until it was no longer needed in the reconstruction. A total number of 5 steps on each data set running for 200 iterations were required until the Fourier error reached a stable plateau. Finally this probe function was used

to run the reconstructions again, independently for each data set, starting from a random noise guess for the object. These reconstructions were run 50 times over 1000 iterations each in order to provide some statistics that can be used to judge the degree of confidence we have in the retrieved values.

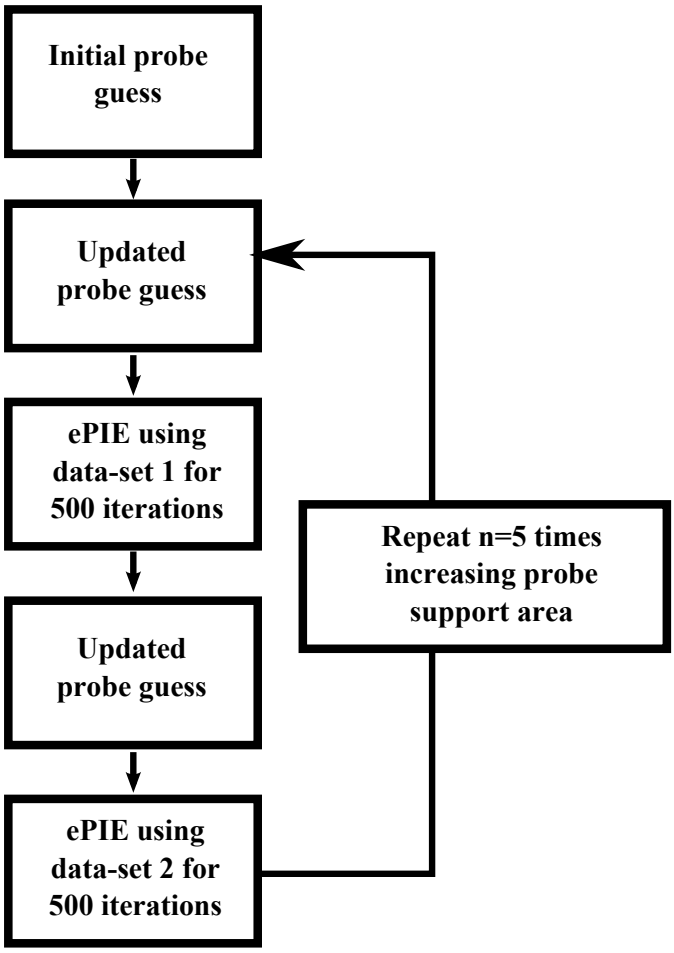

Figure 3.20: The processing chain that was followed to improve the reconstructions. The process was iterated 5 times before a good convergence was found.

Note here that no external information has been added to the algorithm, just an average between two independent data-sets.

The reconstructed averages and mean normalised variances obtained from this process for the probe (a) and b)) and the object (c) and d)), alongside an example of their Fourier errors, are shown in figures 3.21 and 3.22 for data-set 1 and data-set 2 respectively.

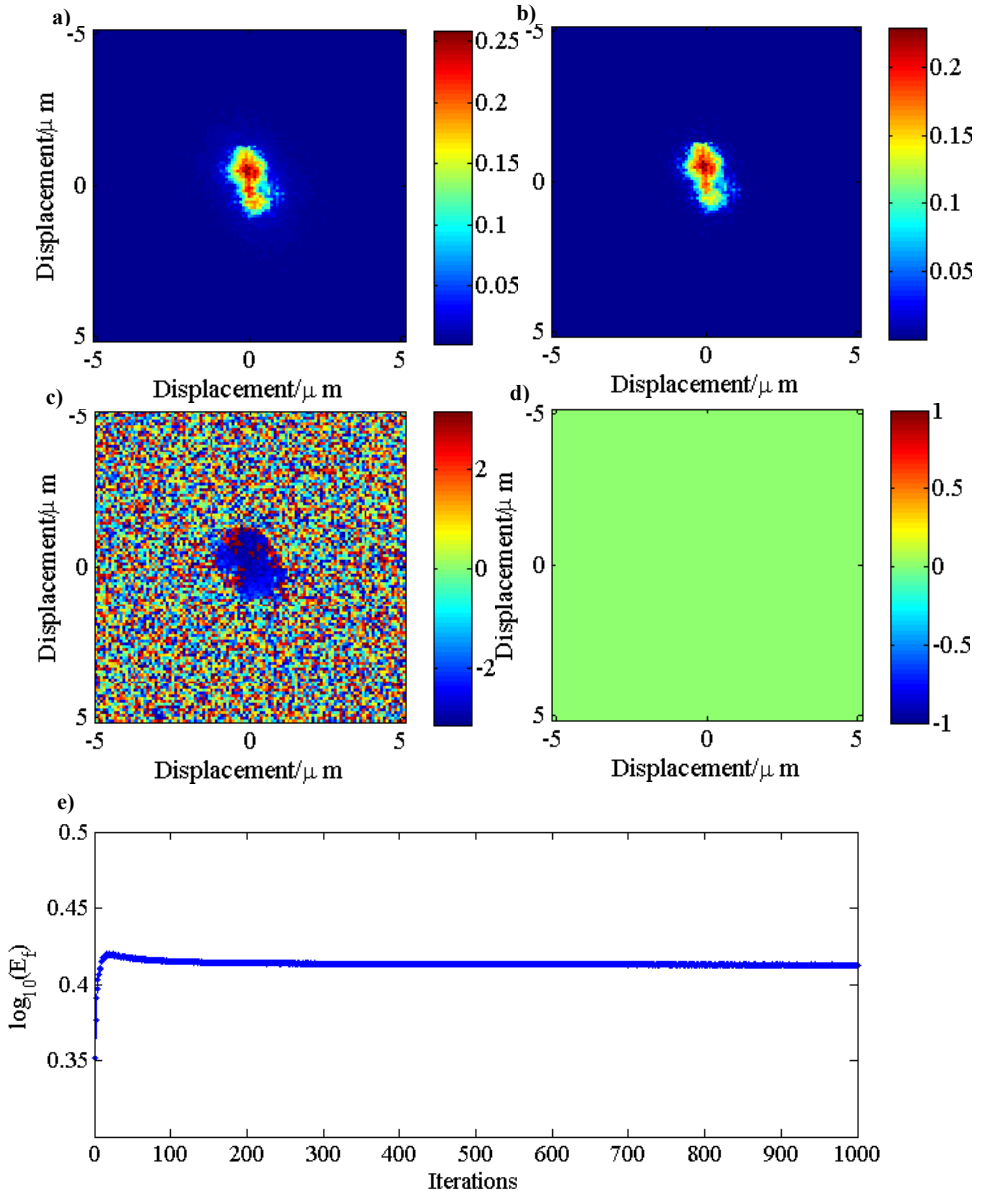

Figure 3.21: Improved reconstructions from data-set 1 using an improved probe guess a) The average and b) the mean normalised variance of the probe wave-field magnitudes c) The average and d) the mean normalised variance of the probe wave-field phases. The low variance and well defined probe suggest that the algorithm has converged.e) The Fourier error of the reconstruction. The smoothly decreasing nature of this further hints that the algorithm has found a good solution. The initial 10 iterations show the error increasing since the probe was held fixed over a free-space guess of the object.

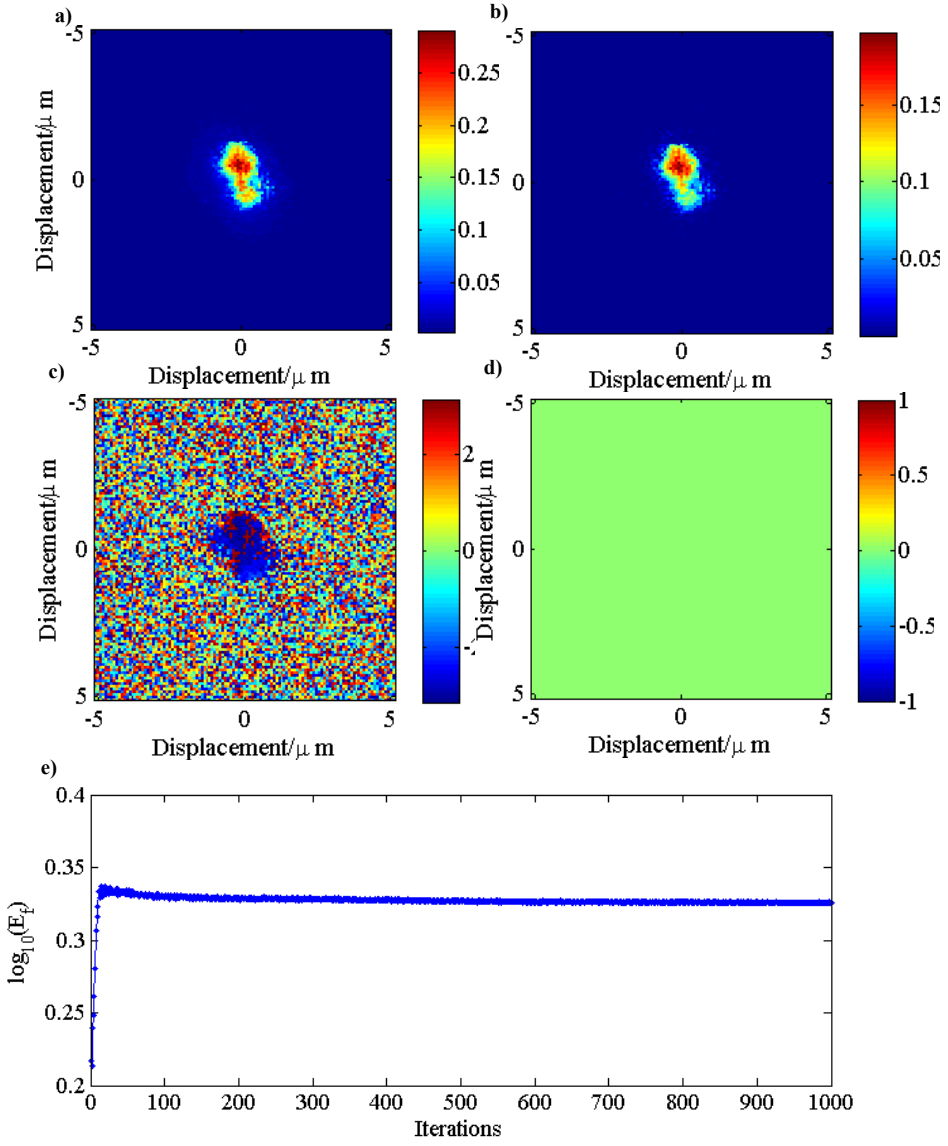

Figure 3.22: Improved reconstructions from data-set 2 using an improved probe guess a) The average and b) the mean normalised variance of the probe wave-field magnitudes c) The average and d) the mean normalised variance of the probe wave-field phases. The low variance and well defined probe suggest that the algorithm has converged.e) The Fourier error of the reconstruction. The smoothly decreasing nature of this further hints that the algorithm has found a good solution. The initial 10 iterations show the error increasing since the probe was held fixed over a free-space guess of the object.

The probe reconstructions are very stable indeed with respect to the recovered probe function, showing a low mean normalised variance (0.5%) over each data set. The Fourier errors for both reconstructions also look to come down smoothly and end at a plateau which could not be improved upon with further analysis. The initial ramp on the Fourier error for both data-sets is caused by the first 10 iterations being run with a non-updating probe. This is a standard step in ptychography and is used to push the object function into a reasonable starting position before both the probe and object functions are allowed to update.

The shape of the probe is certainly not circular as was previously assumed. To investigate the reasons for this anomaly, an SEM was taken of the pinhole after the experiment for comparison to the reconstructed function. The SEM is shown in figure 3.23c)with the average probe reconstruction from data-set 1 3.23a) and from data-set 2 in 3.23b). The SEM has here been scaled to the same pixel size as the ptychogram, and also its orientation has been rotated to match the same co-ordinate system.

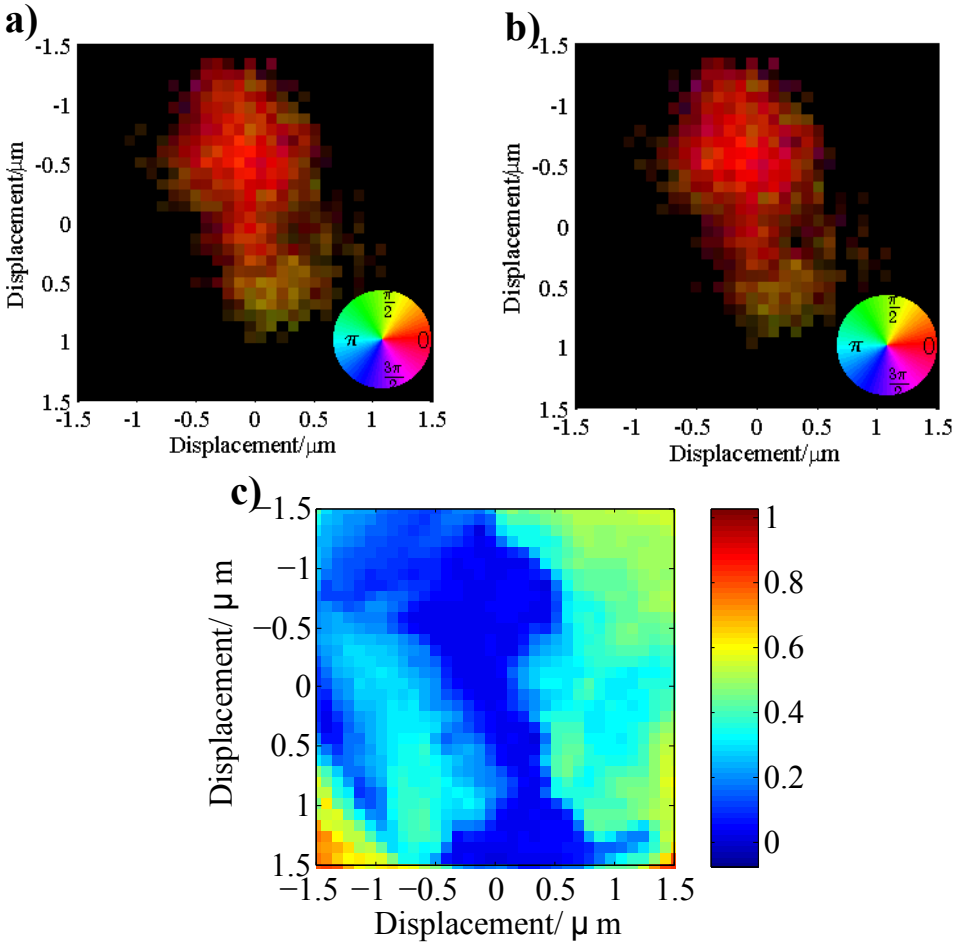

Figure 3.23: The average full field probe reconstructions for a)data-set 1 and b) data-set 2 over 50 independent reconstructions;)c) the SEM of the pinhole on the same grid size as the reconstructions and rotated to match the orientation of the reconstructions.

The SEM in 3.23c) shows that the aperture is definitely not circular, instead containing a thin layer of residual Molybdenum from the laser ablation process. Indeed it looks very similar indeed to the reconstructed probe from the ptychogram, and it is possible to make out the partially transmitting region of the Molybdenum in the probe reconstructions. The next subsection uses this information to attempt to calibrate the thickness of this defect region, but for now we focus on verifying the validity of the reconstruction.

Since the SEM contains inherently different information to the HHG ptychogram, it is not possible to perform a more detailed analysis of this comparison, except this initial verification that they do look the same. Instead,

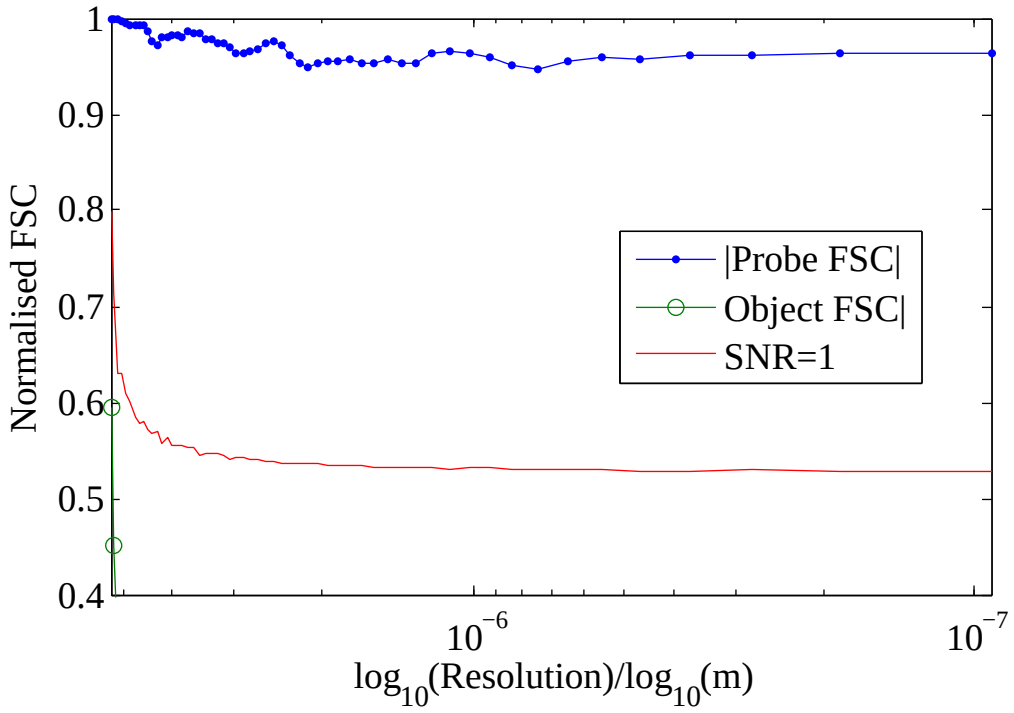

Figure 3.24: The Fourier ring correlations between the probe wave-fields (blue line) and the object wave-fields (green line) from each independent data-sets. The lack of correlation between the object fields shows that the data-sets are indeed independent, while the strong correlation between the probe fields shows that the probe solution is consistent across both data-sets. The red line shows the cut-off where the signal meets the noise.

since two independently measured and reconstructed ptychograms are shown which are formed by averaging over multiple reconstructions from the same data, we can check the reliability of the information by finding the Fourier ring correlation (FRC) as we carried out for the synchrotron data. This FRC is shown in figure 3.24, along with the FRC of the object reconstructions to confirm the assumption of independence of the data sets.

From the information in figure 3.24 it can be concluded that the two probes are indeed strongly correlated over the entire range of spatial frequencies present in the reconstruction, meaning the result is diffraction limited instead of noise limited; in contrast, the object field reconstructions are not correlated at all, with the correlation coefficient dropping straight to 0 aside from a small correlation of the background 'DC' frequencies. This suggests that a larger section of the raw data could have been used in the reconstruc-

tions to gain higher resolution. However, as shown in figures 3.16, the data does not provide any significant information over the noise outside of this region. From this, we can be satisfied that we have achieved the best fit to the recorded data possible and can proceed to use this information to make some statements about both the probe and object fields.

Pinhole defect analysis from HHG ptychography

In this subsection we will try to make some concrete statements about the nature of the defects seen inside the aperture used.

Although Molybdenum is a good electrical conductor, and so would ground most organic material in the formation of an SEM, none of the defect material showed any inclination to charge during the measurement. For this reason, the defect can be attributed to a defect in the manufacture of the pinhole and not any of the materials used in the sample preparation. For this reason it is a relatively safe assumption that this defect material is redeposited material from the laser ablation process used to manufacture the pinholes.

With this in mind, we can convert the exit-wave field (EWF) of the probe, into a thickness function for the material. For an EWF $U(x, y, z, \lambda)$ measured at wavelength λ, the thickness function $T(\rho)$ for a material of density ρ and complex refractive index $n(\lambda)$ can be expressed as equation 3.3.

$$U(x, y, z, \lambda) = \exp[\frac{i2\pi}{\lambda} n(\lambda])T(\rho)] \tag{3.3}$$

which can be rearranged as

$$T(\rho) = \frac{-i\lambda}{2\pi n(\lambda)} \ln[U(x, y, z, \lambda)] \tag{3.4}$$

The refractive index in the EUV and X-ray regions of the spectrum can be expressed as equation 3.5, where $f_1(\lambda)$ and $f_2(\lambda)$ are the atomic scattering factors in the forward direction and r_e is the classical electron radius.

$$\begin{aligned} n(\lambda) &= 1 - \delta(\lambda) - i\beta(\lambda) \\ &= 1 - \frac{r_e}{2\pi}\lambda^2(f_1(\lambda) + if_2(\lambda)) \end{aligned} \tag{3.5}$$

By calculating $n(\lambda)$ using values for the scattering factors obtained from CXRO [78], we can calculate the 2-dimensional thickness functions for both average probe functions as shown in figure 3.25a) and b) for data-sets 1 and 2 respectively. Since the wave-field incident on the pinhole is unknown and

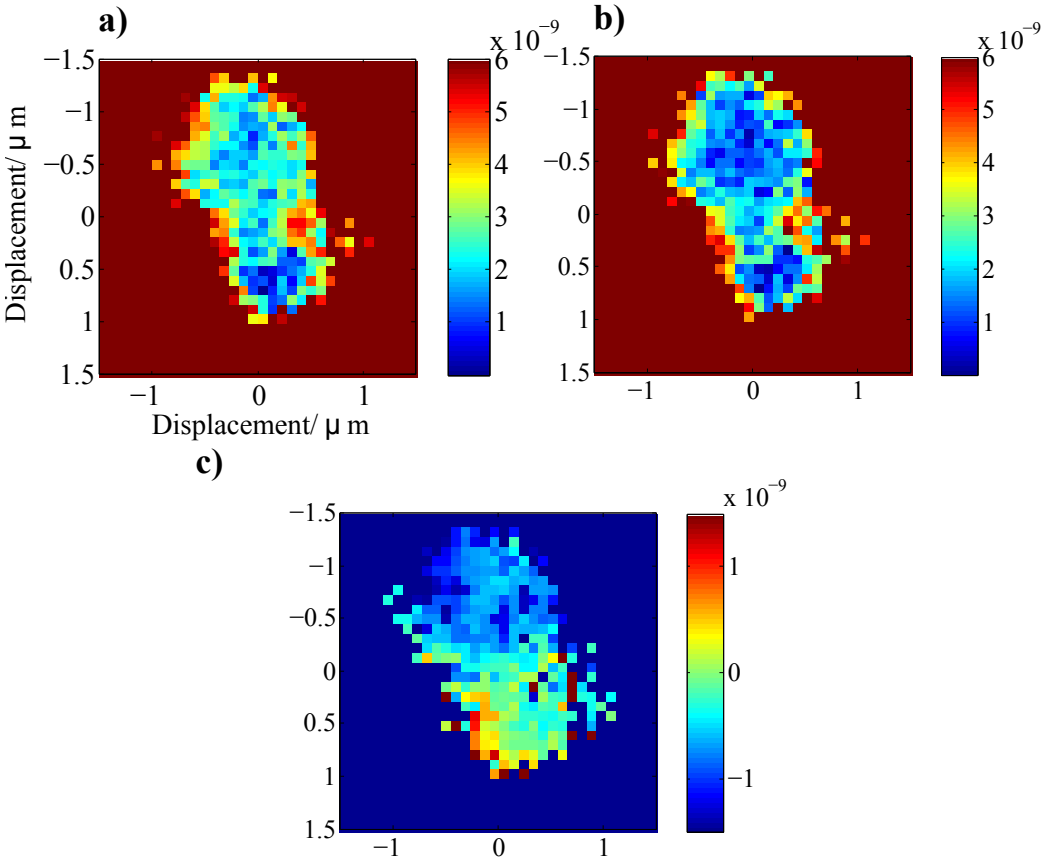

Figure 3.25: The magnitude of the thickness functions for the average probe reconstruction for data-set 1 a) and data-set 2 b). c) the difference between the two thickness functions providing the error in measurement of this thickness. The colormap in all these plots is indicative of thickness, with the units in m.

hence the incident intensities and phases are also unknown, an assumption of plane wave incidence has been made and the minimum "thickness" in these arrays have been subtracted from the other data points to provide absolute values.

To calculate a rough error range for these measurements, the thickness functions in figure 3.25 a) and b) were subtracted from each other with the result shown in figure 3.25c). Hence we can say with some certainty that the defects in the pinhole are 5.5 nm ± 1 nm thick at the thickest part.

3.2.3 Object wave-field reconstructions

The stability and repeatability of the probe wave-field analysed in the previous subsection show that we can trust the validity of this reconstruction. Since the probe and object functions are coupled in the reconstructions, the fact that one of these functions is well defined, suggests that the other will be stable and reliable also, and so we can move straight in to the interpretation of the results, without requiring further validation.

Since two data-sets were taken during the experiment, corresponding to two independent object wave-field reconstructions, it makes sense to consider each one in turn in order to extract the maximum useful information. Since, from figure 3.16, it was concluded that data-set 2 (3.16 b) contained the most information about the object, this data set will be investigated first.

3.2.4 Object field analysis from data-set 2

The initial reconstruction of the object wave-field from data set 2 was introduced in figure 3.22 whilst the reconstructions were being optimised. They were ignored initially whilst we optimised and analysed the probe information, but are now reproduced in more detail in figure 3.26.

Figure 3.26 a) shows a zoomed in plot of the complex object field. Since the 4 scanned probe points were not enough to fill up the field of view, and the starting guess for the object was an array of random numbers, we can improve the object reconstruction by applying a mask to this field. A suitable mask was found by scanning the probe magnitudes according to the recorded views and summing them. The resultant distribution was then thresholded at 10% of the maximum to produce the final mask shown in figure 3.26 b). Applying this mask to the reconstruction gives the result shown in figure 3.26 c).

Figure 3.26 c), although consistent with the data, gives little in the way of usable information about the features of the object exit wavefield.

The reasons for this become apparent, when we consider the fact that the reconstruction of the probe function was in focus. We know from the alignment of the sample using the travelling microscope technique that the defining pinhole is within 10 microns of the sample substrate. However, the plane of reconstruction has been defined as that of the pinhole due to its strongly scattering nature. A schematic of the sample layout with respect to the pinhole is shown in figure 3.27 as a reminder of what we should expect to see.

Since the full field is known at this position, it is possible to propagate the function forward until the plane where the sample is in focus by considering

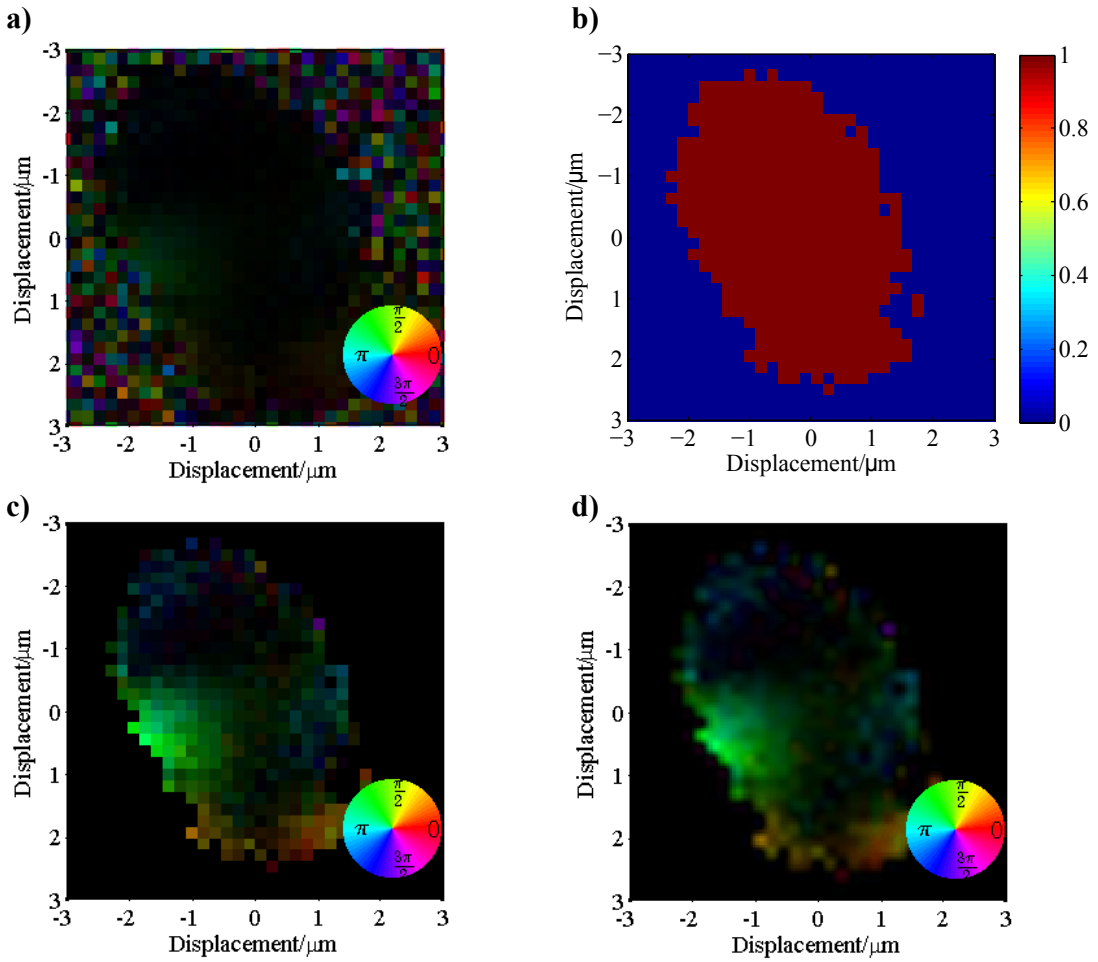

Figure 3.26: The reconstructed object for data-set 2. a) The mean average object exit wave field over 50 independent pseudo-random starting seeds. b) A binary mask of the reconstructed field of view formed by addition of the reconstructed probe magnitudes at the 4 scan positions. The resultant magnitudes were then thresholded at 10%. c) The reconstructed field shown in a) multiplied by the mask in b). d) The field of view in c) interpolated twice by padding in Fourier space to increase the sampling rate. No extra information is added in this process.

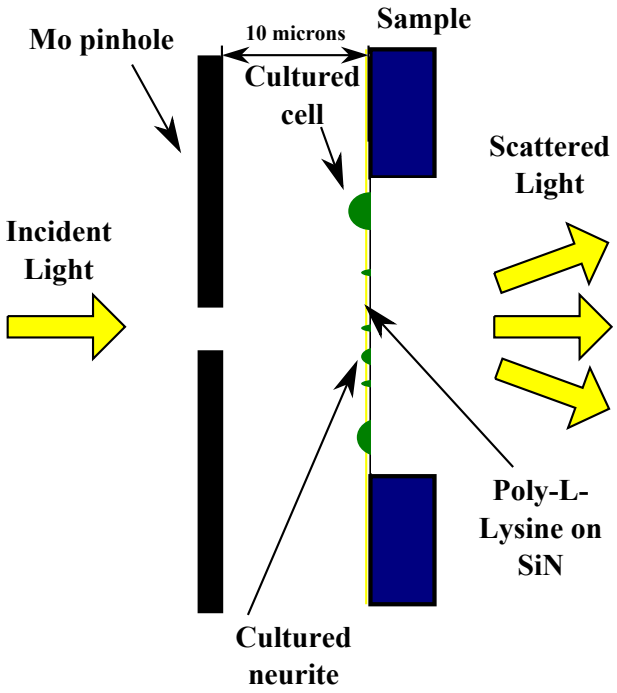

Figure 3.27: A schematic of the pinhole and sample layout showing which order the elements interact with the EUV radiation. The light is incident upon the pinhole first. After this, it progresses onto some of the larger neuron cells, which will be closest to the pinhole. This is then followed by the thinner dendritic structures and then the Poly-L-Lysine coated SiN

the propagation of the angular spectrum of the sample, as explained in depth in section 1.3.2 and re-iterated here in equation 3.6.

$$\tilde{U}(\alpha, \beta, z') = \tilde{U}(\alpha, \beta, 0) \exp[ik_z z' \{1 - (\alpha^2 + \beta^2)\}^{\frac{1}{2}}] \tag{3.6}$$

The propagation of the angular spectrum works best when the signal at $z = 0$ is finely sampled. However, with the current wave-field shown in figure 3.26 c), this is not the case. Instead the wave-field was up-sampled by a factor of two by padding the angular spectrum with zeros. Fourier interpolation is the best choice for this smoothing process since it adds no extra information to the data, unlike the assumptions of spline interpolation. The result of this interpolation is shown in figure 3.26 d) and shows that no artefacts have been picked up in the transformation.

The function can now be propagated through via the ASM. Since the object is an organic compound, and hence the refractive index is hard to determine, the refractive index for the ASM propagation will be set to unity. This does limit the interpretation of the result, as will be discussed later, such that a true thickness function cannot be determined. However, this is a standard limitation of just considering the forward projection of the object; to fully characterise the object in question would require a full tomographic scan of the ptychograms would need to be collected. This type of "ptycho-tomo" experiment is frequently carried out at the Swiss Light Source (SLS), a synchrotron based source, but currently is beyond the scope of lab-based sources. Alternately, reconstructions using different wavelength probes could be considered to distinguish between the dispersive change and the density, however the equipment required for this was not available at the time of the experiment.

Figure 3.28 shows some cross sections through the interpolated array as it is propagated, figure 3.28a) being the reference for the cross sections in 3.28b). Ignoring the scattering from the "pinhole" effect of the limited field of view, it is possible to identify several points where the wave-field is in focus at various obstructions. These are shown in the figure by white arrows, and are identified by tracing back the scattered rays to their source.

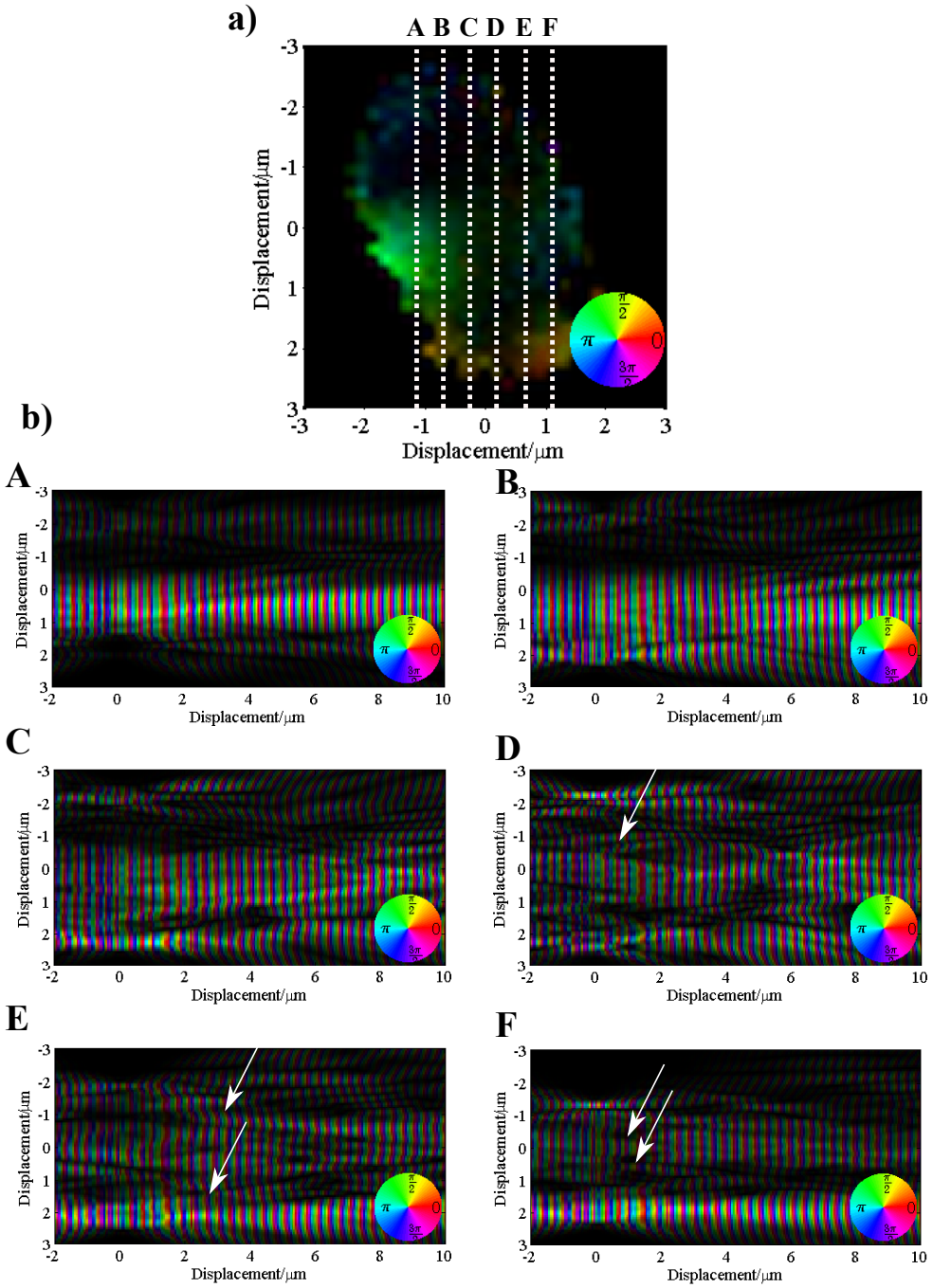

Figure 3.28: Complex cross-sections of the propagation of the object field reconstructed from data-set 2 a) Identifying some cross sections across the object field.b) the ASM propagated field for cross-sections A-F respectively. The white arrows point to some of the perturbing obstacles in the light path. These are identified by tracing rays back to their point of origin.

For the remainder of this analysis of data set 2 we will concentrate on one of these focal points, which corresponds to the neurite that the pinhole was aligned to in figure 3.14.

An EUV ptychogram of a neurite

By picking one of the planes identified in figure 3.28, we can look at the 2-dimensional variation in the EWF of the object, as the propagation distance is varied. Figure 3.29 shows this propagation for slice E (shown previously in figure 3.28e) as it is scanned from 0.5 microns to 2.5 microns. It is clear to see from the propagation in 3.29b) that some dendritic structures do indeed appear as the focus is scanned; a fact reinforced by looking in more detail at the expanded version in 3.29c).

The dendritic structure that appears through this propagation is retarded and attenuated with respect to the areas around it, suggesting that a thicker or denser structure is obstructing the propagation of the light. This feature can be seen in more detail in figure 3.30a). The neurite structure appears to be around 200 nm in width, and to cause a phase shift of just under $\frac{\pi}{2}$ radians.

To try to identify whether these structures are part of a neurite complex, we return to the optical microscope image we showed earlier during the alignment process. A zoomed and enhanced version of this light micrograph is shown here in figure 3.30, next to the EWF from this reconstruction. This zoomed region is the area of the sample scanned during this ptychography experiment. Although the light microscope image is low resolution, there is definitely a strong similarity between the two images, confirming that nothing had drifted during the light microscope alignment and the EUV experiment.

Unfortunately, the sample broke on removal after the ptychography experiment and so no other microscopy techniques could be applied to this same sample. Instead, a sample from the same cultured batch was imaged via SEM. This is shown figure 3.30, which is a close-up of the SEM shown in 3.12d). This also shows a good similarity to the EUV ptychogram, confirming that the reconstructed object EWF is definitely that of a neurite.

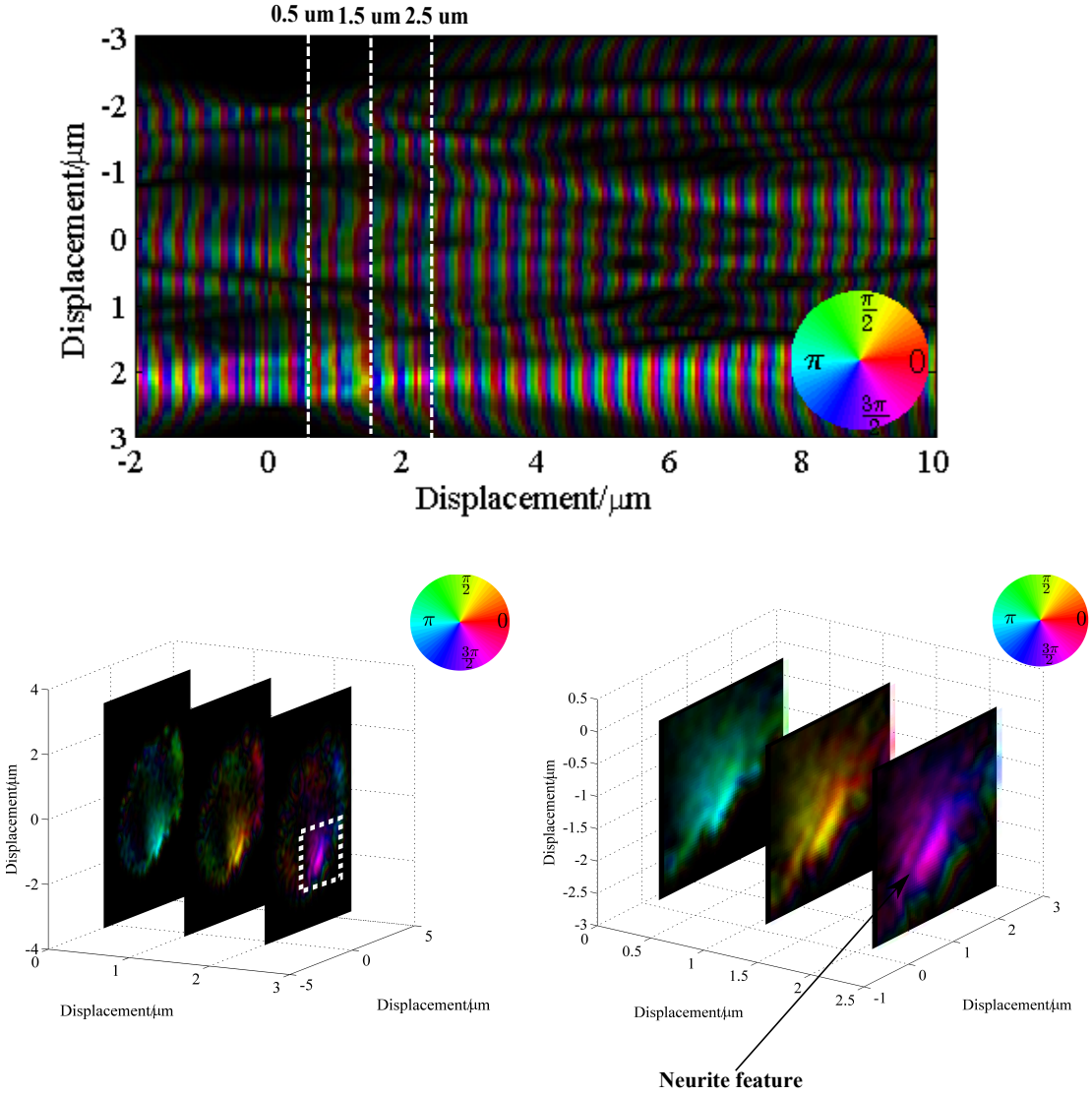

Figure 3.29: A more detailed look at a focal point around 1.5-2 microns. a) The ASM propagation of this cross section as previously shown in 3.28e). Cross sections of the two dimensional complex field corresponding to the white lines in a) are shown in b) at their positions along the travel direction. It is possible to see features that are not visible in the 0.5 micron image coming into focus in the 1.5 micron images and 2.5 micron suggesting that the field has been propagated to the region of the disturbance. c) a zoomed in version of b) showing detail corresponding to a dendritic structure in the sample.

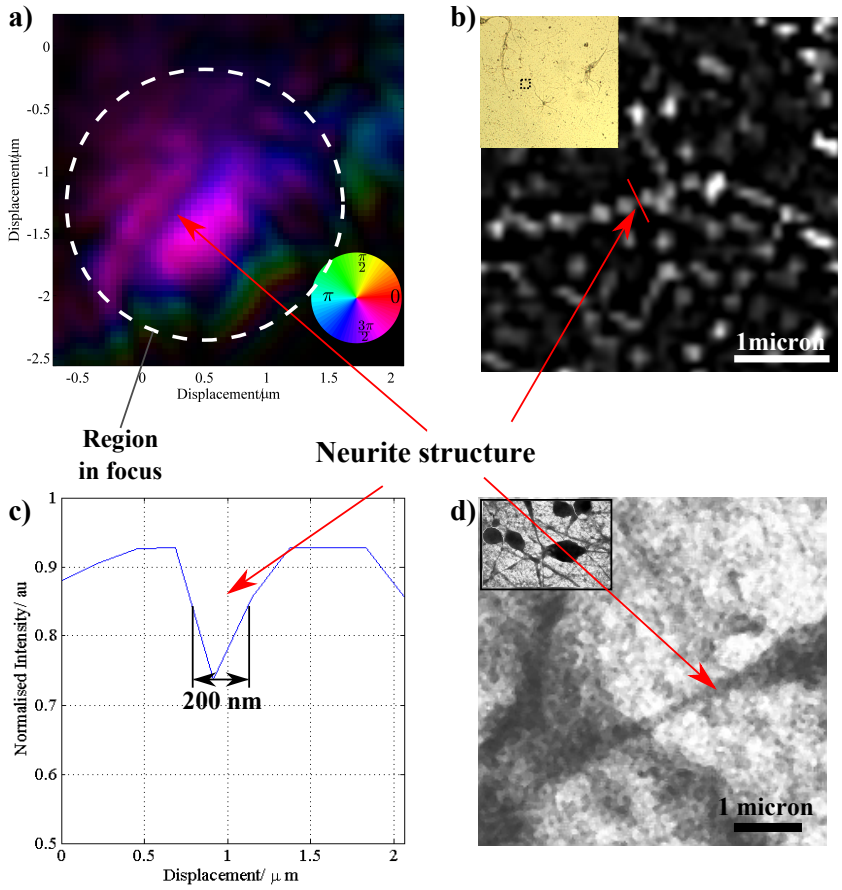

Figure 3.30: Comparison of the reconstructed EWF with other microscopy techniques. a) An image of the full field ptychogram zoomed in at 2.5 micron propagation length, with the in focus region shown (white circle). b)inset: The light microscope image using a 20x 0.4 NA objective previously shown in figure 3.11b), Main: The area inside the white dashed box in the inset image zoomed and enhanced using ImageJ software. The colormap has been inverted to better show the neurite region. c) A cross section of the region marked by the red line in b) showing the feature with is around 200nm. This measurement is limited by the pixel size of the detector on the microscope.d)Inset: The enhanced SEM shown in figure 3.12. The square marks a position that is zoomed in on the main image, Main image: a zoomed in region of the enhanced SEM showing neurite complex. The SEM is from a different sample to the one studied since the original broke on removal from the ptychography system. The arrows mark the similarity between the features in the two different images

From this initial look at the data, it is not possible to tell whether the neurite in question is a dendrite or axon, although the optical micrograph, shown in full in figure 3.11b), suggests that this neurite is connecting between two neurons, and may potentially be an axon. Identifying axons from dendrites is a task that is usually technically challenging unless the sample is micro-tomed and imaged via TEM.

Ideally, from the EUV ptychogram, we could now plot a thickness function for this EWF, as we did for the pinhole defect. As previously mentioned, since the elemental composition,density or thickness are not known, it is more complicated to get this information out of the EWF. Since we know both the transmission and phase of the light however, we can make some investigation into the variation of the composition of the features.

The EWF can be expressed in terms of a thickness function as shown in equation 3.3, re-printed here as equation 3.7, where the refractive index has been written in terms of its real and imaginary parts.

$$U(x,y,z,\lambda) = \exp[\frac{i2\pi}{\lambda}(1-\delta(\lambda)-i\beta(\lambda))T(\rho)] \tag{3.7}$$

Separating out the real and imaginary terms in equation 3.7, allows us to write the following statements for the magnitude and phase of the EWF.

$$\begin{aligned} |U(x,y,z,\lambda)| &= \exp[-\frac{i2\pi}{\lambda}\beta(\lambda)T(\rho)] \\ \mathsf{arg}[U(x,y,z,\lambda)] &= \frac{i2\pi}{\lambda}(1-\delta(\lambda))T(\rho) \end{aligned} \tag{3.8}$$

Dividing the equation for the phase by the equation for the magnitude gives a quantity that is independent of the thickness function, and only includes information about the relationship of the phase delay ratio with the attenuation, or real and imaginary parts of the refractive index, as shown in equation 3.9

$$\frac{\mathsf{arg}[U(x,y,z,\lambda)]}{|U(x,y,z,\lambda)|} = \frac{1-\beta}{\delta} \tag{3.9}$$

This quantity is similar to a measure frequently used in RF electronics [87] and microwave optics [88] and is known as the *loss tangent* of a dielectric medium. It can be understood as the tangent of the phasor angle of the refractive index tensor, which is unique to specific compounds. Hence, a plot of the loss tangent should provide information of the object which is independent of the thickness function and related to the change in composition of the material.

Figure 3.31 shows a plot of the loss tangent for the cross section of the loss tangent over the dendritic structure that we focussed on in figure 3.30.

Figure 3.31 shows that the neurite feature in the EWF does indeed represent an area of the sample which has a different composition to the background, having a higher phase shift per unit attenuation. From the cross section in d) we can see that the width of the neurite structure is around 200 nm wide which corresponds to that which we outlined in figure 3.12e). from an SEM of a neurite. We see that their is an asymmetry about this feature; the signal does not go down to the same background level on either side. This is probably because the gap on the left hand side between the neurite and the adjacent feature is below resolution of the image.

If we now inspect the feature along its length (figure 3.32), we see a steady decrease in the value of the loss tangent, indicating that the composition is changing along it's length, decreasing linearly from right to left. This agrees with the known fact that neurites have a polarity, allowing them to communicate via electrical and chemical gradients. It can also be seen that there is a region of constant composition, corresponding to a plateau in the loss tangent. Although the information here is limited due to the low resolution, a modulation of this kind would fit the model of an axon, with alternating periods of myelin sheath and Ranvier nodes. Combined with the light microscope image however, we can be fairly certain that this is indeed what we are seeing. The spacing of the node would hence be around 300 nm, around the expected size scale for such a feature.

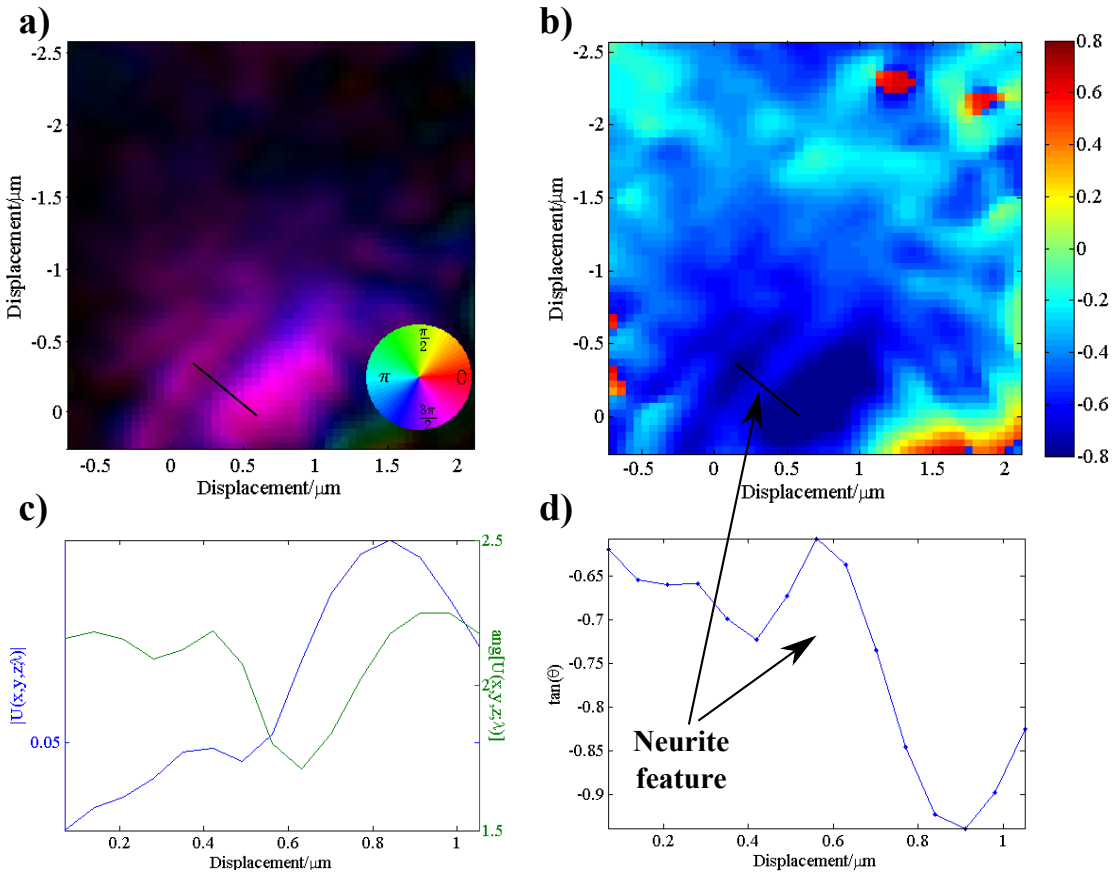

Figure 3.31: A comparison of the dielectric loss tangent to the reconstructed EWF across a cross section of the neurite. a) The reconstructed EWF propagated to the region with the neurite in focus. c) a cross section in amplitude and phase across the region depicted by the sold black line in a). b)A 2-dimensional plot of the loss tangent calculated from the field shown in a) depicting areas of different composition. d) A cross section across the black line shown in b) showing a region with higher phase shift per unit attenuation than the surrounding areas. The reason for the asymmetry about this feature may be the low resolution of the image.

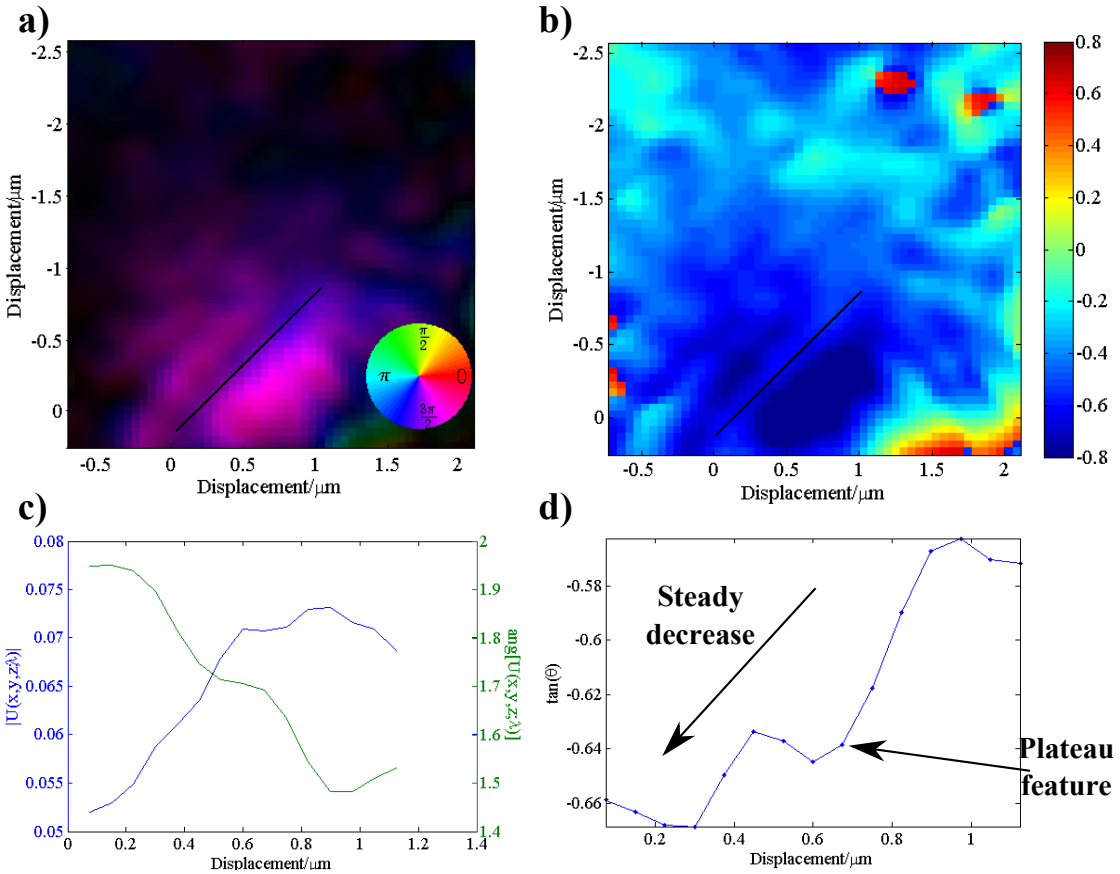

Figure 3.32: A comparison of the dielectric loss tangent to the reconstructed EWF along the length of the neurite. a) The reconstructed EWF propagated to the region with the neurite in focus. c) a cross section along the region depicted by the sold black line in a). b)A 2- dimensional plot of the loss tangent calculated from the field shown in a) depicting areas of different composition. d) A cross section along the black line shown in b) There is a steady decrease in the loss tangent as we move to the left of the plot, indicating a polarity to the neurite composition. There is also a plateau region present where the composition must remain the same. This is indicative of the feature being an axon.

3.2.5 Object field analysis from data-set 1

Now we have analysed the dataset 2, we will return to dataset 1. Recall that this was the dataset that we deduced from figure 3.16 to have less

information about the object.

As with data set 2, it makes sense to first look at the raw reconstruction of the object field. This is shown in figure 3.33 where the average wavefield over 50 iterations (3.33a)) is first isolated by multiplication of a mask of the non-zero probe scan points (3.33b) shows the mask, and c), the resultant object field) and then Fourier interpolated twice ready for the ASM propagation. The result of this interpolation is given in 3.33d).

As with the dataset 2 analysis, we can see that the resulting wavefield, does not show many obvious features, primarily because the reconstructed object field is currently situated in the plane of the pinhole. To propagate it to the correct plane, we will use the ASM with all the same assumptions as for the dataset 2. Figure 3.34 shows this propagation for a range of cross sections through the object field.

Comparing this to dataset 2, we can see that the region of the sample in dataset 1 does indeed seem to be much more weakly scattering, and indeed it is hard to pick out any particular regions which may be in focus at points along the propagation. However, there are still a few points of interest, one of which is identified by a white arrow in figure 3.34d).

Figure 3.35 shows a 2D scan of this area in 3.34d). This figure shows that although the features here become slightly more sharp, they are still not well defined, which is what would be expected for a sample region of poor contrast.

To better see what the field looks like at the region that is in focus, figure 3.36 shows the field at 3 microns propagation distance.

The features in this field still looked very blurred, even though they are in the best focus position. This is probably due to the low contrast of this region of the sample and low diffraction limited resolution of the experiment.

3.3 Summary

In summary, this section has shown the first demonstration of ptychography of real objects from a lab based source of short wavelength radiation. Whilst initially the data did not converge to a solution due to the limited number of views collected, an improved starting probe calculated directly from the data was used, resulting in good convergence and high correlation between two independently acquired datasets.

The reconstructed probes provided enough information to identify and analyse the defects in the laser drilled Molybdenum pinhole used to provide the support constraint. A maximum thickness of 6 nm $\pm$ 1 nm was found for the obstructing piece of Molybdenum.

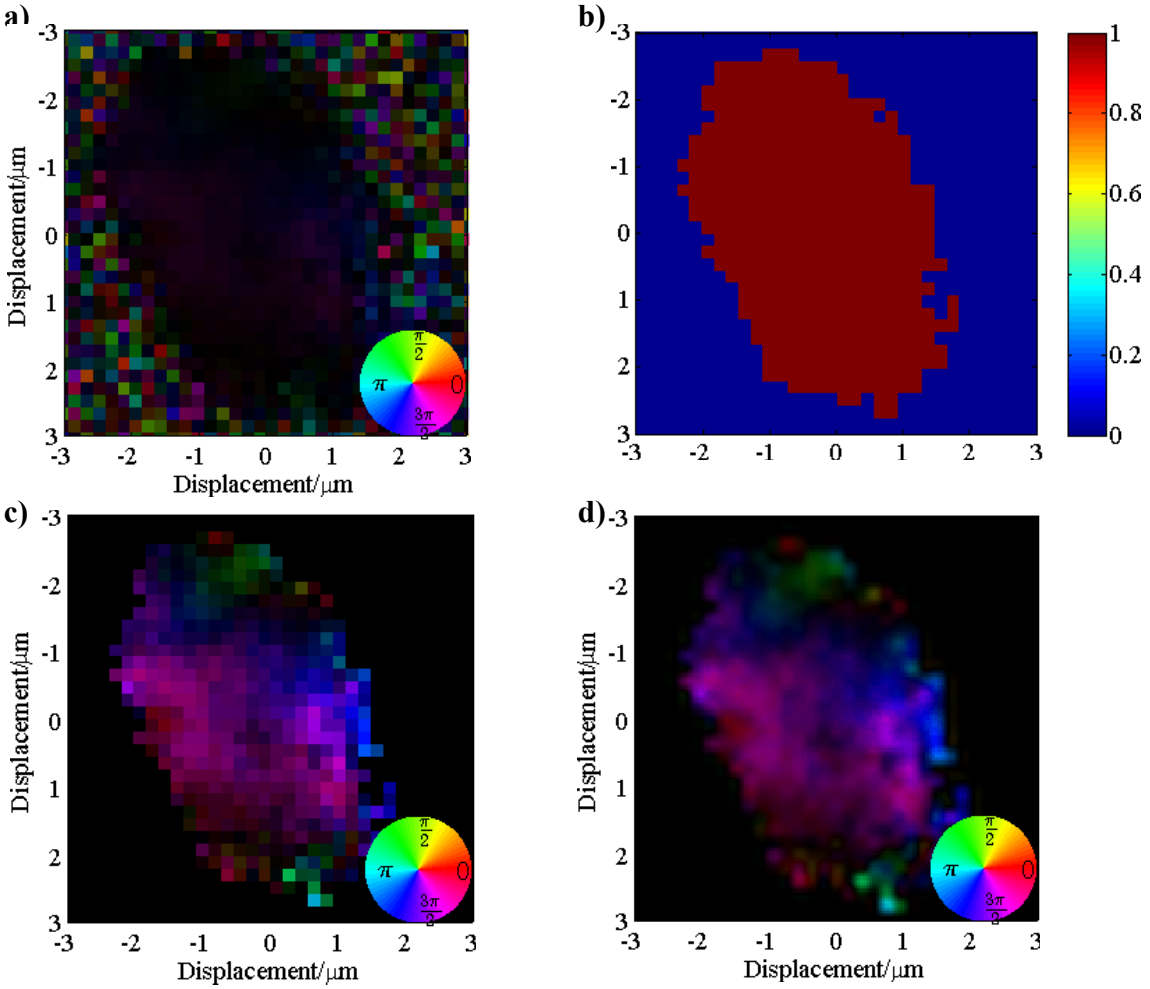

Figure 3.33: The reconstructed object for data-set 1. a) The mean average object exit wave field over 50 independent pseudo-random starting seeds. b) A binary mask of the reconstructed field of view formed by addition of the reconstructed probe magnitudes at the 4 scan positions. The resultant magnitudes were then thresholded at 10%. c) The reconstructed field shown in a) multiplied by the mask in b). d) The field of view in c) interpolated twice by padding in Fourier space to increase the sampling rate. No extra information is added in this process.

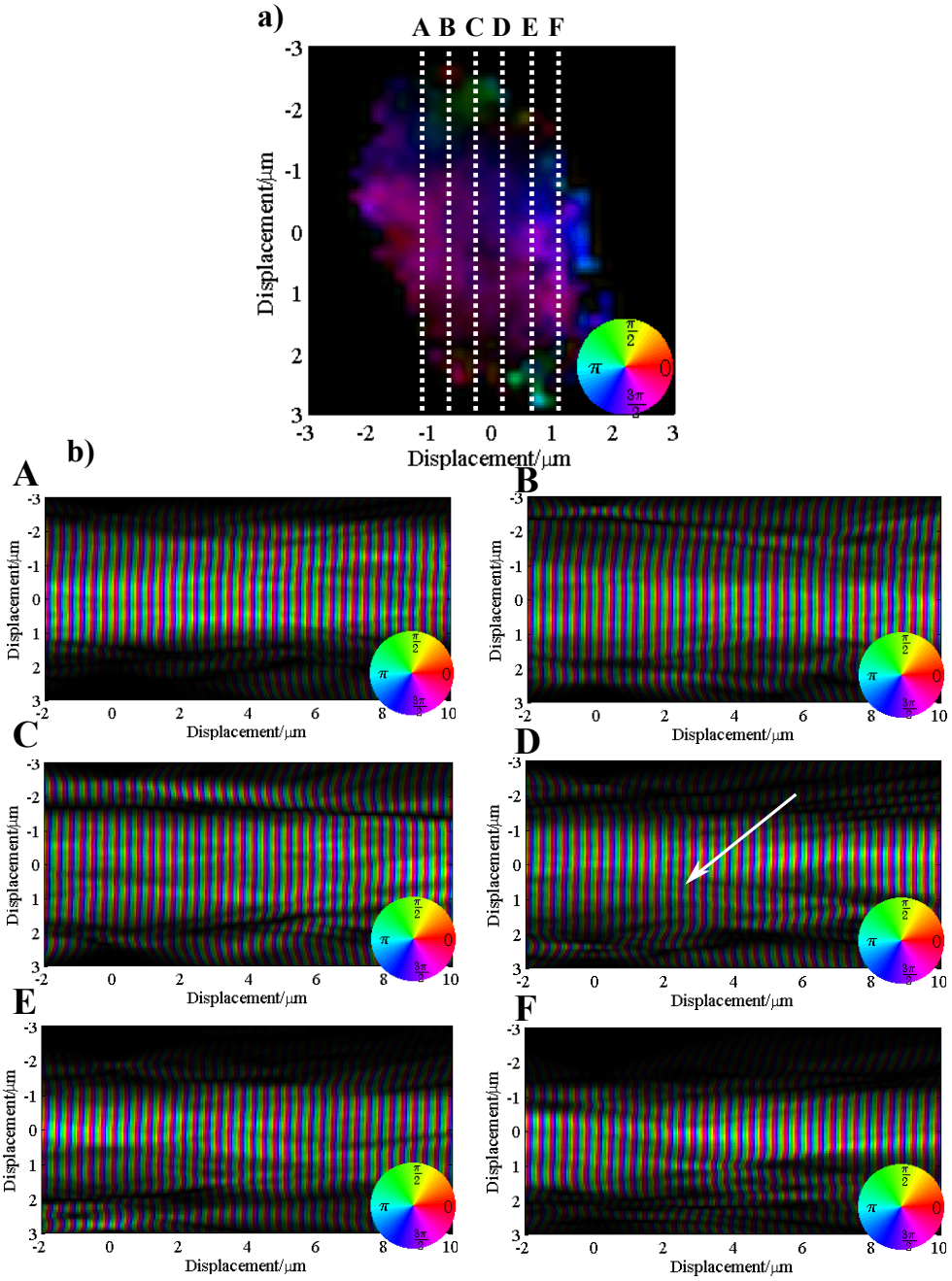

Figure 3.34: Complex cross-sections of the propagation of the object field reconstructed from data-set 1 a) Identifying some cross sections across the object field.b) the ASM propagated field for cross-sections A-F respectively. Compared to figure 3.28 these images show that the object imaged here has much less contrast and hence is much less strongly scattering than dataset 2. The white arrow in d) points to a region that is in focus.

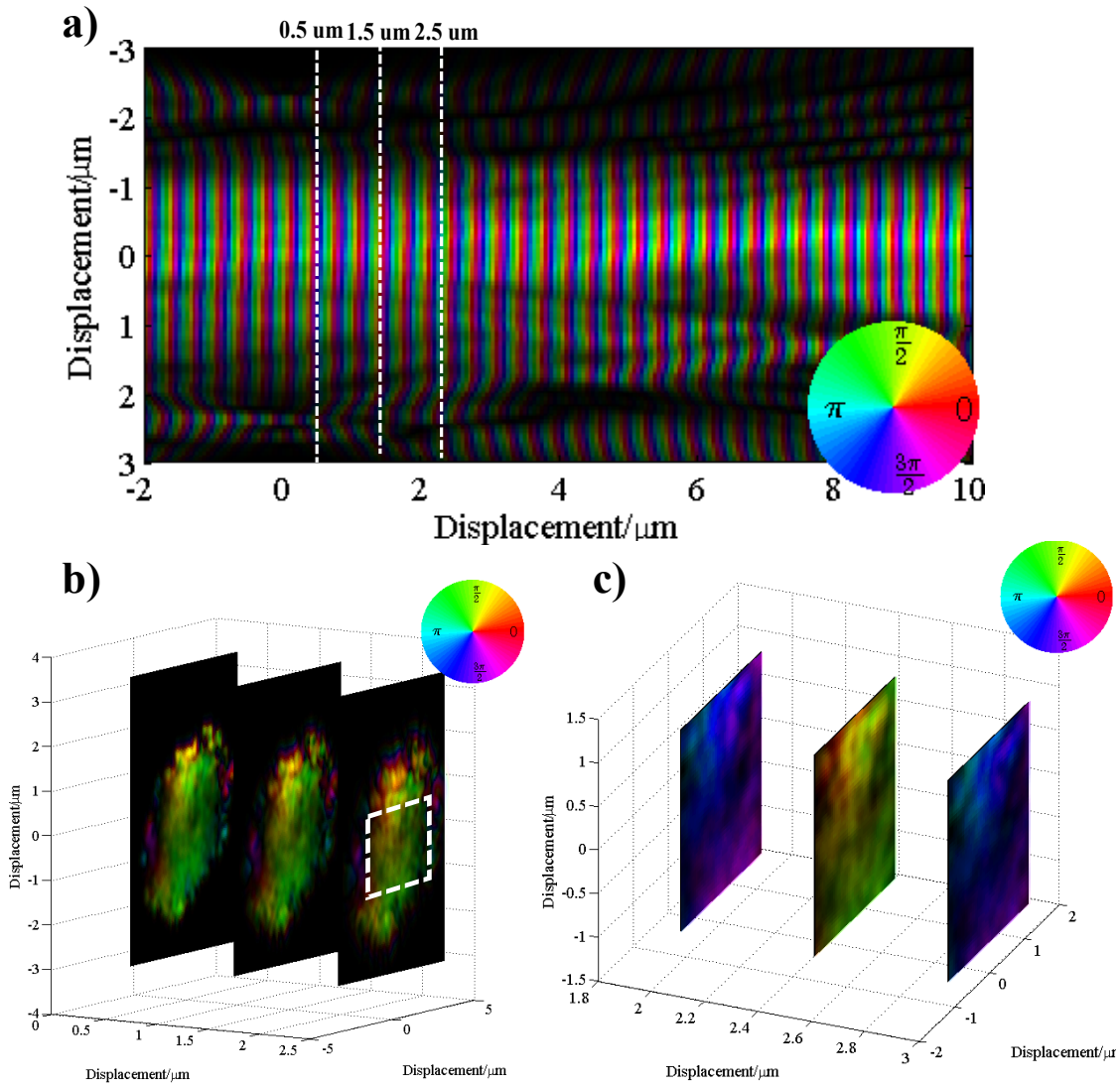

Figure 3.35: A more detailed look at a focal point around 1.5-2.5 miorons in dataset 1. a) The ASM propagation of this cross section as previously shown in 3.28e). Cross sections of the two dimensional complex field corresponding to the white lines in a) are shown in b) at their positions along the travel direction. c) shows a finer scan in the travel direction of a zoomed in section of b). It is still very hard to discern a region that becomes sharp with this propagation.

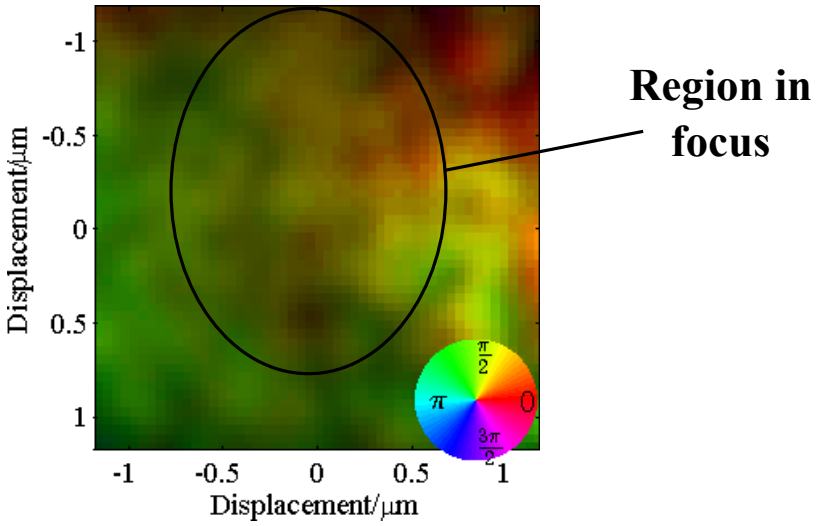

Figure 3.36: The object field at 3 microns propagation distance. The features that are in focus are circled, however they still seem blurred. This may be due to their low contrast, and their feature size being below the diffraction limit of this experiment.

Two reconstructed objects were examined; one providing no resolvable information, and the other providing compositional information about the cultured neurite growth. The neurite under investigation was imaged with 180 nm resolution, the diffraction limit for this experiment, and better than could be achieved via a regular light microscope. By analysis of the loss tangent of this structure in combination with the light microscope image it was identified to be an axon; information not available by EM or light microscopy without destruction of the sample.

Chapter 4

Conclusions

The work outlined in this thesis has been fairly varied from a microscopy point of view. After outlining the background of phase retrieval techniques and the nature of the source in chapter 1, we visited topics as diverse as the exploration of the treatment of coherence through a computational imaging system(chapter 2) and microscopy of extended hippocampal neural complexes in chapter 3.

This chapter will pull together the main conclusions and results from the two experimental chapters.

4.1 Coherence in CDI, chapter 2

The main idea behind the published work set out in this chapter was to investigate the tolerance of the standard CDI algorithms as the relative bandwidth of the source was increased from 0.7% to 20%, increasing the scattered flux by a factor of 5. For the conventional, uniform spectra of existing lab and facility based sources of short wavelength radiation, has been shown in previous work [67] to lower the visibility of the recorded speckle pattern by such an extent that, unless specifically designed algorithms [66] are used, or the signals separated [73], the process of CDI would fail completely. The hypothesis under test during the investigation in this chapter was whether for a non-dispersive object the modulated nature of the high harmonic spectrum would improve the visibility of the signal enough in the broadband case at selected spatial frequencies so that the CDI algorithm could reconstruct both correctly and reliably.

An experiment was designed and implemented to measure the speckle patterns of the same non-dispersive, binary transmission test sample in both broadband and narrowband conditions. The raw data were compared to

confirm that indeed the effect of the high bandwidth was enough to lower the visibility of the recorded speckles, alongside further analysis of the real-space spatial dependence of the signal on the coherence.

CDI reconstructions were then performed on both data sets and a statistical interpretation of the results was performed. It was found that, whilst the broadband reconstructions were a little more noisy and slightly blurred, applying the shrinkwrap modification to the iterate, and then selecting the iterate that corresponded to the lowest Fourier-space error gave a result that was consistent in shape almost 100% of the time. These reconstructions were claimed *not* to be a solution to the phase problem, but instead are presented as an improved support guess for further refinement via other optimisation algorithms. This result was claimed to be broadly applicable across a range of high energy photon sources provided that the spectrum can be modulated accordingly.

4.2 Iterative ptychography experiments, chapter 3

This chapter presents the key advances in the use of lab-based EUV microscopy of extended complex valued objects. At the time of writing this thesis, it was the first such result in the world, and is soon to be published in an appropriate, high impact, journal.

The main concepts for the experiments detailed in this chapter were:

1. To check and prove that iterative ptychography could be used to image extended samples for a high harmonic source.

2. To image complex-valued objects, notably those of scientific interest.

3. To attempt to image and characterise biological samples using the high harmonic source via iterative ptychography, notably hippocampal neurites.

To gain some experience working with experimental ptychographic data sets, I attended a beamtime with Ian Robinsons group (UCL) at the i13 coherence beamline at Diamond Light Source. Chapter 3, section 3.1 presents some simple results from this experiment where a test sample was imaged. The lessons learned from processing this data were summarised as

1. Applying a support to the probe seems essential to get repeatable reconstructions from real data. Otherwise the probe may tend to move to the edges of the support.

2. If the independence between all views is high, it would seem that a simple modelled probe guess can be used.

3. Using the same probe across two independent data sets improves the stability of the probe and hence object field reconstructions.

4. Floated pixels may cause multiple threshold crossing points and hence issues with the interpretation of the FRC and so a standard cut-off cannot be used for the figure of merit for resolution.

An experiment was next performed using the high harmonic source at Southampton, the tips in the above list were applied in combination with a novel formation of a probe constraint to encourage the data to converge. The resulting probe wave-field from this showed a high Fourier ring correlation out to a high resolution across two independent and uncorrelated data sets. The investigation of the probe wave-field allowed characterisation of defects in the pinhole: a thickness of 6 nm $\pm$ 1 nm was found for this defect, with a lateral resolution of 90 nm.

The two reconstructed object data sets were examined and it was confirmed that a neurite had indeed been imaged, as we had intended from the sample alignment steps. Since the composition of the sample was complex and unknown, the loss tangent was used to note the change in composition of the sample across a cross section and along its length. This revealed that the neurite was around 200 nm thick at its thinnest point (a resolution above the Sparrow diffraction limit of 180 nm), and modulations of compositions along its length were observed. This combined with the initially light microscope image and SEMs of other samples confirmed that what was imaged was in fact an axon, the neurites responsible for carrying neuron communication.

The capability of HHG ptychography to resolve such features and establish patterns in their composition is a very useful tool, that has been so far unreported in the field. Usually in order to get this information of neurite complexs, active microscopy (PALM/STORM) is required and even then it can be inconclusive due to the resolution limitations and need for sample preparation.

Chapter 5

Future Work

The main goal of the coherent diffraction project at Southampton is ultimately to image biological samples at high diffraction-limited resolution using a lab-based source. The University of Southampton is a prime location for such research since the group is on the same campus, and has very strong links with, the Institute for Life Sciences (IfLS) with whom the work detailed in the iterative ptychography section of this report (chapter 3) was part of a collaboration with.

Although the work detailed in this thesis provides a lot of the ground work for future work. There are a number of things that have been highlighted in the analysis of this thesis which currently provide limitations on the applicability of the HHG coherent diffraction technique to such a goal.

These are

1. The stability of the source
2. The available flux
3. The wavelength of the source
4. The repeatability of biological sample manufacture

The stability of the source is inherently linked to the stability of the pump laser system. Currently, the maximum data collection time for an experiment is limited to around 20 minutes (3) due to this instability, limiting the field of view that can be collected for a ptychogram.

This limitation can be addressed from a few different perspectives. The first of these is to make the laser system more stable. Since the cavity Spectra Physics amplifier system used throughout this thesis is not temperature stabilised, one should expect nanoscopic slow thermal drifts to cause shifting

of the cavity components. This in term will cause the EUV source to drift over time. To fix this directly would involve the major task of rebuilding the amplifier system on a water-cooled table. Instead it may be preferably to actively or passively stabilise the laser beam exiting the system. Active methods, although nowadays very accurate, could have the disadvantage of causing the beam to jump as the steering is corrected. Instead is may be preferable to apply the passive step of de-magnifying the beam, which would give an improvement in stability proportional to the de-magnification. However, this would then affect the available flux of the system.

To improve the available flux, one could consider pumping a larger volume inside the gas cell. Since the Keyldysh parameter (detailed in chapter 1) is currently very small indeed, a more slowly focussed pump beam could be used allowing a greater volume to be pumped. Other source geometries are also under investigation in the group such as those of gas-filled capillaries. These show great promise for increased flux at 40 eV as well as for future sources extending down to the water-window (500eV - 1keV) by using Neon and Helium gases to push the energy cut-off in the HHG process. However, these sources are currently too unstable for use in imaging experiments. This novel source research is part of an ongoing collaboration with the Central Laser Facility at the Rutherford Appleton laboratories.

Lastly, the availability of suitable biological samples is limited. The dominant issue with these samples is currently the repeatability of creating a sample with the necessary features of interest. For neurons this is the neural synapse region. This is, however, the nature of dealing with biological specimens. The samples are currently manufactured by the group in collaboration with IfLS, and this work is part of the remit of this collaboration.

Bibliography

[1] Richard Feynman. Plenty of room at the bottom. In *American Physical Society*, March 1959.

[2] Gordon E Moore and Life Fellow. Cramming More Components onto Integrated Circuits. 86(1):82–85, 1998.

[3] N Yao and ZL Wang, editors. *Handbook of microscopy for nanotechnology*. Kluwer Academic Publishers, London, 2005.

[4] Sergei N. Magonov and Myung-Hwan Whangbo. *Surface Analysis with STM and AFM: Experimental and Theoretical Aspects of Image Analysis*. VCH, Cambridge, 1996.

[5] Louis de Broglie. XXXV. A tentative theory of light quanta. *Philosophical Magazine Series 6*, 47(278):446–458, February 1924.

[6] Eugene Hecht. *Optics*. Addison Wesley, London, fourth edi edition, 2002.

[7] David B. Williams and C. Barry Carter. *Transmission Electron Microscopy*. Springer US, Boston, MA, 2009.

[8] Ernst Abbe. Beiträge zur Theorie des Mikroskops und der mikroskopischen Wahrnehmung. *Archiv für Mikroskopische Anatomie*, 9(1):413–418, December 1873.

[9] H. Fripp and H Helmholz. On the Limits of the Optical Capacity of the Microscope. *The Monthly Microscopical Journal*, 16(1):15–39, July 1876.

[10] Lord Rayleigh. XXV. On the manufacture and theory of diffraction-gratings. *Philosophical Magazine Series 4*, 47(311):193 – 205, 1874.

[11] A.E Siegmann. *Lasers*. University Science Books, Sausilito, 1986.

[12] Dominik Wildanger, Brian R Patton, Heiko Schill, Luca Marseglia, J P Hadden, Sebastian Knauer, Andreas Schönle, John G Rarity, Jeremy L O'Brien, Stefan W Hell, and Jason M Smith. Solid immersion facilitates fluorescence microscopy with nanometer resolution and sub-ångström emitter localization. *Advanced materials (Deerfield Beach, Fla.)*, 24(44):OP309–13, November 2012.

[13] Hari Shroff. Section on High Resolution Optical Imaging.

[14] Jb Pendry. Negative refraction makes a perfect lens. *Physical review letters*, 85(18):3966–9, October 2000.

[15] M V Berry and S Popescu. Evolution of quantum superoscillations and optical superresolution without evanescent waves. *Journal of Physics A: Mathematical and General*, 39(22):6965–6977, June 2006.

[16] Maja Hrabak, Ranka Stern Padovan, Marko Kralik, David Ozretic, and Kristina Potocki. Scenes from the past: Nikola Tesla and the discovery of X-rays. *Radiographics : a review publication of the Radiological Society of North America, Inc*, 28(4):1189–92, 2008.

[17] W. C. Röntgen. Ueber eine neue Art von Strahlen. *Annalen der Physik*, 300(1):1–11, 1898.

[18] J. J Thomson. Cathode Rays. *Philosophical Magazine*, 44:293, 1897.

[19] C. Davisson and L. Germer. Diffraction of Electrons by a Crystal of Nickel. *Physical Review*, 30(6):705–740, December 1927.

[20] V. K. Zworykin and E. G. Ramberg. Surface Studies with the Electron Microscope. *Journal of Applied Physics*, 12(9):692, 1941.

[21] Gareth Griffiths. Biological Specimen Preparation for Transmission Electron Microscopy. by Audrey M. Glauert & Peter R. Lewis. Practical Methods in Electron Microscopy Vol. 17. Series Editor Audrey Glauert. Portland Press, 1998. Softback, f39.50, ISBN 185578 060 7, hardbac. *Journal of Microscopy*, 196(3), December 1999.

[22] Robin Leslie Owen, Enrique Rudiño Piñera, and Elspeth F Garman. Experimental determination of the radiation dose limit for cryocooled protein crystals. *Proceedings of the National Academy of Sciences of the United States of America*, 103(13):4912–7, March 2006.

[23] M R Howells, T Beetz, H N Chapman, C Cui, J M Holton, C J Jacobsen, J Kirz, E Lima, S Marchesini, H Miao, D Sayre, D a Shapiro, J C H Spence, and D Starodub. An assessment of the resolution limitation due to radiation-damage in x-ray diffraction microscopy. *Journal of electron spectroscopy and related phenomena*, 170(1-3):4–12, March 2009.

[24] R Henderson. The potential and limitations of neutrons, electrons and X-rays for atomic resolution microscopy of unstained biological molecules. *Quarterly reviews of biophysics*, 28(2):171–93, May 1995.

[25] R F Egerton, P Li, and M Malac. Radiation damage in the TEM and SEM. *Micron (Oxford, England : 1993)*, 35(6):399–409, January 2004.

[26] Jean Marc, Frédéric Clette, John Daniel, Jean-françois Hochedez, E I T Consortium, Spatial De Liège, Avenue Pré-aily, and B Angleur. In-orbit diagnostic of the EIT EUV CCD radiation induced aging . pages 1–10, 1997.

[27] R Sobierajski. Interaction of intense ultrashort XUV pulses with silicon. *SPIE Europe ...*, pages 409–410, 2009.

[28] Vladimir S Popov. Tunnel and multiphoton ionization of atoms and ions in a strong laser field (Keldysh theory). *Physics-Uspekhi*, 47(9):855–885, September 2004.

[29] T. J. Butcher, P. N. Anderson, R. T. Chapman, P. Horak, J. G. Frey, and W. S. Brocklesby. Bright extreme-ultraviolet high-order-harmonic radiation from optimized pulse compression in short hollow waveguides. *Physical Review A*, 87(4):043822, April 2013.

[30] Joseph W Goodman. *Introduction to Fourier Optics*. Roberts and Company, third edit edition, 2005.

[31] W.H Press, B.P Flannery, S.A Teukolsky, and W.T Vetterling. *Numerical Recipes: The Art of Scientific Computing*. Cambridge University Press, Cambridge, 1st editio edition, 1986.

[32] D. Sayre. Some implications of a theorem due to Shannon. *Acta Crystallographica*, 5(6):843, November 1952.

[33] WB Yun, J Kirz, and D Sayre. Observation of the soft X-ray diffraction pattern of a single diatom. *Acta Crystallographica Section A: ...*, 3(1987):131–133, 1987.

[34] Jianwei Miao, Pambos Charalambous, Janos Kirz, and David Sayre. Extending the methodology of X-ray crystallography to allow imaging of micrometre-sized non-crystalline specimens. *Nature*, 400(July):342–344, 1999.

[35] R. W. Gerchberg and W. O. Saxton. A practical algorithm for determination of phase from image and diffraction plane pictures. *OPTIK*, 35(2):237–246, 1972.

[36] J R Fienup. Reconstruction of an object from the modulus of its Fourier transform. *Optics Letters*, 3(1):27–29, 1978.

[37] Erik H Anderson and Keith O Hodgson. Phase retrieval of diffraction patterns from noncrystalline samples using the oversampling method. *Physical Review B*, pages 1–6, 2003.

[38] J. R. Fienup, T. R. Crimmins, and W. Holsztynski. Reconstruction of the support of an object from the support of its autocorrelation. *Journal of the Optical Society of America*, 72(5):610, May 1982.

[39] J Miao, D Sayre, and Henry N Chapman. Phase retrieval from the magnitude of the Fourier transforms of nonperiodic objects. *J. Opt. Soc. Am. A*, 15:1662–1669, 1998.

[40] Alberto Cambrini and Laura Martein. *Generalized Convexity and Optimization*, volume 616 of *Lecture Notes in Economics and Mathematical Systems*. Springer Berlin Heidelberg, Berlin, Heidelberg, 2009.

[41] V Elser, I Rankenburg, and P Thibault. Searching with iterated maps. *Proceedings of the National Academy of Sciences of the United States of America*, 104(2):418–23, January 2007.

[42] Pierre Thibault. *Algorithmic Methods in Diffraction microscopy*. Doctor of philosophy, Cornell Unversity, 2007.

[43] S Marchesini, HN Chapman, and A Barty. Phase aberrations in diffraction microscopy. *arXiv preprint physics/ ...*, pages 380–382, 2005.

[44] JR Fienup and CC Wackerman. Phase-retrieval stagnation problems and solutions. *JOSA A*, 3(11):1897–1907, 1986.

[45] Stefano Marchesini, H He, Henry N Chapman, Stefan P Hau-Riege, a. Noy, M. R. Howells, U. Weierstall, and J. C. H. Spence. X-ray image reconstruction from a diffraction pattern alone. *Physical Review B*, 68(14):1–4, October 2003.

[46] W. Hoppe. Beugung im inhomogenen Primärstrahlwellenfeld. I. Prinzip einer Phasenmessung von Elektronenbeungungsinterferenzen. *Acta Crystallographica Section A*, 25(4):495–501, July 1969.

[47] J M Rodenburg. Ptychography and Related Diffractive Imaging Methods. *Advances in Imaging and Electron Physics*, 150(07):87–184, 2008.

[48] Henry N. Chapman. Phase-retrieval X-ray microscopy by Wigner-distribution deconvolution. *Ultramicroscopy*, 66(3-4):153–172, December 1996.

[49] J M Rodenburg and H M L Faulkner. A phase retrieval algorithm for shifting illumination. *Applied Physics Letters*, 85(20):4795, 2004.

[50] Andrew M Maiden and John M Rodenburg. An improved ptychographical phase retrieval algorithm for diffractive imaging. *Ultramicroscopy*, 109(10):1256–62, September 2009.

[51] Pierre Thibault, Martin Dierolf, Oliver Bunk, Andreas Menzel, and Franz Pfeiffer. Probe retrieval in ptychographic coherent diffractive imaging. *Ultramicroscopy*, 109(4):338–43, March 2009.

[52] Fucai Zhang, Isaac Peterson, and J Vila-Comamala. Translation position determination in ptychographic coherent diffraction imaging. *Optics express*, 21(11):13592–13606, 2013.

[53] B. Enders, M. Dierolf, P. Cloetens, M. Stockmar, F. Pfeiffer, and P. Thibault. Ptychography with broad-bandwidth radiation. *Applied Physics Letters*, 104(17):171104, April 2014.

[54] Pierre Thibault and Andreas Menzel. Reconstructing state mixtures from diffraction measurements. *Nature*, 494(7435):68–71, February 2013.

[55] T. B. Edo, D. J. Batey, a. M. Maiden, C. Rau, U. Wagner, Z. D. Pešić, T. a. Waigh, and J. M. Rodenburg. Sampling in x-ray ptychography. *Physical Review A*, 87(5):053850, May 2013.

[56] D. J. Batey, T. B. Edo, C. Rau, U. Wagner, Z. D. Pešić, T. a. Waigh, and J. M. Rodenburg. Reciprocal-space up-sampling from real-space oversampling in x-ray ptychography. *Physical Review A*, 89(4):043812, April 2014.

[57] AdmiralPR. http://www.phasefocus.com/, 2014.

[58] Martin Dierolf, Andreas Menzel, Pierre Thibault, Philipp Schneider, Cameron M Kewish, Roger Wepf, Oliver Bunk, and Franz Pfeiffer. Ptychographic X-ray computed tomography at the nanoscale. *Nature*, 467(7314):436–9, September 2010.

[59] M Holler, a Diaz, M Guizar-Sicairos, P Karvinen, Elina Färm, Emma Härkönen, Mikko Ritala, a Menzel, J Raabe, and O Bunk. X-ray ptychographic computed tomography at 16 nm isotropic 3D resolution. *Scientific reports*, 4:3857, January 2014.

[60] Kay Diederichs and P. Andrew Karplus. Improved R-factors for diffraction data analysis in macromolecular crystallography. *Nature Structural Biology*, 4(4):269–275, April 1997.

[61] H.N. Chapman, Anton Barty, Stefano Marchesini, Aleksandr Noy, S.P. Hau-Riege, Congwu Cui, M.R. Howells, Rachel Rosen, Haifeng He, J.C.H. Spence, and Others. High-resolution ab initio three-dimensional x-ray diffraction microscopy. *JOSA A*, 23(5):1179–1200, 2006.

[62] Matthew D Seaberg, Daniel E Adams, Ethan L Townsend, Daisy A Raymondson, William F Schlotter, Yanwei Liu, Carmen S Menoni, Lu Rong, Chien-chun Chen, Jianwei Miao, Henry C Kapteyn, and Margaret M Murnane. Ultrahigh 22 nm resolution coherent diffractive imaging using a desktop 13 nm high harmonic source. *Optics Express*, 19(23):7235–7239, 2011.

[63] Marin Van Heel. Similarity measures between images. *Ultramicroscopy*, 21(1):95–100, January 1987.

[64] Marin van Heel and Michael Schatz. Fourier shell correlation threshold criteria. *Journal of structural biology*, 151(3):250–62, September 2005.

[65] CM Sparrow. On spectroscopic resolving power. *The Astrophysical Journal*, 1916.

[66] Bo Chen, RA Ruben a. Dilanian, Sven Teichmann, Brian Abbey, Andrew G. AG Peele, Garth J. GJ Williams, Peter Hannaford, LV Dao, HM Harry M. Quiney, Keith a. KA Nugent, and Lap Van Dao. Multiple wavelength diffractive imaging. *Physical Review A*, 79(2):3–6, 2009.

[67] Brian Abbey, LW Whitehead, and HM Quiney. Lensless imaging using broadband X-ray sources. *Nature ...*, 5(7):420–424, June 2011.

[68] A D Parsons, R T Chapman, P Baksh, B Mills, S Bajt, W S Brocklesby, and J G Frey. Ultra-broadband support determination for extreme ultraviolet coherent diffractive imaging from a high harmonic source. *Journal of Optics*, 15(9):094009, September 2013.

[69] A.D. Parsons, R.T. Chapman, B. Mills, S. Bajt, J.G. Frey, and W.S. Brocklesby. Temporal Coherence Effects on Coherent Diffractive Imaging of a Binary Sample by a High Harmonic Source. *EPJ Web of Conferences*, 41:12015, March 2013.

[70] A.D Parsons, R.T Chapman, B Mills, T.J Butcher, JG Frey, and W.S Brocklesby. 90 nm resolution reconstruction from a polychromatic signal using monochromatic phase retrieval techniques. In *The European Conference on Lasers and Electro-Optics*, page CD_P35, Munich, 2011. IEEE.

[71] Jesse N. Clark and Andrew G. Peele. Simultaneous sample and spatial coherence characterisation using diffractive imaging. *Applied Physics Letters*, 99(15):154103, 2011.

[72] Stefan Witte, V. T. Tenner, D. W. E Noom, and Kjeld S E Eikema. Coherent Lensless imaging with Ultra-Broadband Light Sources. *EPJ Web of Conferences*, 41:12014, March 2013.

[73] Stefan Witte, Vasco T Tenner, Daniel WE Noom, and Kjeld SE Eikema. Lensless diffractive imaging with ultra-broadband table-top sources: from infrared to extreme-ultraviolet wavelengths. *Light: Science & Applications*, 3(3):e163, March 2014.

[74] J C H Spence, U Weierstall, and M Howells. Coherence and sampling requirements for diffractive imaging. *Ultramicroscopy*, 101(2-4):149–52, November 2004.

[75] Forbes R. Powell. Care and feeding of soft x-ray and extreme ultraviolet filters. In Harold E. Bennett, Lloyd L. Chase, Arthur H. Guenther, Brian E. Newnam, and M. J. Soileau, editors, *Proc. SPIE 1848, 24th Annual Boulder Damage Symposium Proceedings – Laser-Induced Damage in Optical Materials*, volume 1848, pages 503–515, June 1993.

[76] Forbes R. Powell. Thin film filter performance for extreme ultraviolet and x-ray applications. *Optical Engineering*, 29(6):614, 1990.

[77] Luxel. Luxel-standard filters, 2013.

[78] B Henke. X-Ray Interactions: Photoabsorption, Scattering, Transmission, and Reflection at E = 50-30,000 eV, Z = 1-92. *Atomic Data and Nuclear Data Tables*, 54(2):181–342, July 1993.

[79] Manuel Guizar-Sicairos, Samuel T Thurman, and James R Fienup. Efficient subpixel image registration algorithms. *Optics letters*, 33(2):156–8, January 2008.

[80] D. T. Attwood. *Soft X-Rays and Extreme Ultraviolet Radiation: Principles and Applications*. Cambridge University Press, Cambridge, 1st edition, 2007.

[81] K Giewekemeyer, M Beckers, and T Gorniak. Ptychographic coherent x-ray diffractive imaging in the water window. *Optics*, 19(2):885–888, 2011.

[82] Andrew M Maiden, John M Rodenburg, and Martin J Humphry. Optical ptychography: a practical implementation with useful resolution. *Optics letters*, 35(15):2585–7, August 2010.

[83] Robert S. Murphy. FAB4: Nagoya - Annual International neuroELT Conference, 2013.

[84] Per Andersen, Richard Morris, David Amaral, Tim Bliss, and John O'Keefe. *The Hippocampus Book*. Oxford University Press, Oxford, December 2006.

[85] Clker.com, 2013.

[86] R R Sturrock. Myelination of the mouse corpus callosum. *Neuropathology and applied neurobiology*, 6(6):415–20, 1980.

[87] Jaejin Lee, Yang-Ki Hong, Woncheol Lee, Gavin S. Abo, Jihoon Park, Won-Mo Seong, and Won-Ki Ahn. Control of magnetic loss tangent of hexaferrite for advanced radio frequency antenna applications. *Journal of Applied Physics*, 113(7):073909, 2013.

[88] Jerzy Krupka, Jonathan Breeze, and Anthony Centeno. Measurements of permittivity, dielectric loss tangent, and resistivity of float-zone silicon at microwave frequencies. *Microwave Theory ...*, 54(11):3995–4001, 2006.